MEDICAL PHYSICS International

The Journal of the International Organization for Medical Physics (IOMP)

Volume 14, Number 1; June 2026

MEDICAL PHYSICS INTERNATIONAL

THE JOURNAL OF

THE INTERNATIONAL ORGANIZATION FOR MEDICAL PHYSICS

MEDICAL PHYSICS INTERNATIONAL
The Journal of the International Organization for Medical Physics

Aims and Coverage:

Medical Physics International (MPI) is the official IOMP journal. It provides a platform for medical physicists to share their experience, ideas and new information generated from their work of scientific, educational and professional nature. The e-journal is available free of charge to IOMP members. MPI- History Edition is dedicated to History of Medical Physics.

MPI web address: www.mpijournal.org

Published by: The International Organization for Medical Physics (IOMP); Web address: www.iomp.org ; Post address: IOMP c/o IPEM, 230 Tadcaster Road, York YO24 1ES, UK.

ISSN 2306 – 4609

CONTENTS

EDITORIAL

EDITORIAL FROM CO-EDITORS-IN-CHIEF

Francis Hasford & Sameer Tipnis

Advancing Medical Physics in an Era of Innovation, Intelligence, and Global Collaboration

Welcome to Volume 14, Issue 1 (2026) of *Medical Physics International (MPI) journal*, the official journal of the International Organization for Medical Physics (IOMP). This issue reflects the continued evolution of medical physics as a scientific discipline, a healthcare profession, and a global community committed to improving patient care through innovation, evidence-based practice, education, and international collaboration.

The contributions featured in this issue demonstrate the breadth and vitality of contemporary medical physics. From radiation dose optimization and adaptive radiotherapy to artificial intelligence (AI), machine learning, quality assurance, and educational innovation, the articles collectively underscore the expanding responsibilities of medical physicists in an increasingly technology-driven healthcare environment.

Patient safety remains at the heart of our profession. The issue opens with an important investigation into inter-centre variability in computed tomography (CT) radiation doses in Nigeria, highlighting the need for protocol harmonization, optimization strategies, and the establishment of locally derived Diagnostic Reference Levels (DRLs). Such studies are particularly valuable in low- and middle-income countries where the expansion of advanced imaging technologies must be accompanied by robust quality assurance and radiation protection programmes. The findings reinforce the critical role medical physicists play in ensuring that technological advancement translates into safer and more effective patient care.

Artificial intelligence continues to reshape every aspect of healthcare, and medical physics is no exception. The professional article, *Medical Physicists in the Age of AI: From Quality Assurance to Governance Assurance*, presents a timely perspective on how our profession is evolving beyond traditional equipment quality assurance toward broader responsibilities in AI validation, lifecycle monitoring, governance, and ethical oversight. As AI-enabled medical devices become increasingly integrated into clinical practice, medical physicists are uniquely positioned to ensure that these technologies remain safe, transparent, equitable, and clinically effective. This transition represents one of the defining opportunities for our profession in the coming decade.

This issue also showcases remarkable advances in radiation oncology and diagnostic imaging. Contributions on online adaptive radiotherapy, Monte Carlo modelling for linear accelerator commissioning, boron neutron capture therapy dosimetry, breast imaging optimization using machine learning, ultrasound quality assessment, and CT dose optimization demonstrate how computational science, advanced modelling, and data-driven methodologies continue to improve clinical decision-making and treatment outcomes. Together, these articles exemplify the multidisciplinary nature of modern medical physics and the increasing convergence of physics, engineering, computer science, and medicine.

Equally inspiring is our Educational Topics article, *For the Love of Medical Physics and Football*, which illustrates how innovative teaching approaches can attract and inspire the next generation of medical physicists. By connecting fundamental physics concepts with the world's most popular sport, the authors demonstrate that education can be both engaging and scientifically rigorous. Such creative educational initiatives are essential for strengthening the future workforce and expanding awareness of the diverse career opportunities available within our profession.

Finally, we are pleased to include a book review on *Understanding Crisis Communication*, a reminder that scientific excellence alone is insufficient without effective communication. Whether communicating with patients, policymakers, healthcare professionals, or the public, medical physicists must increasingly combine technical expertise with clear, evidence-based communication, particularly in an era where misinformation can spread rapidly.

As Co-Editors-in-Chief, we extend our sincere appreciation to all authors, reviewers, and members of the Editorial Board whose dedication and professionalism have made this issue possible. We are equally grateful to the global medical physics community for its continued support of *Medical Physics International*. Your commitment to scientific excellence, education, mentorship, and international cooperation continues to strengthen our profession and improve healthcare worldwide.

We hope the articles in this issue stimulate new ideas, encourage collaboration across regions and disciplines, and inspire continued innovation in research, education, and clinical practice. Together, we remain committed to advancing medical physics for the benefit of patients and society.

Francis Hasford
Sameer Tipnis
Co-Editors-in-Chief
Medical Physics International

Francis Hasford,PhD. FIOMP, FIUPESM
Editor-in-Chief
Radiological and Medical Sciences Research Institute, Ghana Atomic Energy Commission, Accra,Ghana.
haspee@yahoo.co.uk
francis.hasford@gaec.gov.gh

Sameer Tipnis, PhD.DABR,FAAPM
Editor-in-Chief
Department of Radiology and Radiological Sciences, Medical University of South Carolina, Charleston, USA.
tipnis@musc.edu

COLLABORATING ORGANIZATIONS

INTER-CENTRE VARIABILITY IN EFFECTIVE RADIATION DOSE AND THE INFLUENCE OF SCAN PARAMETERS IN ROUTINE COMPUTED TOMOGRAPHY EXAMINATIONS: EVIDENCE FROM THREE DIAGNOSTIC CENTRES IN NORTHWESTERN NIGERIA

B. Maidamma[1,2], I. Maina[2], O.W Olasoji[2], A.M Tijjani[2]

[1] Department of Physics with Electronic, Federal University Birnin Kebbi, Nigeria
[2] Department of Physics, Abubakar Tafawa Balewa University, 740272, Bauchi, Nigeria.

Abstract – **Effective dose is broadly used to estimate the overall stochastic risk associated with computed tomography (CT) examinations and to support dose comparison between scanners/centres. There has been a steady increase in the installation and utilisation of medical imaging modality in Nigeria; however, CT dose monitoring and reporting have not received commensurate attention. This study aimed to compute effective dose values for routine head, chest, and abdominal CT examinations in Sokoto State, Nigeria; evaluate inter-centre variability; and investigate the influence of scan parameters on patient dose. A prospective study was conducted in three different Nigerian Nuclear Regulatory Authority accredited diagnostic centres using multi slice CT scanners. Data from 750 patients, aged 0-80, were collected, including demographic characteristics, scan parameters, and dose length product (DLP). Effective dose was estimated using region-specific conversion coefficients based on International Commission on Radiological Protection (ICRP) 103 recommendations. Inter-centre comparisons were performed, and regression analysis assessed the relationship between effective dose and scan parameters such as tube voltage, tube current, and scan length. This study found significant variation in effective dose between centres for the same CT examinations, reflecting differences in scanner technology, protocol settings, and optimisation practices. Regression analysis identified tube current and scan length as the most influential factors affecting effective dose, though their impact varied by centre. Some effective dose values exceeded international benchmarks, suggesting a need for optimisation. These results highlight the importance of standardised protocols and locally established diagnostic reference levels to improve dose consistency and patient safety in CT practice.**

Keywords – **Effective dose, computed tomography, inter-centre variability, scan parameters, radiation optimisation, Nigeria .**

I. INTRODUCTION

Computed Tomography (CT) is one of the most used diagnostic imaging techniques in modern medicine due to its diagnostic accuracy, speed, and expanding clinical indications (Mahesh, 2013; Maidamma et al., 2026; Yu et al., 2009). CT scans expose patients to ionizing radiation, a known human carcinogen. From 1997 through 2007, CT scans and nuclear medicine procedures became the largest source of exposure to ionizing radiation and accounted for 24% of the exposure in the US population (Maidamma et al., 2026; Sekkat et al., 2025; Shao et al., 2020). It is impractical to directly measure the radiation dose absorbed by individual patients even when the radiation emitted by a machine is precisely known. Instead, radiation exposure may be quantified using various methods, including effective dose (ED) (Smith-Bindman et al., 2009; Trotter et al., 2023; Uniyal et al., 2025). Effective dose is the measure of radiation calculated with the radiosensitivity of specific organs considered. It is measured in Sievert (Sv) (Maidamma et al., 2026; Maidamma & Samaila, 2024). ED was introduced by the International Commission on Radiological Protection (ICRP) for the needs of radiation protection and the assessment of radiation risks, expressed as health detriment due to stochastic effects (Avramova-Cholakova et al., 2022; Dendy & Heaton, 1999; Maidamma et al., 2026; Maidamma & Samaila, 2024; Uniyal et al., 2025; Wang et al., 2022). Although ED was not intended for individual patient risk estimation (Foley et al., 2012; Sekkat et al., 2025; Trotter et al., 2023; Uniyal et al., 2025), it remains an essential tool for body risk assessment, dose benchmarking, and the establishment of diagnostic reference levels (DRLs)(Maidamma & Samaila, 2024; Sekkat et al., 2025). Several studies have demonstrated substantial variations in effective dose for similar CT examinations performed at different centres, often attributable to differences in scan parameters, protocol selection, equipment performance, and operator practice (Einstein et al., 2007; Maidamma et al., 2026; Maidamma & Samaila, 2024). Such inter-centre variability indicates opportunities for optimization and highlights the need for locally generated dose data. In low- and middle-income countries, including Nigeria, data on patient radiation doses from CT examinations remain limited (Garba et al., 2021; Mahesh, 2013; Maidamma & Samaila, 2024), and national DRLs are either absent or based on sparse information. In Sokoto State, CT services are expanding, yet there is little published evidence evaluating effective dose levels across centres or examining whether current practices align with international recommendations (Garba et al., 2021; Mahesh, 2013; Maidamma, 2021). Without such data, it is difficult to assess patient radiation risk, compare local practice with global standards, or identify factors contributing to unnecessarily high doses.

Scan parameters such as tube voltage (kVp), tube current–time product (mAs), scan length, pitch, and the use of automatic exposure control have a direct and significant

influence on radiation dose in CT (Garba et al., 2021; ICRP, 2007; Maidamma et al., 2026). Quantifying the relationship between effective dose and these parameters using statistical methods, including regression analysis, provides valuable insight into the determinants of patient dose and supports evidence-based optimization strategies. This study aims to estimate the effective dose associated with head, chest, and abdominal CT examinations in selected centres in Sokoto State, evaluate inter-centre variability, and compare local dose levels with published literature. Furthermore, the study investigates the influence of key scan parameters on effective dose and employs regression analysis to determine the strength of these relationships.

Theoretical Background

CT scans often involve high radiation doses compared to other imaging procedures, thus monitoring and minimizing the effective dose is essential for optimizing patient safety and complying with international standards set by organizations like the ICRP (Brage et al., 2025; ICRP, 2007; Maidamma et al., 2026). Many scholars give their verdict on the importance of effective dose estimation especially in CT with use of non-ionization radiation that primarily rely on stochastic effect risk.

CT Effective Dose

In CT, the ED helps quantify the stochastic health effects such as cancer and genetic mutations resulting from ionizing radiation (Bąk et al., 2025; Brage et al., 2025; Kalra et al., 2004). Effective dose thus is not a dose metric for a specific individual (Kalra et al., 2004; Zanzonico, 2024). It represents a population-averaged risk estimate, derived from reference phantoms and epidemiological models (Almaasfeh et al., 2023; Arjmandi et al., 2024; Zanzonico, 2024). Recent studies increasingly caution against misuse of effective dose in clinical risk prediction, especially when researchers attempt to relate it directly to tissue-level effects, DNA damage (Albahiti et al., 2022; Almaasfeh et al., 2023; Greene-Schloesser et al., 2012). Effective dose is calculated using the dose-length product (DLP) and region-specific conversion coefficients (k-factors) as show in the equation (Chaparian, 2018; Maidamma et al., 2026).

$$ED = DLP \times k \quad (1)$$ (Maidamma et al., 2026)

Table 1: *k* – Value for CT scan (ICRP, 2007; Maidamma et al., 2026)

Body Region	Adult (≥ 16 Yrs)	Children (15-10 Yrs)	Children (9-2 Yrs)	Infant (1 Yrs)
Head	0.0021	0.0023	0.0042	0.0067
Chest	0.014	0.021	0.026	0.039
Abdomen	0.015	0.019	0.023	0.032

Head CT

Head CT examinations are routinely performed to evaluate intracranial pathologies such as trauma, stroke, haemorrhage, and tumours (ICRP, 2007; Kesmezacar et al., 2026; Maidamma et al., 2026). The procedure typically involves axial acquisition from the skull base to the vertex using relatively high tube current and moderate tube voltage to overcome the high attenuation of the skull bones and achieve adequate contrast resolution (Trotter, 2023; (Chaparian, 2018; Dendy & Heaton, 1999; Kesmezacar et al., 2026; Mahesh, 2013; Maidamma et al., 2026). Consequently, head CT contributes significantly to localised organ absorbed dose despite producing a comparatively lower effective dose than body CT examinations (ICRP, 2007; Maidamma et al., 2026). Dose optimisation strategies such as reduced tube current, appropriate scan length, and lens shielding are therefore critical in head CT imaging (Brage et al., 2025; ICRP, 2007).

Chest CT

Chest CT is widely used for the assessment of pulmonary diseases, mediastinal abnormalities, cardiac conditions, and oncological staging (Brage et al., 2025; Garba et al., 2021; Kesmezacar et al., 2026). Due to the relatively large scan volume and the inclusion of multiple radiosensitive organs, chest CT results in substantial organ absorbed doses, particularly to the lungs, breast, heart, thyroid, and bone marrow (Maidamma et al., 2026). Variations in patient body habitus, scan length, and tube current modulation further influence absorbed dose distribution (Kesmezacar et al., 2026). Optimisation in chest CT is therefore essential, with emphasis on protocol tailoring, automatic exposure control, and careful justification to minimise unnecessary radiation exposure (Barker et al., 2007; Kesmezacar et al., 2026; Maidamma et al., 2026; Sekkat et al., 2025).

Abdominal CT

Abdominal CT examinations are commonly performed to investigate hepatic, gastrointestinal, renal, and pelvic pathologies (Aboul Hamad et al., 2023; Mahesh, 2013; Sekkat et al., 2025). The procedure typically covers a long anatomical range and often employs higher tube current and longer scan times to maintain adequate image quality through soft tissues with varying densities (Aboul Hamad et al., 2023; Mahesh, 2013; Maidamma et al., 2026). Many of these organs have moderate to high tissue weighting factors, indicating a significant contribution to overall radiation risk (Maidamma et al., 2026). Careful optimisation of scan parameters, limitation of scan length, and justification of multiphase studies are essential to reduce unnecessary organ dose while maintaining diagnostic efficacy (ICRP, 2007; Kalender, 2011; Mahesh, 2013; Maidamma et al., 2026).

II. MATERIALS AND METHODS

Study Area

The study was conducted in Sokoto Metropolis, Sokoto State, located in northwestern Nigeria. The state shares borders with the Republic of Niger to the north and west, Zamfara State to the east, and Kebbi State to the south and west. It covers a land area of 28,232.37 square kilometers and lies within the savannah vegetation zone.

Study Population

Eligible participants included male and female patients aged 0–80 years scanned using multi-slice CT systems capable of displaying dose metrics on the console at Usmanu Danfodiyo University Teaching Hospital, Sokoto State advance Medical Diagnostic Centre and Caliphate clinical and Diagnostic Centre; while critically ill patients unable to stand on a floor weighing scale were excluded.

Ethical Consideration

Institutional ethical clearance was obtained from the Ethical Committees of the three participating centers: Usmanu Danfodiyo University Teaching Hospital (UDUTH/HREC/2024/1438/V2), Sokoto State advance Medical Diagnostic Centre (SSAMDC/HREC/2024/01), and Caliphate clinical and Diagnostic Centre (CCDC/HREC/2024/021), with patient consent obtained or waived in accordance with the approved protocols.

Sample size

A total of 900 adult and paediatric patients undergoing routine computed tomography examinations were prospectively recruited from three Nigerian Nuclear Regulatory Authority accredited diagnostic centres, with 300 patients sampled from each centre, in compliance with the European Commission guideline recommending a minimum of 10 patients per CT procedure (Garba et al., 2021; Maidamma et al., 2026).

Study Equipment and Data Collection

The study employed three multi-slice CT scanners of different technological generations a GE LightSpeed 4-slice unit installed in 2011, a Philips Brilliance 16-slice unit installed in 2019, and a GE Brivo-series 16-slice unit installed in 2021. Prior to scanning, patient demographic data such as age, sex, body weight, and height were collected, with weight measured using a calibrated floor scale and height using a measuring tape, while additional information was obtained from medical records or the radiology information system and recorded on a structured data collection form. For each examination, key scan parameters including tube voltage, tube current, and scan length were extracted directly from the scanner console, as these factors significantly influence radiation dose delivery.

Statistical Analysis

All collected data were analysed using Minitab statistical software, where descriptive statistics such as mean, range, standard deviation, and the 75th percentile were computed to characterise patient demographics, scan parameters, and radiation dose metrics and to facilitate inter-centre dose comparison and evaluation.

III. RESULTS

Effective Dose received by the Patients

Individual values of effective dose for all patients were calculated and the mean regional values for each centre were statistically derived (Table 1). The highest average dose was recorded for head CT examinations in Centre A at 3.65 mSv (±2.65), followed by Centre B at 2.31 mSv (±1.36), and Centre C at 1.14 mSv (±0.45). Chest CTs revealed mean doses of 1.68 mSv, 0.69 mSv, and 0.68 mSv in Centres A, B, and C respectively, while abdominal scans yielded relatively lower mean doses ranging from 0.69 mSv to 0.74 mSv across the three centres. These findings demonstrate a consistent pattern, head CT scans deliver the highest radiation doses, followed by chest and abdominal scans Table 4.0. This variation can be attributed to differences in scan protocols, anatomical density, and the length of scanned regions. Head CTs often involve higher tube currents and multiple sequences, resulting in greater exposure (Garba et al., 2021; Maidamma et al., 2026).

Table 2: Mean and SD of Effective Dose (mSv)

Centres	N (no of patients)	Region	E (mSv)
	103	Head	3.65(±2.65)
A	111	Chest	1.68(±1.59)
	86	Abdomen	0.74(±0.30)
	132	Head	2.31(±1.36)
B	114	Chest	0.69(±0.33)
	54	Abdomen	0.74(±0.29)
	132	Head	1.14(±0.45)
C	108	Chest	0.68(±0.36)
	60	Abdomen	0.69(±0.29)
	367	Head	2.25(±1.99)
Total	333	Chest	1.15(±1.22)
	200	Abdomen	0.72(±0.29)

The Relationship Between Patient Age Groups and Effective Dose

The relationship between patient age groups and effective dose in Centre A reveals non-uniform distribution of radiation exposure across age brackets (figure 1a). Particularly, patients in the 20-29 and 30-39 age groups appear to receive higher average doses compared to other cohorts in Centre A reveals non-uniform distribution of radiation exposure across age brackets. Particularly, patients in the 20-19 and 30-39 age groups appear to receive higher average doses compared to other cohorts. This is a critical finding given that younger patients (especially those 20 years) are more radiosensitive due to active cellular division and longer remaining lifespans, factors that substantially elevate their lifetime attributable risk (LAR) of cancer, as established by the BEIR VII model.

Figure 1a,b&c: Effective dose against age group in study Centres

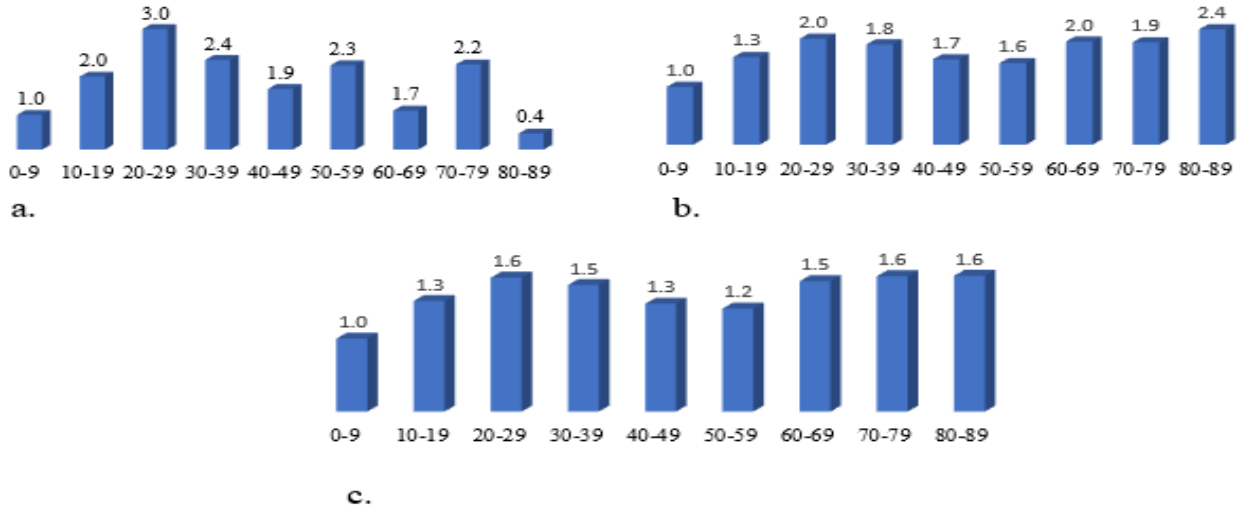

Figure 1b, shows a more consistent dose distribution across age groups compared to Centre A, with effective doses some remaining below the 2 mSv for most age ranges. The highest doses are seen in patients aged 20–29 and 80–89, but even these remain within the lower-risk category as defined by international radiological protection agencies. There remains concern for young patients, particularly in the 0-9 and 10-19 age groups, where any non-essential exposure must be carefully justified. Overall, Centre B demonstrates moderate compliance with dose safety standards, but continuous review and individualized scanning protocols remain essential for long-term patient protection. Centre C, Figure 1c, the dose distribution across age groups indicates the consistent overall exposure among all three centres. Most patient categories received effective doses well below 2 mSv, including those undergoing head, chest, and abdominal CT scans. Despite the lower absolute doses, special attention must still be paid to younger patients (0-19 years) due to their increased susceptibility to radiation-induced carcinogenesis. Although the effective doses in Centre C, are commendable, ongoing surveillance is warranted to ensure consistency across varying body habitus and clinical indications. In conclusion, Centre C's age dose demonstrates commendable performance in minimizing radiation burden, setting a reference standard for the other centres in terms of clinical protocol design and patient safety assurance.

Comparison of centres effective dose with literature

A comparative analysis of the average ED (mSv) for CT examinations across the three anatomical regions (Head, Chest, and Abdomen) performed at three local centres (Centre A, Centre B, and Centre C), benchmarked against established values from selected peer-reviewed literature. ED for head CT scans at Centre A (3.8 mSv) is notably higher than those recorded at Centre B (2.3 mSv) and Centre C (1.1 mSv). When compared to international standards, the value from Centre A closely aligns with the dose reported by (Smith-Bindman et al., 2009) who reported a mean of 3.0 mSv for adult head CT. However, doses from Centre C are substantially lower and are consistent with the findings of (Zamani et al., 2025) and (Virginia Tsapaki et al., 2006) who documented head CT doses of 1.1 mSv and 1.2 mSv, respectively. This variation suggests potential differences in scan protocols, scanner models, and exposure settings (mA, kV, and SL) between local centres, highlighting a possible optimization strategy. Chest CT EDs at the local centres range from 0.7 mSv (Centres B and C) to 1.7 mSv (Centre A). These values are substantially lower than those reported in literature. For instance, (Al-OThman, 2022) and (Smith-Bindman et al., 2009) reported mean doses of 7.3 mSv and 5.0 mSv, respectively.

Abdominal CT Examinations: similarly, EDs for abdominal CT at the local centres 1.8 mSv (Centre A), 0.7 mSv (Centre B), and 0.8 mSv (Centre C) are markedly lower than literature value. The dose from Centre A is the highest among the local centres but still significantly reduced compared to published standards. This trend reinforces the possibility that current CT protocols at the study centres have been optimized for dose reduction without compromising diagnostic utility. Several patients undergoing head CT at UDUTHS received doses ranging from approximately 3.2 to 6.5 mSv, closely matching the average of 3.8 mSv. In contrast, patients scanned at other centres (CCDCS and SSAMDCS) show lower values, consistent with Centres B and C. The wide range of abdominal scan doses, primarily between 0.7 and 2.4 mSv across the dataset, further confirms the lower average values reported in Table 2. Thus, the data provides strong quantitative support for the dose optimization conclusions drawn from Table 3.

Table 3: Comparison of Effective Dose with Literature

Studies	E (mSv) Scan Region		
Centres/Studies	**Head**	**Chest**	**Abdomen**
Centre A	3.8	1.7	1.8
Centre B	2.3	0.7	0.7
Centre C	1.1	0.7	0.8
(Abdullah et al., 2022)	1.8	4.2	8.7
(Al-OThman, 2022)	1.7	7.3	10
(V. Tsapaki et al., 2006)	1.2	5.9	8.2
(Zamani et al., 2025)	1.1	3.7	5.8
(R. Smith-Bindman et al., 2009)	3.0	5.0	10

Comparison of E (mSv) with Scan Parameters

For Centre A, the multiple linear regression model relating effective dose (E) to tube voltage (kV), tube current (mA), and scan length (SL) is given by: E = 1.292 − 0.00264kV + 0.002683mA − 0.01392SL. The overall regression model is statistically significant (F = 29.3, p < 0.001), indicating that the selected scan parameters collectively explain a meaningful proportion of the variation in effective dose. The coefficient of determination (r^2 = 25.4%, shows that approximately one-quarter of the variability in patient effective dose can be explained by changes in kV, mA, and scan length in these centres. Centre B, the regression equation is expressed as; E = −6.01 + 0.0651kV + 0.00735mA − 0.0494SL, and the model demonstrates strong statistical significance (F = 76.70, p < 0.001). The coefficient of determination (r^2 = 47.70%) indicates that nearly half of the variation in effective dose is explained by the three scan parameters. For Centre C, the regression model is:

E = 1.74 + 0.0019kV − 0.00464mA − 0.00478SL,

with the overall model reaching statistical significance (F = 3.58, p = 0.014). However, the explanatory power of the model is very low, with r^2 = 3.03%, indicating that scan parameters explain only a small fraction of the variability in effective dose at this centre. This inverse trend may reflect the influence of advanced automatic exposure control and dose modulation technologies in this newer GE Brivo 16-slice scanner, where increases in mA may occur selectively for larger patients while overall dose efficiency is maintained (Table 4).

Table 4: Regression analysis of Effective dose against Scan Parameters

Centres	*F- value*	r^2	*P-value*
A	29.3	25.4	0.000
B	76.7	47.7	0.000
C	3.58	3.03	0.014

IV. DISCUSSION

Comparatively, Centre B shows the strongest and most predictable relationship between effective dose and scan parameters. Centre A shows moderate dependence with room for optimisation, while Centre C demonstrates advanced technology-driven dose modulation where traditional linear parameter–dose relationships are less dominant. These findings emphasise the importance of centre-specific optimisation strategies and support the development of local Diagnostic Reference Levels (DRLs) tailored to scanner technology and clinical practice in Sokoto State.

Relationship Between ED (mSv) and Scan Parameters in Centre A

Figure 2, the scatter plots with fitted regression lines demonstrate a clear upward trend between effective dose and mA, while kV shows weak dispersion and scan length shows a modest inverse trend. The presence of several large residuals indicates inter-patient variability and reinforces the need for further optimisation and protocol harmonisation in Centre A.

Figure 2: Regression graph of E (mSv) against Scan Parameters in Centre A

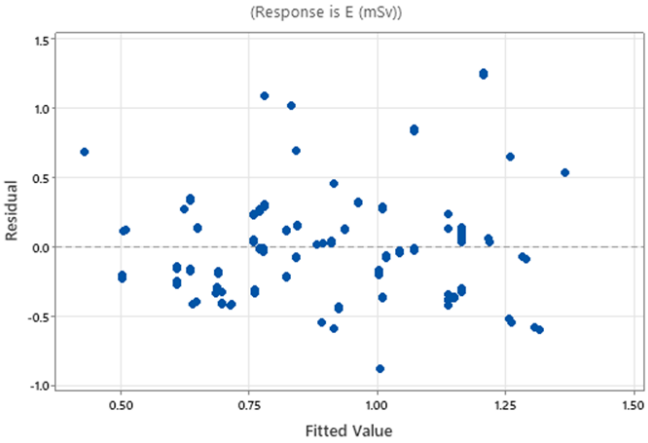

Relationship Between ED (mSv) and Scan Parameters in Centre B

Figure 3, the regression plots for Centre B show well defined linear trends, particularly for kV and mA, with relatively narrow scatter around the fitted lines. The lack of fit test is not significant, indicating that the linear model adequately describes the data. However, a few extreme residuals point to occasional protocol deviations or atypical patient examinations, which merit quality assurance review. Overall, Centre B demonstrates the most optimised and predictable relationship between scan parameters and effective dose.

Relationship Between ED (mSv) and Scan Parameters in Centre C

Figure 4, the scatter plots for Centre C show wide dispersion and weak linear trends, consistent with the low r^2 values. Numerous large residuals highlight substantial inter-patient and protocol-driven variability. This suggests that in Centre C, effective dose is more strongly influenced by patient-specific factors, reconstruction algorithms, and vendor-specific dose-reduction technologies than by simple scan parameter settings alone.

Figure 3: Regression graph of E (mSv) against Scan Parameters in Centre B

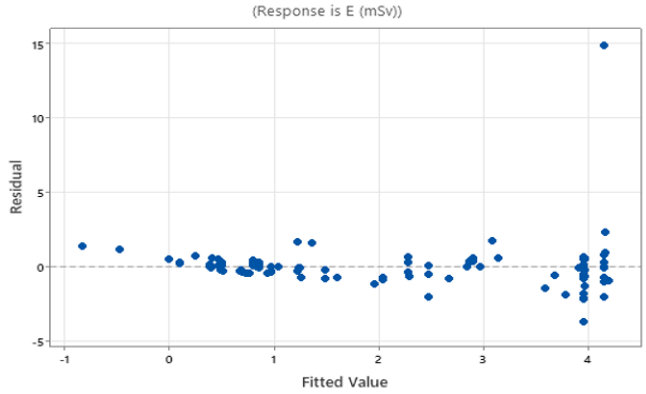

Figure 4: Regression graph of E (mSv) against Scan Parameters in Centre C

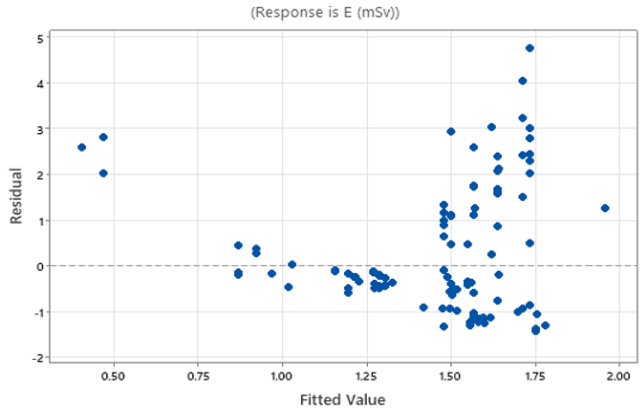

V. CONCLUSION

This study revealed substantial inter-centre variability in effective dose for routine CT examinations in Sokoto State despite comparable clinical indications. These differences were primarily driven by variations in scan parameters, scanner technology, and protocol. Regression analysis identified tube current and scan length as the principal determinants of effective dose, although their influence varied across centres, reflecting differences in dose modulation and optimisation practices. Comparison with international literature indicates that while some centres operate within global benchmarks, others demonstrate clear potential for dose optimisation. These findings underscore the need for continuous dose monitoring, protocol standardisation, and targeted staff training to reduce unnecessary radiation exposure. The establishment of locally derived diagnostic reference levels based on measured effective dose values would provide a critical framework for quality assurance and optimisation in Nigeria. Overall, the study highlights the utility of effective dose as a population-level metric for comparison while emphasising the importance of centre-specific optimisation to ensure safe and effective CT practice.

VI. ACKNOWLEDGEMENT

All authors wish to express their sincere gratitude to all individuals and institutions whose contributions, support, and cooperation were instrumental to the successful completion of this study.

VII. REFERENCES

Al-OThman, A. (2022). Radiation Dose Optimization for Routine Radiological Studies Using Computed Tomography: A Comparison Based on National Dose Reference Levels and Effective Dose Calculation Alfaisal University (Saudi Arabia)].

Albahiti, S. K., Barnawi, R. A., Alsafi, K., Khafaji, M., Aljondi, R., Alghamdi, S. S., Awan, Z., Sulieman, A., Jafer, M., Tamam, N., Tajaldeen, A., Mattar, E. H., Al-Malki, K. M., & Bradley, D. (2022). Establishment of institutional diagnostic reference levels for 6 adult computed tomography examinations: Results from preliminary data collection. *Radiation Physics and Chemistry*, *201*, 110477. https://doi.org/https://doi.org/10.1016/j.radphyschem.2022.110477

Almaasfeh, S., Salahudeen, A., Salih, M., & Abukonna, A. (2023). Estimation of effective and organ dose from chest CT. *Radiation Physics and Chemistry*, *204*, 110646. https://doi.org/https://doi.org/10.1016/j.radphyschem.2022.110646

Arjmandi, N., Momennezhad, M., Arastouei, S., Mosleh-Shirazi, M. A., Albawi, A., Pishevar, Z., & Nasseri, S. (2024). Deep learning-based automated liver contouring using a small sample of radiotherapy planning computed tomography images. *Radiography*, *30*(5), 1442–1450. https://doi.org/https://doi.org/10.1016/j.radi.2024.08.005

Avramova-Cholakova, S., Dyakov, I., Yordanov, H., & O'Sullivan, J. (2022). Comparison of patient effective doses from multiple CT examinations based on different calculation methods. *Physica Medica*, *99*, 73–84.

Bąk, B., Kaczmarek, K., Radoła, D., Winiecki, T., & Bajon, T. (2025). A prospective study of bladder volume assessment using ultrasound in prostate cancer radiotherapy: Comparison with cone-beam computed tomography (CBCT). *Radiography*, *31*(5), 103016. https://doi.org/https://doi.org/10.1016/j.radi.2025.103016

Barker, N., Van Es, J. H., Kuipers, J., Kujala, P., Van Den Born, M., Cozijnsen, M., Haegebarth, A., Korving, J., Begthel, H., & Peters, P. J. (2007). Identification of stem cells in small intestine and colon by marker gene Lgr5. *Nature*, *449*(7165), 1003–1007.

Brage, K., Pedersen, M. R. V., Lauridsen, C. A., Paulo, C., Hansen, P., Precht, H., Addi, A. J., & Jensen, J. (2025). Reporting radiographers in CT and MRI: A literature review with a systematic approach. *Radiography*, *31*(2), 102901. https://doi.org/https://doi.org/10.1016/j.radi.2025.102901

Chaparian, A. (2018). Assessment of radiation-induced cancer risk to patients undergoing computed tomography angiography scans.

Dendy, P. P., & Heaton, B. (1999). *Physics for diagnostic radiology*. CRC press.

Einstein, A. J., Henzlova, M. J., & Rajagopalan, S. (2007). Estimating risk of cancer associated with radiation exposure from 64-slice computed tomography coronary angiography. *Jama*, *298*(3), 317–323.

Foley, S. J., McEntee, M. F., & Rainford, L. A. (2012). Establishment of CT diagnostic reference levels in Ireland. *The British journal of radiology*, *85*(1018), 1390–1397.

Garba, I., Zarb, F., McEntee, M. F., & Fabri, S. G. (2021). Computed tomography diagnostic reference levels for adult brain, chest and abdominal examinations: A systematic review. *Radiography*, *27*(2), 673–681. https://doi.org/https://doi.org/10.1016/j.radi.2020.08.011

Greene-Schloesser, D., Robbins, M. E., Peiffer, A. M., Shaw, E. G., Wheeler, K. T., & Chan, M. D. (2012). Radiation-induced brain injury: a review. *Frontiers in oncology*, *2*, 73.

ICRP. (2007). Preface, executive summary and glossary. *Annals of the ICRP*, *37*(2-4), 9–34.

Kalender, W. A. (2011). *Computed tomography: fundamentals, system technology, image quality, applications*. John Wiley & Sons.

Kalra, M. K., Maher, M. M., Toth, T. L., Hamberg, L. M., Blake, M. A., Shepard, J.-A., & Saini, S. (2004). Strategies for CT radiation dose optimization. *Radiology*, *230*(3), 619–628.

Kesmezacar, F. F., Günay, O., Kayaokay, D. T., Yeyin, N., Demirci, A., Karaçam, S. Ç., Öksüz, D. Ç., Demir, M., Almisned, G., Karadağ, T., Alkarrani, H., Issa, B., & Tekin, H. O. (2026). Radiation dose variability in critical thoracic organs during CT imaging: A multi-centre phantom dosimetry study. *Radiation Physics and Chemistry*, *238*, 113174. https://doi.org/https://doi.org/10.1016/j.radphyschem.2025.113174

Mahesh, M. (2013). The Essential Physics of Medical Imaging, Third Edition. *Med Phys*, *40*(7). https://doi.org/10.1118/1.4811156

Maidamma, B. (2021). Estimation of Dose Reference Values for Patients Undergoing Chest and Abdomen Computed Tomography Scan in Sokoto, Nigeria. *International Journal of Science and Research (IJSR)*, *10*(6), 1563–1566. https://doi.org/https://dx.doi.org/10.21275/MR21622173253

Maidamma, B., Maina, I., Tijjani, A. M., Benabdallah, F., El-Rayyes, A., & Iliyasu, U. (2026). Assessment of organ-specific radiation risk in computed tomography examination using the ratio of absorbed organ dose to total effective dose in Sokoto State CT centres. *Radiation Physics and Chemistry*, *246*, 113912. https://doi.org/https://doi.org/10.1016/j.radphyschem.2026.113912

Maidamma, B., & Samaila, B. (2024). Estimation of Cancer Risk Associated With Patients Undergoing Brain Computed Tomography Scan in Sokoto, Nigeria. *International Journal of Medical Physics, Clinical Engineering and Radiation Oncology*, *12*, 151–153.

Sekkat, H., Khallouqi, A., El rhazouani, O., Halimi, A., & Madkouri, Y. (2025). HeadCTDosi: A python-based automated calculation of head water equivalent diameter and size specific dose estimate based on AAPM 220 report. *Radiation Physics and Chemistry*, *227*, 112388. https://doi.org/https://doi.org/10.1016/j.radphyschem.2024.112388

Shao, Y.-H., Tsai, K., Kim, S., Wu, Y.-J., & Demissie, K. (2020). Exposure to tomographic scans and cancer risks. *JNCI cancer spectrum*, *4*(1), pkz072.

Smith-Bindman, Rebecca Lipson, Jafi Marcus, Ralph Kim, Kwang-Pyo Mahesh, M. G., Robert De González, & Amy Berrington Miglioretti, D. L. (2009). Radiation dose associated with common computed tomography examinations and the associated lifetime attributable risk of cancer. *Archives of internal medicine*, *169*(22), 2078–2086.

Smith-Bindman, R., Lipson, J., Marcus, R., Kim, K.-P., Mahesh, M., Gould, R., Berrington de González, A., & Miglioretti, D. L. (2009). Radiation Dose Associated With Common Computed Tomography Examinations and the Associated Lifetime Attributable Risk of Cancer. *Archives of Internal Medicine*, *169*(22), 2078–2086. https://doi.org/10.1001/archinternmed.2009.427

Trotter, J., Pantel, A. R., Teo, B.-K. K., Escorcia, F. E., Li, T., Pryma, D. A., & Taunk, N. K. (2023). Positron Emission Tomography (PET)/Computed Tomography (CT) Imaging in Radiation Therapy Treatment Planning: A Review of PET Imaging Tracers and Methods to Incorporate PET/CT. *Advances in Radiation Oncology*, *8*(5), 101212. https://doi.org/https://doi.org/10.1016/j.adro.2023.101212

Tsapaki, V., Aldrich, J. E., Sharma, R., Staniszewska, M. A., Krisanachinda, A., Rehani, M., Hufton, A., Triantopoulou, C., Maniatis, P. N., & Papailiou, J. (2006). Dose reduction in CT while maintaining diagnostic confidence: diagnostic reference levels at routine head, chest, and abdominal CT—IAEA-coordinated research project. *Radiology*, *240*(3), 828–834.

Tsapaki, V., John, E. A., Sharma, S., Staniszewska, M., A., , Anchali K., Rehani, M., M., , Hufton, A., Chariklia T., Petros N, M., Papailiou, J., & P., M. (2006). *Dose Reduction in CT while Maintaining Diagnostic Confidence: Diagnostic Reference Levels at Routine Head, Chest, and Abdominal CT—IAEA-coordinated Research Project1* (www.rsna.org/rsnarights, Issue. 2006.

Uniyal, S. C., Prasad, M., & Raghuvanshi, S. (2025). Patient dose survey and determination of diagnostic reference levels for routine computed tomography examinations in Uttarakhand, India. *Applied Radiation and Isotopes*, *222*, 111875. https://doi.org/https://doi.org/10.1016/j.apradiso.2025.111875

Wang, K., Malkin, H. E., Patchett, N. D., Pearlstein, K. A., Heiling, H. M., McCabe, S. D., Deal, A. M., Mavroidis, P., Oakey, M., Fenoli, J., Lee, C. B., Klein, J. L., Jensen, B. C., Stinchcombe, T. E., Marks, L. B., & Weiner, A. A. (2022). Coronary Artery Calcifications and Cardiac Risk After Radiation Therapy for Stage III Lung Cancer. *Int J Radiat Oncol Biol Phys*, *112*(1), 188–196. https://doi.org/10.1016/j.ijrobp.2021.08.017

Yu, L., Liu, X., Leng, S., Kofler, J. M., Ramirez-Giraldo, J. C., Qu, M., Christner, J., Fletcher, J. G., & McCollough, C. H. (2009). Radiation dose reduction in computed tomography: techniques and future perspective. *Imaging in medicine*, *1*(1), 65.

Zamani, H., Yektamanesh, M., Shiridokht, F., Sharifian Jazi, S., Javadrashid, R., Ghasemi Jangjoo, A., Molazadeh, M., Farajollahi, A., & Mortezazadeh, T. (2025). Estimation of effective dose and risk of exposure-induced cancer death, and diagnostic reference level for CT scans in Tabriz, Iran. *Radiological Physics and Technology*, *18*(1), 186–195.

Zanzonico, P. (2024). The MIRD schema for radiopharmaceutical dosimetry: a review. *Journal of Nuclear Medicine Technology*, *52*(2), 74–85.

Contacts of the corresponding author:
Authors: Buhari Maidamma
Institute: Federal University Birnin Kebbi
Country: Bulgaria
Email: buharizimber@gmail.com

EDUCATIONAL TOPICS

FOR THE LOVE OF MEDICAL PHYSICS AND FOOTBALL

I.B. Uwadiae[1], O.D. Adekanbi[2], P.O. Emmanuel[3], E.M. Olaigbe [4]

[1] University College Hospital, Ibadan, Nigeria
[2] University of Ibadan, Ibadan, Nigeria
[3] Federal University of Agriculture, Abeokuta, Nigeria
[4] Ladoke Akintola University of Technology, Ogbomoso, Nigeria

Abstract—**Engaging and exposing students to various applications of physics for the improvement of health, can be fun and productive. This study was done to broaden students' view of medical physics, showing its applications beyond traditional healthcare settings and encouraging them to consider it as a career, using the sports they love as a tool.**

Keywords—**Football, Medical Physics, Physiological Measurements.**

I. INTRODUCTION

How do you explain the applications of physics in medicine to a group of undergraduate students who are new to the idea and have a 'not so interesting time' understanding its relevance? What happens when both the students and their supervisor love and play football? A good approach is to leverage their interests as an opportunity to introduce and clarify the less familiar aspects of medical physics.

Medical Physics is an interesting field of study that intercepts physics and medicine. It applies the theoretical and experimental principles of physics in medicine for the diagnosis and treatment of diseases. It has existed for as long as the discovery of X-rays and radioactivity by Wilhelm Roentgen and Marie Curie respectively while the applications of physics in medicine dates to the very beginning of life. However, the profession started to become popular when the complexity of physics applications in medicine required high level of specialised scientists, the physicists themselves [1,2]. Internationally, Medical Physics as a profession is promoted and overseen by the International Organisation for Medical Physics (IOMP), established in 1963 and it is recognised by the International Labour Organisation (ILO) formally as a health profession [3]. Over the years, the specialties of medical physics in health care have expanded from the applications of ionizing and non-ionizing radiation to physiological measurements, rehabilitation, orthopaedics, audiology, and the list goes on.

Football, also known as soccer mainly in North America, is undoubtedly the most popular and most watched sport in the world [4]. Though widely seen as an art of teamwork and instinct, it is fundamentally a science of motion, force, and energy. Physics governs every action on the pitch, from the curved trajectory of a free kick to the impact force of a tackle and the acceleration of a sprint. It is a wholesome sport that combines various other 'mini' sports like athletics, running, throwing, and kicking. These activities are all governed by the principles of physics. Physics principles like Newton's laws, gravitational force, projectile motion, kinetic energy, potential energy, impulse, friction, momentum, torque, and angular velocity.

One branch of medical physics that has applications in football is physiological measurements. Physiological measurements involve taking measurements of how the body functions and these can be very simple measurements from taking the temperature of the body with a clinical thermometer to much more complicated measurements like ECG and brain functions [5,6]. These measurements are used for diagnosis and monitoring using various methods and tools.

The advancement of technology especially in the areas of development of wearable devices for measurement of players health and performance has greatly improved performance monitoring [7]. These devices help to check metrics like heart rates, temperature, player speed, velocity, distance covered, and so on. Concepts all grounded in the principles of physics. Data collected with the help of these devices connected to a phone app or computer, help to track health status players in real time to evaluate performance, prevent injuries or other health complications.

Teaching and learning medical physics need not be boring and so the objective of this study was to highlight and demonstrate practically, the intersection of medical physics and football amongst a group of undergraduate students, to help their understanding of the field with the hope that they will consider taking up medical physics as a career. Common physiological factors affecting player' performance were collected and analysed during which there were teaching moments explaining the 'limitless' opportunities physics has beyond the hospital.

II. MATERIALS AND METHODS

Football teams of university students competing at the 2025 annual freshmen vs seniors' competition at the University of Ibadan, Nigeria were used for the study. Two different designs of four smart watches (Fig. 1) were used: the M4 Smart Bracelet (watch A) and the Kingnote Smart watch (watch B). The M4 Smart Bracelet features a 0.96-inch color touch screen, and it includes basic health monitoring capabilities such as heart rate and sleep tracking. The Kingnote Smart watch provides functions such as heart rate, blood pressure, sleep, and blood oxygen monitoring. Prior to

use, both devices were calibrated by downloading their respective applications from the application store on four android phones. The watches were paired with corresponding phones. Each team comprised of the standard 11 team members (10 players, 1 goalkeeper). Due to the simplicity and lightweight of watch A, it was assigned to the players, one per opposing team, per match. Watch B was assigned to two linesmen per match. The players who were assigned the watches were selected based on their activity level in a match e.g. striker or midfielder. This configuration enabled simultaneous collection of physiological and activity data from both teams and the match official under similar environmental and game play conditions. Eight matches in total were observed.

The match comprised two halves of 30 minutes each, with a short interval between halves. During gameplay, the players engaged in regular football activities, including running, passing, tackling, and shooting. The linesman performed normal officiating duties, running along the sidelines to monitor offside positions.

Before the commencement of the match, screenshots of the readings on the smart watch applications were taken and stored for reference. During the game, all physical activities were observed, and key events were recorded in the order they occurred to create a clear timeline of actions. After the match, all data recorded from the players and the linesmen were gathered and saved. The parameters included Blood pressure(mmHg), Heart rate(bpm), Distance covered (km), Blood oxygen (%), and time(min).

Once data collection was completed, the students, who are also the co-authors of this study, participated in an interactive session where they examined physiological measurements gathered during football matches. The supervisor (lead author) discussed the results, connecting the physical challenges of football with the physiological responses recorded by the smart devices. By linking these practical observations to key physics concepts such as energy use, cardiovascular activity, and biomechanics, the session sparked engaging conversations. The students and interested players, were invited to pose questions, discuss their perspectives, and explore how similar measurement methods are used in medical and sports environments to track health and enhance performance.

Fig. 1 Smart Watches - M4 Smart Bracelet (left) and the Kingnote Smart watch (right).

III. RESULTS AND DISCUSSION

Table 1 presents physiological data for 16 linesmen, with each row representing an individual and the columns detailing the following metrics: serial number (S/N), distance covered (Km), heart rate (beats per minute, BPM), time (min), blood pressure (mmHg), and blood oxygen saturation (%).

The distance covered by the linesmen varied widely, ranging from as little as 0.53 km (linesman 14) and 0.56 km (linesman 16), up to 3.74 km (linesman 12). Most of them covered between 1.44 km and 3.74 km, suggesting variations in either patrol time or activity level. Linesmen who covered longer distances (3 and 12) generally had longer patrol times and maintained heart rates within the lower end of the observed range. The lowest distances covered corresponded to the shortest patrol times (linesmen 14 and 16), which may be due to the time used to manage substitutions, reduced activity, or different tracking roles.

Table 1 Physiological Data from the Linesmen

S/N	Distance Covered (Km)	Heart rate (BPM)	Time (min)	Blood Pressure (mmHg)	Blood Oxygen (%)
1	3.08	84	33	126/76	97
2	2.22	88	58	100/71	97
3	3.63	83	76	100/71	97
4	2.41	83	69	126/76	97
5	2.91	83	68	100//71	97
6	1.93	89	76	110/79	97
7	1.94	83	69	121/76	95
8	3.23	83	78	113/77	97
9	2.12	88	61	113/77	97
10	1.73	83	68	121/76	95
11	1.44	88	77	115/70	96
12	3.74	87	95	115/70	97
13	1.65	83	60	121/76	95
14	0.53	83	48	121/76	95
15	2.24	88	91	126/76	96
16	0.56	88	36	126/76	96
Mean (SD)	2.21 (0.95)	85.25 (2.54)	66.44 (17.11)	116/75 (9/3)	96 (0.85)

Heart rates were generally clustered between 83 and 89 BPM, with several linesmen (2, 9, 11, 15, 16) recording 88 BPM. The highest heart rate was 89 BPM (linesman 6), and the lowest was 83 BPM, which was the most common value. There was significant variation in patrol time, with the lowest being 36 mins (linesman 16) and the highest being 95 mins (linesman 12). Most linesmen had times between 48 and 95 mins, indicating differences in patrolling or tracking offsides. The blood pressure readings fluctuated across board, with common values being 121/76 mmHg, 126/76 mmHg, 100/71 mmHg, 113/77 mmHg, 115/70 mmHg, and 110/79 mmHg.

Most readings fell within the normal adult range, with no values indicating hypertension or hypotension. Oxygen saturation levels were consistently high, ranging from 95% to 97%, which is within the normal healthy range. Most linesmen had readings of 97%, indicating good oxygenation during activity. Blood pressure and oxygen saturation remained stable across all players, suggesting that the physical exertion did not cause significant physiological stress or compromise cardiovascular/respiratory function. Heart rate did not show a strong direct correlation with distance covered or playing time, remaining relatively stable across the dataset.

Overall, the data in table 1 showed that the linesmen maintained healthy physiological profiles during the game. Most of them had normal blood pressure and high oxygen saturation, regardless of the distance covered or playing time. This suggests good cardiovascular and respiratory fitness among the group, with individual variations likely reflecting differences in intensity of participation.

Table 2 Physiological Data from the Players

S/N	Distance Covered (Km)	Heart rate (BPM)	Time (min)	Blood Pressure (mmHg)	Blood Oxygen (%)
1	4.50	79	34	109/75	97
2	7.30	93	72	127/96	97
3	6.50	90	85	106/79	98
4	8.60	73	73	123/76	97
5	7.24	74	73	111/72	97
6	6.90	90	71	106/79	98
7	6.50	74	88	118/84	97
8	5.80	74	74	118/84	97
9	7.60	93	75	115/70	97
10	5.80	79	70	108/64	97
11	5.00	81	70	110/76	97
12	3.25	78	50	108/75	96
13	3.42	85	30	111/80	99
14	5.10	73	103	117/68	98
15	5.12	87	90	107/78	98
16	4.56	89	103	101/76	98
Mean (SD)	5.82 (1.47)	82 (7)	72.56 (20)	112/77 (7/7)	97.37 (0.72)

Table 2 presents data for 16 players, documenting the distance covered (Km), heart rate (BPM), time (mins), blood pressure (mmHg), and blood oxygen saturation (%) for each entry. The distances covered by the players ranged from 3.25 km to 8.6 km, showing a broad variation in the performance of players and indicating moderate to high activity levels among most of them. Players with higher distances generally had higher heart rates and spent more time, as expected. There were a few players for example players 14 and 16 with only 5.10 km and 4.56 Km respectively, in 103 mins, who covered relatively shorter distances in long times, possibly indicating lower fitness, a walking pace, or breaks during the match.

The heart rates ranged from 73 to 93 BPM. Higher heart rates were generally seen in players who covered greater distances or spent more time, as expected due to increased cardiovascular demand. However, some outliers exist, such as player 4 (8.6 km, 73 BPM) indicating good cardiovascular fitness or pacing strategy. The time spent varied significantly (from 30 to 103 mins). Those covering longer distances generally took more time, but some players (e.g. player 4, 8.6 km in 73 minutes) were able to cover more ground in less time, suggesting higher speed or intensity. The blood pressure readings were within normal range, with systolic values between 101mmHg and 127 mmHg and diastolic values between 64 mmHg and 96 mmHg. There was no clear trend correlating higher activity with significantly higher blood pressure, which is typical in healthy and physically fit individuals. The blood oxygen levels were consistently high, mostly between 96% and 99%, indicating efficient oxygen uptake and delivery during physical activity. All players maintained healthy oxygen levels, indicating adequate aerobic response.

This data demonstrates a positive relationship between distance covered and heart rate/time, as would be expected during physical exertion. The physiological parameters (blood pressure and oxygen saturation) remain within healthy ranges for all players, indicating no adverse responses to the activity with individual variations likely reflecting differences in playing position, duration, and intensity of participation.

To further inspire students about the discipline, the supervisor showcased the wide range of careers available in medical physics. The description of how skills like data analysis, utilising wearable technology, and interpreting physiological data are directly relevant to work in hospitals, research, sports science, and medical device development was done. Real-world examples included medical physicists collaborating with athletes, creating diagnostic tools, and improving patient care. This strategy allowed students to view medical physics not only as a subject of study, but as a vibrant career that connects their interest in sports with a meaningful opportunity to advance health outcomes. Additional questions were raised by the students and even some of the players. Some of the questions and responses are presented below:

1. How do the principles of physics, apply to the actions performed during a football match?
   Response: *Physics governs every action on the pitch. For example, Newton's laws explain how a player accelerates, kicks, or collides with another player. The curved trajectory of a free kick is a result of projectile motion and angular velocity, while the impact force of a tackle involves momentum and impulse. These principles help analyse and optimise player movements and strategies.*

2. How can data collected from wearable technology during football matches be used to prevent injuries or optimise player performance
   Response: *The data allows coaches and medical staff to monitor players' cardiovascular and respiratory responses. For example, consistently high heart rates or abnormal blood pressure readings can indicate fatigue or risk of overexertion, prompting timely substitutions or adjustments in training. Stable oxygen saturation and blood pressure, as observed in the study, indicate healthy responses to exertion.*
3. In what ways does medical physics contribute to the design and improvement of sports equipment and wearable devices used in football?
   Response: *Medical physics principles are used to develop and calibrate sensors in wearable devices, ensuring accurate measurement of physiological parameters.*
4. What career opportunities exist for medical physicists in the field of sports, particularly football?
   Response: *Medical physicists can work in sports science, rehabilitation, and medical device development. Their expertise in physiological measurement and data analysis is valuable for monitoring athlete health, optimising performance, and designing new technologies. medical physics offers diverse career paths beyond traditional clinical settings.*
5. How can the study of biomechanics, a branch of medical physics, improve training techniques and reduce the risk of injury in football?
   Response: *Biomechanics analyses movement patterns, force application, and joint stress. By studying these aspects, coaches and medical physicists can optimize running and kicking techniques, reducing injury risk and improving efficiency. Football activities like running, kicking, and tackling are governed by physics principles, making biomechanics essential for performance enhancement and injury prevention*

After the interactive session, the students were asked if they would strongly consider careers in medical physics after being exposed to its applications both in the hospital and in sports. They all responded in the affirmative. Two of them who are acive football players were particularly pleased and relieved to know that their physics degrees, and interest in medicine, could be directly linked to what they already love doing making medical physics more relatable.

IV. CONCLUSIONS

Integrating football into the study of medical physics provides a relatable approach for undergraduate students who love the sport to appreciate the practical applications of physics in medicine. Medical physicists possess a solid a foundation in physics, which enables them to clearly explain and analyses the principles underlying sports. Their expertise allows them to contribute meaningfully to both the performance outcomes of games and the health and well-being of athletes. By utilising wearable technology and analysing physiological data during real matches, students gain hands-on experience that bridges theoretical concepts with real-world scenarios. This method not only enhances their understanding and engagement but also broadens their perspective on the scope of medical physics, encouraging them to explore diverse career opportunities within the field. The data supports the use of these variables as effective markers for monitoring exercise intensity and players' health.

V. ACKNOWLEDGMENT

The authors acknowledge the football teams of the male halls of residence of the University of Ibadan who were kind enough to volunteer for this study.

VI. REFERENCES

1. Duck F et al. (2014) The origins of medical physics. Physica Medica: European Journal of Medical Physics, 30, 397-402
2. Endo M. (2021) History of medical physics. Radiol Phys Technol. 14(4):345-357. doi: 10.1007/s12194-021-00642-2.
3. Nüsslin, F. and Smith, P. (2011) Medical Physics now classified internationally as a profession. Med. Phys., 38: i-i. https://doi.org/10.1118/1.3605469
4. World Atlas at https://www.worldatlas.com/articles/what-are-the-most-popular-sports-in-the-world.html.
5. Dan Clark (2021) An Introduction to Physiological Measurement. Available at: https://www.youtube.com/watch?v=gMDY2FmbV0M
6. IPEM: What do our members do? Available at https://www.ipem.ac.uk/about/what-do-our-members-do/clinical-engineering/physiological-measurement/)
7. Migliaccio, G.M.; Padulo, J.; Russo, L. (2024) The Impact of Wearable Technologies on Marginal Gains in Sports Performance: An Integrative Overview on Advances in Sports, Exercise, and Health. *Appl. Sci. 14*, 6649. https://doi.org/10.3390/app14156649),

Contacts of the corresponding author:

Author: Iyobosa B. Uwadiae
Institute: University College Hospital
City: Ibadan (at the time of study)
Country: Nigeria
Email: iyobosa.uwadiae@physics.org

PROFESSIONAL ISSUES

MEDICAL PHYSICISTS IN THE AGE OF AI: FROM QUALITY ASSURANCE TO GOVERNANCE ASSURANCE

M.F.A. Halim [1,2], K.H. Ng [1,3]

[1] Department of Biomedical Imaging, Faculty of Medicine, Universiti Malaya, Kuala Lumpur, Malaysia
[2] Pre-market Controls Division, Medical Device Authority, Ministry of Health, Cyberjaya, Selangor, Malaysia
[3] Faculty of Medicine and Health Sciences, UCSI University, Port Dickson, Negeri Sembilan, Malaysia

Abstract – **Artificial intelligence (AI) is increasingly integrated into healthcare and is reshaping how medical technologies are developed, deployed and monitored. Unlike conventional medical devices, AI-enabled systems may evolve, creating new challenges related to validation, performance monitoring, cybersecurity and governance. Drawing upon current global evidence and emerging international guidance, this article explores how the role of medical physicists is expanding beyond traditional quality assurance towards broader governance assurance. It highlights key responsibilities in AI validation, post-market monitoring, bias assessment and governance leadership, while emphasising the importance of workforce development and international collaboration. The article argues that medical physicists are uniquely positioned to support the safe, effective and trustworthy adoption of AI-enabled medical devices and to serve as future stewards of AI governance in healthcare.**

Keywords – Artificial Intelligence; Medical Physics; AI Governance; AI-Enabled Medical Devices; Quality Assurance; Lifecycle Governance; Patient Safety; Healthcare Technology Management **.**

I. THE AI REVOLUTION HAS ALREADY ARRIVED

Figure 1. The Evolving Role of Medical Physicists in the Age of AI (AI-generated)

Artificial intelligence (AI) is rapidly transforming healthcare. Across radiology, radiation oncology and nuclear medicine, AI-enabled medical devices are increasingly being integrated into clinical workflows, supporting image reconstruction, clinical decision-making and operational efficiency [1, 2].

Unlike conventional medical technologies, many AI-enabled systems do not remain fixed after deployment. Their performance may be influenced by software updates, evolving datasets, changing patient populations and local clinical environments. As a result, ensuring that these technologies remain safe and effective over time presents new challenges for healthcare organisations [2, 3].

Medical physicists have long played a central role in the safe implementation of healthcare technology through equipment commissioning, quality assurance, performance evaluation and patient safety oversight. However, the emergence of adaptive and data-driven technologies is expanding these traditional responsibilities. Beyond ensuring that technology functions correctly, medical physicists are increasingly being called upon to support the governance, monitoring and safe integration of AI throughout its clinical lifecycle [4].

As AI becomes an increasingly important component of healthcare delivery, the profession has a unique opportunity to help shape how these technologies are implemented, monitored and governed in real-world clinical practice.

II. AI IS DIFFERENT FROM CONVENTIONAL MEDICAL DEVICES

To understand why AI governance has become such an important issue, we must first recognise how AI-enabled medical devices differ from the technologies we traditionally manage.

Consider a familiar example, such as a CT scanner. Once commissioned and placed into clinical service, its core operating characteristics generally remain stable over time. AI-enabled technologies are different. Their performance may be influenced by software updates, evolving datasets, changing patient populations and local clinical workflows. As a result, a system that performs well today may not necessarily perform identically in the future [2, 3].

This creates a new challenge for healthcare organisations. While considerable attention is given to regulatory approval and initial clinical deployment, much less attention is often paid to what happens after implementation. Yet AI systems continue to operate within dynamic clinical environments where data, workflows and practice patterns constantly evolve. Recognising this

challenge, international regulators have increasingly emphasised the importance of continuous monitoring, performance evaluation and lifecycle oversight for AI-enabled medical devices [4, 5].

As AI adoption expands, ensuring that these technologies remain safe, effective and trustworthy requires ongoing oversight rather than a one-time assessment. This highlights the growing importance of post-market monitoring, continuous performance evaluation and lifecycle governance throughout routine clinical practice [3, 6].

III. LESSONS FROM A RECENT REVIEW

A recent review of 355 studies from around the world revealed several important lessons about how AI-enabled medical devices are currently governed (unpublished). Although healthcare systems differ across countries, many of the same challenges continue to emerge.

One of the findings was that governance efforts remain heavily focused on the early stages of the technology lifecycle, particularly regulatory approval and clinical deployment. Considerable attention is devoted to how AI tools are introduced into practice, yet far less attention is directed toward what happens after implementation. Despite the adaptive nature of many AI systems, post-market surveillance and long-term performance monitoring remain relatively underdeveloped.

A second observation concerns the use of international standards. Frameworks such as ISO 14971 [7], IEC 62304 [8], and IEC 81001-5-1 [9] are widely recognised and frequently referenced. However, their practical implementation within healthcare organisations appears much less common. This highlights an important gap between regulatory expectations and everyday clinical practice.

The review also showed a significant geographical imbalance. Most governance evidence originates from high-income countries, while comparatively little is available from low- and middle-income settings. This raises important questions about local validation, infrastructure readiness, workforce capacity and governance maturity.

Perhaps the most important lesson is that governance does not end when an AI system receives regulatory approval. In many respects, governance only begins once the technology enters routine clinical practice. As AI adoption accelerates, hospitals and healthcare organisations will increasingly need local expertise to ensure these systems remain safe, effective and trustworthy over time.

IV. THE MEDICAL PHYSICIST AS THE AI SAFETY STEWARD

AI governance is often viewed as the responsibility of regulators, software developers, and healthcare administrators. However, as attention shifts toward local accountability and post-deployment oversight, it becomes clear that medical physicists already possess many of the skills needed to support the safe and effective use of AI in healthcare [4, 10].

For decades, medical physicists have been responsible for managing complex clinical technologies. We routinely assess risk, investigate incidents, validate performance and implement quality assurance programmes designed to protect patients and support clinical decision-making. Through activities such as acceptance testing, commissioning, performance evaluation and audit, we help ensure that healthcare technologies perform as intended throughout their operational life [4].

Importantly, medical physicists also work at the interface between technology and clinical practice. We regularly translate technical concepts into practical clinical applications, collaborating with clinicians, engineers, information technology teams, and hospital leadership. This ability to bridge technical and clinical domains is particularly valuable in the era of AI, where safe implementation depends not only on algorithm performance but also on how technologies interact with people, workflows and healthcare systems [4].

These existing competencies align closely with many of the challenges associated with AI-enabled medical devices. As healthcare organisations seek stronger approaches to AI validation, safety monitoring and post-market oversight, medical physicists are well-positioned to contribute to local governance efforts and support responsible implementation [4, 10].

Rather than viewing AI as a disruption to the profession, we should see it as an opportunity to extend our contribution to healthcare. The skills that have long underpinned quality and safety in medical technology can also help support the safe, effective and trustworthy use of AI in clinical practice.

V. FIVE EMERGING RESPONSIBILITIES FOR MEDICAL PHYSICISTS

As AI becomes part of routine clinical practice, many of the traditional responsibilities of medical physicists are naturally evolving. Rather than representing entirely new roles, these responsibilities build upon competencies that already exist within the profession (Table 1).

Table 1. From Quality Assurance to Governance Assurance

Traditional Responsibility	Emerging AI Responsibility
Equipment Quality Assurance	AI Performance Monitoring
Acceptance Testing	Algorithm Validation
Radiation Safety	AI Safety Assurance
Device Commissioning	Lifecycle Governance
Technical Advisor	AI Governance Advisor

One important area is AI validation. Just as new imaging equipment requires local acceptance testing and commissioning, AI systems should be evaluated within the clinical environment in which they will be used. Performance demonstrated elsewhere may not always translate directly to local patient populations, workflows, or data characteristics. International guidance increasingly emphasises the importance of validation within the intended context of use and throughout the product lifecycle [5, 6].

Medical physicists can also contribute to bias assessment by helping identify variations in algorithm performance across different patient groups. Ensuring that AI systems perform consistently and equitably is becoming an increasingly important aspect of patient safety and trustworthy AI implementation [2].

Another emerging responsibility is post-market monitoring. Unlike many conventional technologies, AI-enabled systems may change in performance over time because of evolving data, clinical practices, or software updates. Ongoing monitoring can help detect performance drift before it affects patient care. Regulatory agencies and international organisations have increasingly highlighted post-market surveillance and continuous performance monitoring as critical components of AI governance [3, 6].

As healthcare technologies become increasingly interconnected, cybersecurity awareness is also becoming part of the broader safety landscape. Medical physicists should work closely with information technology and cybersecurity teams to support the safe deployment and operation of AI-enabled systems. Cybersecurity is increasingly recognised as a key element of maintaining the safety, effectiveness and trustworthiness of software-based medical technologies [2, 11].

Finally, medical physicists can play an important role in governance leadership. As healthcare organisations assume greater responsibility for the oversight of AI-enabled technologies, many may establish multidisciplinary AI governance committees involving clinicians, information technology specialists, data scientists, administrators and medical physicists. Such committees can support local validation, performance monitoring, risk management and post-market oversight. Within these structures, medical physicists are well-positioned to contribute expertise in quality assurance, safety assurance and lifecycle management of AI-enabled medical devices [4, 10].

Together, these responsibilities reflect an important evolution of the profession, from technology assessment toward continuous stewardship of AI-enabled healthcare technologies throughout their lifecycle.

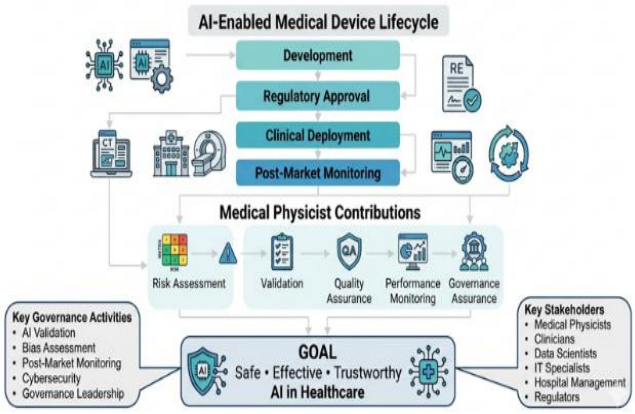

Figure 2. Medical physicists as AI safety stewards across the AI lifecycle. (AI-generated)

VI. BUILDING GLOBAL CAPACITY FOR SAFE AI ADOPTION

The IOMP encompasses healthcare systems with diverse levels of infrastructure, workforce capacity, regulatory maturity and access to technical expertise. As AI-enabled medical devices become more widely adopted, ensuring their safe and effective use will require more than technology acquisition alone. It will also require governance capability, professional competency and institutional readiness [2].

For many years, IOMP has supported professional development through its schools, workshops, scientific meetings and regional educational initiatives [12]. These established platforms provide a strong foundation for building awareness and competency in emerging areas such as AI governance, validation, safety monitoring and lifecycle management.

Beyond education, IOMP has facilitated regional collaboration and knowledge sharing among member organisations facing similar challenges. By exchanging experiences, developing practical guidance and promoting best practices, the medical physics community can help ensure that AI is implemented responsibly across a wide range of healthcare settings [4].

The challenge we are facing is not whether AI will be adopted, but whether the healthcare workforce will be adequately prepared to govern it. Through continued collaboration and professional development, IOMP can help build a community of practice that supports safe, effective and trustworthy AI adoption throughout the world.

VII. PREPARING THE NEXT GENERATION OF MEDICAL PHYSICISTS

As AI becomes increasingly embedded in healthcare, the competencies required of future medical physicists will continue to evolve. In addition to traditional expertise in clinical physics, quality assurance and patient safety, the next generation will need a broader understanding of AI literacy, data governance, cybersecurity, regulatory science, human-AI interaction and ethics [2, 4].

Developing these competencies will require ongoing education, professional development, and lifelong learning. Universities, training programmes, professional societies and healthcare organisations all have an important role to play in preparing the workforce for an increasingly digital healthcare environment [10]. Beyond technical competencies, future medical physicists will also need to cultivate ethical judgement, professional wisdom, stewardship and a strong sense of responsibility in the use of emerging technologies, particularly artificial intelligence.

Importantly, these new skills should complement and not replace the core scientific and clinical foundations of the profession. As healthcare becomes more dependent on data-driven technologies, medical physicists will be uniquely positioned to help ensure that innovation remains safe, effective and patient-centred [4].

Future medical physicists will increasingly become the trusted guardians of safe, effective and trustworthy AI across the healthcare ecosystem.

VIII. CONCLUSION

AI-enabled medical devices are reshaping healthcare, creating new challenges that extend beyond traditional regulatory approval and into routine clinical practice. Medical physicists already possess many of the skills needed to support this transition, including expertise in risk management, quality assurance, validation and clinical implementation.

As healthcare increasingly adopts AI-enabled technologies, the profession has an opportunity to expand its contribution from quality assurance to governance assurance. This action ensures that AI remains safe, effective and trustworthy throughout its lifecycle. Medical physicists can play a central role in shaping the future of healthcare.

IX. REFERENCES

1. European Society of Radiology (ESR) (2019). *Impact of artificial intelligence on radiology: a EuroAIM survey among members of the European Society of Radiology*. Insights into imaging, 10(1), 105. https://doi.org/10.1186/s13244-019-0798-3.
2. World Health Organization. (2021). *Ethics and governance of artificial intelligence for health: WHO guidance*. World Health Organization.www.who.int.
3. U.S. Food and Drug Administration. (2024). *Marketing submission recommendations for a predetermined change control plan for artificial intelligence-enabled device software functions: Guidance for industry and Food and Drug Administration staff*. U.S. Department of Health and Human Services. https://www.fda.gov/regulatory-information/search-fda-guidance-documents/marketing-submission-recommendations-predetermined-change-control-plan-artificial-intelligence
4. International Atomic Energy Agency. (2023). *Artificial intelligence in medical physics (Training Course Series No. 83)*. International Atomic Energy Agency. https://www-pub.iaea.org/MTCD/Publications/PDF/TCS83web.pdf.
5. U.S. Food and Drug Administration, Health Canada, & Medicines and Healthcare products Regulatory Agency. (2021). *Good machine learning practice for medical device development: Guiding principles*. U.S. Food and Drug Administration. https://www.fda.gov/media/153486/download
6. International Medical Device Regulators Forum. (2022). *Machine learning-enabled medical devices: Key terms and definitions* (IMDRF/AIMD WG/N67). https://www.imdrf.org/sites/default/files/2022-05/IMDRF%20AIMD%20WG%20Final%20Document%20N67.pdf.
7. International Organization for Standardization. (2019). *ISO 14971:2019 Medical devices—Application of risk management to medical devices*. ISO.
8. International Electrotechnical Commission. (2006). *IEC 62304:2006 Medical device software—Software life cycle processes*. IEC.
9. International Electrotechnical Commission. (2021). *IEC 81001-5-1:2021 – Health software and health IT systems safety, effectiveness and security — Part 5-1: Security — Activities in the product life cycle* (IEC Standard No. 81001-5-1:2021). https://www.iso.org/standard/76097.html
10. Zanca, F., Hernandez-Giron, I., Avanzo, M., Guidi, G., Crijns, W., Diaz, O., Kagadis, G. C., Rampado, O., Lønne, P. I., Ken, S., Colgan, N., Zaidi, H., Zakaria, G. A., & Kortesniemi, M. (2021). *Expanding the medical physicist curricular and professional programme to include Artificial Intelligence*. Physica Medica, 83, 174–183. https://doi.org/https://doi.org/10.1016/j.ejmp.2021.01.069
11. International Electrotechnical Commission. (2021). *IEC 81001-5-1:2021 – Health software and health IT systems safety, effectiveness and security — Part 5-1: Security — Activities in the product life cycle* (IEC Standard No. 81001-5-1:2021). https://www.iso.org/standard/76097.html
12. Rehani, M. M., Damilakis, J., Bezak, E., Duhaini, I., Tabakov, S., Ibbott, G., Pipman, Y., Renha, S. K., Chougule, A., Russo, P., & Stoeva, M. (2022). *The International Organization for Medical Physics - a driving force for the global development of medical physics*. Health and technology, 12(3), 617–631. https://doi.org/10.1007/s12553-022-00685-4

Contacts of the corresponding author:

Author: Mohd Fadhullah Bin Abd Halim
Institute: Universiti Malaya
Street: Lembah Pantai
City: Kuala Lumpur
Country: Malaysia
Email: mohdfadhullah.abdhalim@gmail.com

INVITED PAPERS

RETROSPECTIVE DVH-BASED COMPARISON OF SCHEDULED AND ADAPTED VARIAN ETHOS PLANS IN PELVIC ONLINE ADAPTIVE RADIOTHERAPY

A. Vlaykov[1], I. Iliev[1]

[1]St. Ivan Rilski Hospital, Plovdiv, Bulgaria

Abstract- **This retrospective DVH based study compared daily scheduled vs adapted Varian Ethos plans in pelvic online adaptive radiotherapy. Thirty patients contributed 359 paired fractions; the primary target analysis included 29 patients and 351 fractions with complete initial plan, scheduled plan, and adapted plan values. For them the treatment planning system reported a dose covering 90% of the planning target volume (PTV D90). Scheduled and adapted PTV D90 values were normalized to the corresponding initial plan PTV D90. Operational target benefit was defined as either recovery from less than 95% to more than or equal to 95% of the initial plan value or an improvement of more than or equal to 2.0 percentage points if the scheduled value was already more than or equal to 95%; these thresholds were relative to the initial plan PTV D90, not prescribed dose. Fraction level results were summarized only. Patient level inference results used each patient's median from the adapted plans minus the scheduled plan and a two sided Wilcoxon signed rank test by treatment site. Overall, 56.41% of the fractions meet the target benefit definition. 8.83% showed deterioration of more than 1 percentage point. Patient level median differences were +2.95 percentage points for prostate (12 patients; p=0.00049), +1.53 for bladder (5 patients; p=0.3125), and +2.00 for rectal cases (12 patients; p=0.00195). Benefit occurred in 65.88%, 47.46%, and 47.62% of fractions, respectively; deterioration occurred in 2.35%, 19.49%, and 6.35%. Secondary organ at risk analyzes were descriptive. Patient level differences were statistically significant for the prostate and rectal cohorts but not for the smaller, more heterogeneous bladder cohort. A DVH framework can be used for a retrospective audit when full DICOM image and CBCT data is unavailable.**

Keywords- **Online adaptive radiotherapy, Varian Ethos, DVH, scheduled plan, adapted plan, pelvic radiotherapy, PTV D90.**

I. INTRODUCTION

Uncertainty due to interfractional variation of a patients' internal anatomy is a persistent challenge for pelvic radiotherapy. The degree of bladder/rectal filling; position of the target; and overall patient geometry will affect both target coverage and dose to OARs when the treatment plan developed for the original planning CT scan is applied through out treatment. Image guided radiotherapy provides a means to reduce errors associated with the placement of a patient on a radiotherapy couch. Couch corrections cannot however account for the internal deformation of the OAR's and PTV from one day to another.

Cone Beam Computed Tomography (CBCT) is used in conjunction with online adaptive radiotherapy (oART) to address these issues. The CBCT is performed prior to each treatment session to assess the anatomical position of the OAR's and PTV. An optimized treatment plan is then generated based upon the CBCT obtained immediately prior to the delivery of radiation. This method of oART has been referred to as "Varian Ethos" workflow. The scheduled plan refers to the unadapted version of the reference plan delivered to the current anatomical position. The adapted plan is an optimized version of the reference plan which accounts for changes in anatomy as determined by the CBCT. Comparisons of planned parameters between scheduled and adapted plans represent decisions made by physicians, physicists, and/or radiation therapists during each treatment session [3-5].

There have been many studies demonstrating clinical benefits of oART for prostate cancer and other sites within the pelvis. Although oART may provide a substantial advantage over standard radiotherapy in terms of dose distribution, there are several challenges associated with implementing this technology into routine practice. One major concern is the time it takes to adapt a treatment plan after completion of the CBCT. Another issue is that it may not be possible or necessary to adapt all treatment plans. Additionally, even if oART appears to produce superior results during each individual treatment session, a patient-level assessment of whether such results persist across multiple fractions is needed.

Finally, obtaining complete DICOM images for reconstruction and dose accumulation is difficult. As a result, some studies rely solely on DVH data. While a DVH-based-only study can still be useful for determining the ultimate dosimetric effects of adaptations, there should be clear definitions regarding its scope and limitations.

This study compares the dosimetry of adapted versus scheduled plans for patients undergoing radiotherapy for prostate, bladder, and rectum cancers using only DVH data from the Varian Ethos system. The study incorporates patient level statistical testing along with descriptive statistics at the fraction level, and defines an objective measure of target benefit.

II. MATERIALS AND METHODS

Study Design & Data Source

A retrospective clinical dosimetrical evaluation was conducted using individualized Excel files for each patient based on plan checks completed by Mobius3D v4.0.2 for the

first planned, initially scheduled and adapted Varian Ethos plans created at MBAL Medical Complex "St. Ivan Rilski" in Plovdiv, Bulgaria. There were thirty-one individualized files that were assessed for eligibility after which the paired fraction rules were applied to evaluate the pelvic dataset consisting of 30 patients and 359 paired fractions (i.e., thirteen prostate patients [178 fractions], five bladder patients [118 fractions] and twelve rectal patients [63 fractions]).

All evaluations regarding targets and OARs utilized the values as provided by the treatment planning system and captured within the Mobius3D plan check report. No analysis was performed utilizing the values provided by Mobius3D to recalculate dose or gamma results. The available dataset also did not contain CT, CBCT or synthetic CT image series; RTPLAN, RTDOSE or RTSTRUCT objects; automatically created or edited contours; deformation registration fields or cumulative dose. Therefore, the study only analyzed the exported final DVH values without attempting independent image registration, contour verification, dose calculation or dose accumulation.

Plan States and Paired Fraction Structure

Each analytic row included information for one patient and one treatment fraction along with values for the scheduled and adapted plans compared side-by-side as a paired comparison. The initial plan remained in the same row as the patient-specific reference values. However, comparisons made against the initial plan were utilized solely for normalizing and providing context for the interpretations of the comparisons made between the scheduled plan and adapted plan.

Primary Target Analysis Subset

The primary target analysis subset required complete initial, scheduled and adapted plan values be present for PTV D90 which is defined as the treatment planning system reported dose covering ninety percent (90%) of the PTV. For this reason, one prostate patient who contributed eight paired fractions lacked sufficient PTV D90 data to compare normalized and thus was excluded from only the normalized primary target analysis. Therefore, this subset consisted of 29 patients and 351 paired fractions: 12 prostate patients / 170 fractions, 5 bladder patients / 118 fractions, and 12 rectal patients / 63 fractions (See Fig. 1).

Primary target metric and benefit definitions

The continuous results of interest for each pair of fractions, scheduled and adapted PTV D90 values were normalized to the patient-specific original plan PTV D90. The main continuous outcome was the difference in the normalized PTV D90 adapted versus scheduled, given as a percentage difference. A positive delta indicated an increased PTV D90 through adaptation.

$$Scheduled\ normalized\ PTV\ D90 = 100 \times \frac{PTV\ D90\ (scheduled)}{PTV\ D90\ (original)}$$

$$Adapted\ normalized\ PTV\ D90 = 100 \times \frac{PTV\ D90\ (adapted)}{PTV\ D90\ (original)}$$

$$Delta\ PTV\ D90 = adapted\ normalized\ PTV\ D90 - scheduled\ normalized\ PTV\ D90$$

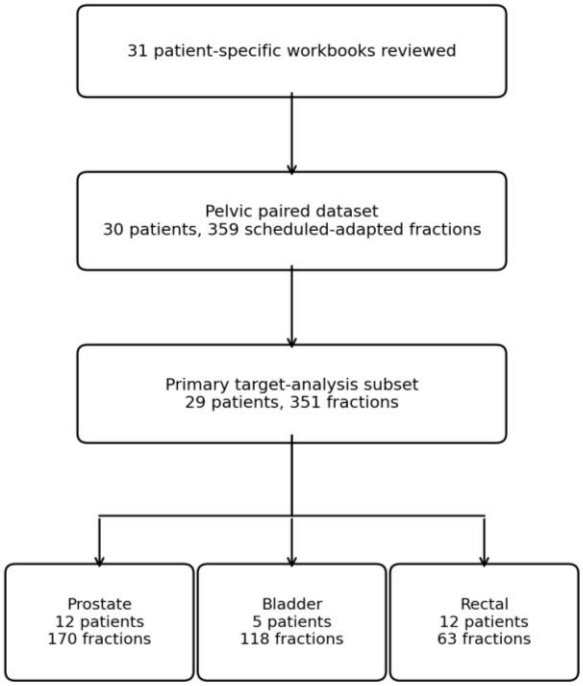

Fig. 1 Cohort derivation and primary target analysis subset.

Clinical interpretation rules

A treatment fraction was considered to have achieved its operational target benefits when one of two conditions were satisfied. The reference recovery rule consisted of the condition that both the scheduled normalized PTV D90 was less than 95% and the adapted normalized PTV D90 was greater than or equal to 95%. The additional benefit rule would apply if the scheduled normalized PTV D90 was already greater than or equal to 95%, and then the adapted plan resulted in a gain in this parameter of at least 2.0 percentage points. Target deterioration was identified when the adapted plan had a loss of more than 1.0 percentage point compared with the scheduled normalized PTV D90. This reference recovery threshold of 95% is based upon the patient-specific initial plan's PTV D90 reference; it should not be taken as being equivalent to a typical coverage metric for prescription doses, e.g., PTV D95 > or = 95% of the prescribed dose.

Secondary and treatment site specific were OAR outcomes. The maximum dose values reported by the exporting treatment planning system (TPS) were analyzed. Descriptive summaries were prepared for adapted minus scheduled differences, and dose changes of at least 0.5 Gy were noted whenever possible for the relevant metric. These findings were viewed as descriptive signals due to the fact

that the metrics utilized were maximum dose rather than small volume dose metrics. The determination of whether or not a particular treatment fraction received its operational target benefits was based solely on the primary target benefit criteria and not upon the findings related to OAR.

Statistical analysis

Daily frequencies and magnitudes of adaptive effects were analyzed at a fraction-by-fraction basis so that repeated measurements could be avoided when analyzing patients' responses. Inference regarding individual patients' responses were made using a single representative summary statistic for each patient. For each patient, the median of the adapted minus scheduled differences across all available pairs of fractions was computed, and tested separately for each of three patient groups -prostate, bladder and rectum, using a two-sided Wilcoxon signed rank test. Continuous variable results are provided as medians with inter-quartile range (IQR), while categorical outcome results are presented as counts/percentages. There were no missing values imputed into the statistical analyses, and each metric was analyzed using complete cases only. No pooled inferential test was conducted across treatment sites. Therefore, statistical significance was established at p-value < .05, and there was no need to make adjustments for multiple testing since site-specific p-values will be assessed in conjunction with their respective effect sizes, consistencies and sample sizes.

Ethics and data protection

Approval and permission to perform this independent retrospective study was granted from MBAL Medical complex "st. Ivan rilski", Plovdiv, Bulgaria. Data utilized in this study were derived directly from routine clinical practice and thus did not alter patient selection, planning nor treatment delivery. Patient identifiers were deleted prior to creating the analytical database, and only those variables required for conducting the paired-dose volume histogram (DVH) analysis were included in the analytical database.

III. RESULTS

Cohort and overall target benefit

Overall, there were 351 paired fractions for 29 patients. A total of 198 of these fractions (56.41%), across the three sites, satisfied the definition of an operational target benefit. There were a total of 88 additional benefit fractions (25.07%) and 110 reference recovery fractions (31.34%). Target potential for loss was detected on 31 fractions (8.83%) as well. In addition to being different by site, both the size and rate of the target benefit varied substantially at each of the three sites (Tables 1 and 2; Figure 2).

Table 1. Primary normalized PTV D90 results by treatment site. Fraction level values summarize paired fractions; patient level values summarize within patient median differences. Values are adapted minus scheduled; pp, percentage points.

Treatment site (patients/fractions)	Fraction level difference, pp median (IQR)	Patient level difference, pp median (IQR); p
Prostate (12/170)	3.10 (1.28 to 7.94)	2.95 (2.07 to 6.61) p=0.00049
Bladder (5/118)	1.87 (-0.51 to 3.06)	1.53 (-0.51 to 2.21) p=0.3125
Rectal (12/63)	1.48 (0.00 to 8.49)	2.00 (0.35 to 5.81) p=0.00195

Table 2. Fraction level operational target benefit and potential deterioration. Total benefit comprises reference recovery and additional benefit.

Treatment site	Recovery n (%)	Total benefit n (%)	Potential deterioration n (%)
Prostate	64 (37.65)	112 (65.88)	4 (2.35)
Bladder	27 (22.88)	56 (47.46)	23 (19.49)
Rectal	19 (30.16)	30 (47.62)	4 (6.35)
All	110 (31.34)	198 (56.41)	31 (8.83)

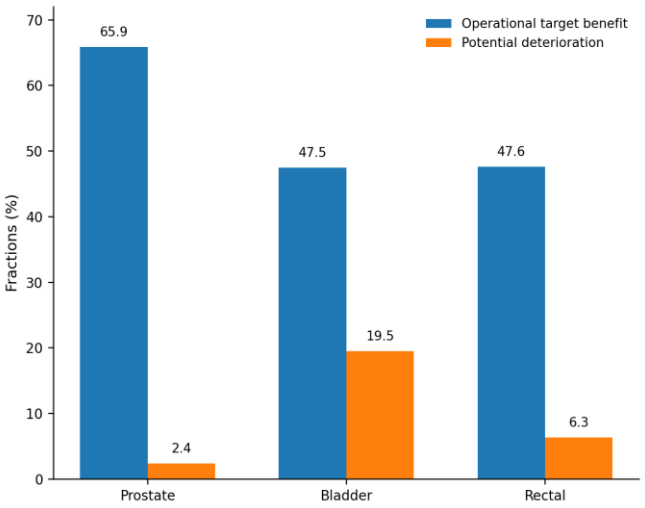

Fig. 2 Fractions meeting the target benefit definition and fractions with potential target deterioration by treatment site.

Prostate

The prostate target analysis used data from 12 patients and 170 fractions. The median normalized PTV D90 at the fraction level for the scheduled and adapted plans was 96.94% and 100.00%, respectively. The median adapted minus scheduled value is +3.10 percentage point (IQR 1.28-7.94) at the fraction level, and at the patient level it is +2.95 percentage points (IQR 2.07-6.61). All 12 patients have a positive median adapted minus scheduled value. The Wilcoxon signed-rank test shows that there is a significant advantage of the adaptive plan over the scheduled plan (p = .00049).

At the operational target levels, the prostate had benefits in 112/170 fractions (65.88%) with 64 being reference recovery fractions (37.65%) and 48 being additional benefit fractions (28.24%). There were potential target deteriorations in 4/170 fractions (2.35%).

Bladder

The bladder target analysis used data from 5 patients and 118 fractions. The median normalized PTV D90 at the fraction level for the scheduled and adapted plans was 98.21% and 99.83%, respectively. At the fraction level, the difference between the scheduled and adapted plans was +1.87 percentage points (IQR -0.51 to 3.06). At the patient level, the difference between the scheduled and adapted plans was +1.53 percentage points (IQR -0.51 to 2.21). Three patients had a positive patient-level median difference, and two had a negative median difference. The test was not statistically different at the $p < .05$ level (.3125).

At the operational target levels, the bladder had benefits in 56/118 fractions (47.46%) with 27 being reference recovery fractions (22.88%) and 29 being additional benefit fractions (24.58%). There were potential target deteriorations in 23/118 fractions (19.49%) which is the greatest number of potential target deteriorations of the three treatment sites.

Secondary analysis using exported treatment planning system maximum dose values demonstrated a median adapted - scheduled difference of -1.05 Gy (IQR -3.40 to .88) for the left femoral head/neck and -2.20 Gy (IQR -4.60 to -.73) for the right. Reductions of at least 0.5 Gy occurred in 66/118 left femoral head observations (55.93%) and 94/118 right femoral head observations (79.66%). Increases of at least 0.5 Gy occurred in 38/118 left femoral head observations (32.20%) and 11/118 right femoral head observations (9.32%), respectively. Thus, the OAR dose reduction signal was greater and more consistent on the right side.

Rectum

The rectum target analysis used data from 12 patients and 63 fractions. The median normalized PTV D90 at the fraction level for the scheduled and adapted plans was 98.52% and 100.00%. The fraction level differences between scheduled and adapted plans were +1.48 percentage points (IQR 0.00 to 8.49) and +2.00 percentage points (IQR .35 to 5.81) at the patient level. All but two of the patients had a positive median difference; those two had no median difference. The Wilcoxon signed-rank test demonstrates a significant advantage of the adaptive plan compared to the scheduled plan ($p = .00195$).

At the operational target levels, the rectum had benefits in 30/63 fractions (47.62%) with 19 being reference recovery fractions (30.16%) and 11 being additional benefit fractions (17.46%). There were potential target deteriorations in four of 63 fractions (6.35%).

Secondary analysis using exported treatment planning system maximum dose values for secondary OAR endpoints were available for eleven patients / fifty-five fractions for rectal dose demonstrating a median difference of -0.10 Gy (IQR -0.245 to .020). Six out of 55 fractions (10.91%) experienced reductions of at least 0.5 Gy, whereas zero experienced increases of at least 0.5 Gy. For ten patients / fifty fractions of bowel maximum dose values, there was a median difference of -0.285 Gy (IQR -0.960 to .065). Forty percent of these fractions had a reduction of at least 0.5 Gy, while ten percent had an increase of at least 0.5 Gy.

IV. DISCUSSION

This research shows that a large portion of the normalised PTV D90s calculated using adapted Varian Ethos plans for all patients are better than the corresponding scheduled normalised PTV D90 values, however this is very treatment site dependent. More than 50% of all treated fractions met the defined operational target benefit. The greatest benefits with the largest amount of consistency occurred with prostate cancer, with all patients experiencing a positive median difference and nearly two-thirds of fractions meeting the target benefit criteria. There was also a significant positive result for patients who received radiation treatments for rectal cancer. Patients who received radiation treatments for bladder cancer experienced a positive average trend, with nearly 50% of fractions resulting in a target benefit; however, there was substantially greater variance per-patient and a larger percentage of fractions resulted in target detriment.

These results support previous studies that have shown that the use of daily adaptations to address interfractional changes in anatomy will restore target coverage and improve plan quality for prostate patients whose original plan has been compromised by changes in anatomy [5, 7, 8] . In addition to demonstrating improved target coverage through the use of adaptations, this study provides a new perspective on how these improvements occur -- specifically that the benefits seen in this study were due to the fact that the median within-patient differences were positive in all 12 prostate patients. The bladder data require a more conservative interpretation. Bladder volumes and shapes can change greatly from fraction-to-fraction and throughout a treatment course [9, 10]; thus, the relationship between target dose and organ-at-risk (OAR) dose sparing may also vary from one fraction-to-another. Although there was not a significant difference for the entire bladder patient population, the group consisted of only five patients and exhibited considerable heterogeneity. The fraction-level data indicate that adaptations resulted in improved normalised target doses for many treatment days; however, they also clearly show that an improvement cannot always be assumed. Therefore, this supports the necessity for reviewing both target and OAR dose metrics on a fraction-by-fraction basis.

There was a significant positive patient level target advantage for patients receiving radiation treatments for rectal cancer. All patients experienced a median within-patient difference that was positive; thus, there was no patient with a negative median difference. The effects were moderate

in terms of magnitude but frequent enough that almost 50% of fractions met the target benefit definition. The secondary OAR analyses indicated a noticeable reduction in maximum bowel-loop dose; however, the reductions in maximum rectum dose were less evident. Unfortunately, these findings are only descriptive due to the limited availability of OAR dose metrics.

One strong aspect of the study methodology is its ability to separate fraction-level questions from patient-level questions. A decision regarding whether to adapt a plan is typically made at the fraction level; therefore, frequency measures are clinically interpretable. If hundreds of fractions were formally tested as if they were independent, then this would create pseudo-replication and result in overly optimistic estimates of precision.

The two-rule definition of target benefit was designed to provide practical interpretability. The reference recovery rule identifies those fractions in which adaptation restored a degraded scheduled plan value back up to the chosen initial plan reference value. The additional benefit rule prevents categorizing of small changes as "meaningful" when the scheduled normalized PTV D90 is near the reference value. Nevertheless, they could potentially serve as useful tools for quality reviews, audits and future prospective studies evaluating potential adaptation triggers [6].

Because the classification is normalized to each patient's original plan (PTV D90), it does not evaluate whether a prescribed treatment protocol meets prescription-based limits, or provides sufficient levels of target coverage for the specific protocol. In addition, because the classification applies binary rules, favorable trends are not always captured — i.e., an appreciable improvement which still falls below the 95% reference value will not be considered "recovery," nor will values near either threshold likely exhibit category shifts due to small numerical fluctuations. Therefore, quantitative comparisons between continuously adapted and scheduled should be analyzed in conjunction with the frequency data reported for the categorizations. No sensitivity analyses were performed using different thresholds than those used above.

The primary limitations of this study stem from its retrospective DVH only design. As such, this study could not examine imaging quality, contour accuracy, deformation registration, synthetic CT accuracy or accumulated delivered dose -- all known sources of uncertainty associated with CBCT guided adaptive radiotherapy (oART) requiring formal quality assurance programs [11-15]. Furthermore, while the number of patients examined was relatively large compared to other similar studies, particularly those examining bladder cancer patients, the number of bladder patients studied was modest; furthermore, treatment prescriptions and target definitions varied among sites; PTV D90 and maximum dose OAR endpoints used in this study were taken directly from structured treatment planning systems exported via Mobius3D without independent DICOM-based verification; point max dose can be sensitive to both contouring and calculation variability; and OAR endpoints were variable and site-specific. Finally, the study did not include clinical outcome data.

While these limitations exist, the dataset presented here includes 351 direct scheduled-adapted target comparisons and permitted every formal statistical conclusion to be related to individual patients instead of artificially inflated counts of fractions.

V. CONCLUSION

This retrospective DVH-based study revealed that the Ethos-plans (which had been adapted) met the operational target/criterion more frequently than the deterioration criterion. The strength and consistency of the differences in the individual case analyses were greatest and most pronounced for prostate cancer. For rectum the differences were statistically significant; however, they varied to a greater degree than those seen for prostate. Differences for bladder cases were much less consistent, and there was no statistical significance. Thus, at the level of dose fractions, an assessment could be made as to when adapted plans would have been advantageous. Conversely, at the level of the individual patient, the consistency of the advantages of using adapted plans could be assessed. While a DVH-only approach has its limitations in terms of replacing actual image data from DICOM images, CBCT, etc., and plan studies; it provides a reasonable means of evaluating/auditing the impact on the final dosimetry of using either scheduled or adapted plans.

VI. DECLARATIONS

Funding: The study received no external project or grant funding.

Conflicts of interest: The authors declare no conflict of interest.

Ethics and data protection: Institutional approval and permission to conduct the independent retrospective analysis were obtained from MBAL Medical Complex "St. Ivan Rilski", Plovdiv, Bulgaria. The study used data generated during routine clinical care and did not alter treatment. Direct patient identifiers were removed before creation of the analytical dataset and were not retained in the analysis.

Acknowledgements: The authors thank MBAL Medical Complex "St. Ivan Rilski", Plovdiv, for granting access to the dosimetric data and permission to conduct the analysis independently.

VII. REFERENCES

1. Stroom JC, Heijmen BJM. Geometrical uncertainties, radiotherapy planning margins, and the ICRU-62 report. Radiotherapy and Oncology. 2002;64(1):75-83.
2. Bujold A, Craig T, Jaffray D, Dawson LA. Image-guided radiotherapy: has it influenced patient outcomes? Seminars in Radiation Oncology. 2012;22(1):50-61.

3. Dona Lemus OM, Cao M, Cai B, Cummings M, Zheng D. Adaptive radiotherapy: next-generation radiotherapy. Cancers. 2024;16(6):1206.
4. Liu H, Schaal DW, Curry H, Clark R, Magliari A, Kupelian PA, et al. Review of cone beam computed tomography based online adaptive radiotherapy: current trend and future direction. Radiation Oncology. 2023;18(1). PMCID: PMC10475190.
5. Byrne M, Archibald-Heeren B, Hu Y, Teh A, Beserminji R, Cai E, et al. Varian Ethos online adaptive radiotherapy for prostate cancer: early results of contouring accuracy, treatment plan quality, and treatment time. Journal of Applied Clinical Medical Physics. 2022;23(1). PMCID: PMC8803282.
6. Yock AD, Ahmed M, Masick S, Morales-Paliza M, Kluwe C, Shinde A, et al. Triggering daily online adaptive radiotherapy in the pelvis: dosimetric effects and procedural implications of trigger parameter-value selection. Journal of Applied Clinical Medical Physics. 2023;24(10). PMCID: PMC10562041.
7. Eckl M, Sarria GR, Springer S, Willam M, Ruder AM, Steil V, et al. Dosimetric benefits of daily treatment plan adaptation for prostate cancer stereotactic body radiotherapy. Radiation Oncology. 2021;16(1). PMCID: PMC8335467.
8. Calvo-Ortega JF, Laosa-Bello C, Moragues-Femenia S, Torices-Caballero J, Pozo-Masso M, Jones A, et al. Online adaptive five-fraction ablative radiotherapy for prostate cancer using a conventional linear accelerator. Practical Radiation Oncology. 2025;15(4):e371-e381.
9. Azzarouali S, Goudschaal K, Visser J, Hulshof M, Admiraal M, van Wieringen N, et al. Online adaptive radiotherapy for bladder cancer using a simultaneous integrated boost and fiducial markers. Radiation Oncology. 2023;18(1). PMCID: PMC10557331.
10. Fischer J, Fischer LA, Bensberg J, Bojko N, Bouabdallaoui M, Frohn J, et al. CBCT-based online adaptive radiotherapy of the bladder: geometrical and dosimetrical considerations compared with conventional IGRT. Radiation Oncology. 2025;20(1). doi:10.1186/s13014-025-02710-y.
11. Zhao X, Stanley DN, Cardenas CE, Harms J, Popple RA. Do we need patient-specific QA for adaptively generated plans? Retrospective evaluation of delivered online adaptive treatment plans on Varian Ethos. Journal of Applied Clinical Medical Physics. 2023;24(2):e13876.
12. Zheng D, Cummings M, Zhang H, Podgorsak A, Li F, Dona Lemus OM, et al. Clinical practice-based failure modes and root cause analysis of cone beam CT-guided online adaptive radiotherapy of the pelvis. Cancers. 2025;17(9):1462.
13. Yoganathan SA, Khemissi A, Paloor S, Hammoud R, Al-Hammadi N. An end-to-end quality assurance procedure for Ethos online adaptive radiotherapy. Journal of Medical Physics. 2025;50(1):140-147.
14. Lavrova E, Garrett MD, Wang Y, Chin C, Elliston CD, Savacool M, et al. Adaptive radiation therapy: a review of CT-based techniques. Radiology: Imaging Cancer. 2023;5(4). PMCID: PMC10413297.
15. Byrne M, Ray X, Kisling K, Archibald-Heeren B, Finnegan R, Luo S, et al. Pelvic dose accumulation accuracy in a CBCT-based online adaptive radiotherapy system. Journal of Applied Clinical Medical Physics. 2025;26(7):e70160.

Contacts of the corresponding author:

Authors: Anton Vlaykov
Institute: St. Ivan Rilski Hospital
City: Plovdiv
Country: Bulgaria
Email: antonvlaykov@gmail.com

MULTI-PARAMETRIC ANALYSIS OF BREAST COMPRESSION IN FULL-FIELD DIGITAL MAMMOGRAPHY: DOSIMETRIC MODELING AND MACHINE LEARNING-BASED PAIN TOLERANCE CLASSIFICATION

R. Pirchio[1,2]

[1] Comisión Nacional de Energía Atómica, Av Pro. González y Aragón 15, B1802AYA, Ezeiza, Buenos Aires, Argentina
[2] Universidad Tecnológica Nacional, Facultad Regional Buenos Aires, Medrano 951 (C1179AAQ) CABA, Buenos Aires, Argentina

Abstract – **To develop and evaluate multiparametric models relating breast compression, mean glandular dose (MGD), and patient-reported pain tolerance in full-field digital mammography (FFDM) using multivariable regression and machine-learning techniques. A retrospective dataset comprising 208 women examined with a Fujifilm Amulet Innovality FFDM system operating under automatic exposure control was analyzed. Demographic, anatomical, mechanical, acquisition and dosimetric variables were included. To improve model training, a balanced synthetic dataset (n = 468) was generated. MGD was modeled using Linear Regression, third-order Polynomial Regression, and Gaussian Process Regression (GPR) with a Matérn 5/2 kernel. Correlation analysis and Principal Component Analysis (PCA) were performed to characterize variable relationships and reduce dimensionality. Pain tolerance was classified into three categories using supervised machine-learning algorithms evaluated by five-fold cross-validation and independent external validation. MGD showed its strongest association with tube current–time product (mAs) (r = 0.96), followed by tube voltage (r = 0.53) and compressed breast thickness (r = 0.52), whereas compression force exhibited only a weak correlation (r = 0.14). The multivariable GPR model achieved the highest predictive performance (R^2 = 0.687; RMSE = 0.410 mGy) and demonstrated agreement during external validation (R^2 = 0.950; RMSE = 0.168 mGy). For pain-tolerance classification, Fine KNN showed the highest cross-validation accuracy (86.5%), whereas Ensemble Bagged Trees demonstrated the most consistent performance across internal and external validation. MGD is determined by the combined effects of breast anatomy, mechanical characteristics, and acquisition parameters rather than by any single variable. GPR enabled accurate patient-specific dose estimation, while Ensemble Bagged Trees provided the most robust prediction of pain tolerance. These findings support the development of personalized mammographic protocols that jointly optimize radiation dose, image quality, and patient comfort.**

Keywords- **Full-field digital mammography; Mean glandular dose; Breast compression; Gaussian Process Regression; Machine learning; Pain tolerance.**

I. INTRODUCTION

Breast cancer remains one of the most frequently diagnosed malignancies worldwide, and mammographic screening plays a central role in early detection and mortality reduction [1,2]. Full-field digital mammography (FFDM) is widely used in both screening and diagnostic, where optimization of image quality and radiation exposure remains a fundamental objective [3].

Breast compression is an essential component of FFDM because it reduces tissue overlap, improves image quality, minimizes motion artifacts, and optimizes radiation dose by decreasing breast thickness and improving exposure efficiency [3,4]. However, it is also the main source of patient discomfort and may negatively affect the patient experience and participation in breast cancer screening programs [5,6].

Mean glandular dose (MGD), the standard dosimetric quantity for mammography, is influenced by multiple factors, including breast thickness, tissue composition, compression parameters, tube voltage (kVp), and tube current–time product (mAs) [4]. Similarly, pain perception during mammographic compression is a multifactorial process influenced by anatomical, mechanical, and patient-related variables, although the combined contribution of these factors remains incompletely understood [5,6].

The interaction among breast anatomy, compression, acquisition parameters, and patient response is difficult to characterize using conventional statistical approaches. Machine-learning techniques provide an effective framework for modeling complex nonlinear relationships and identifying interactions that may not be captured by traditional methods [7].

This study aimed to perform a multiparametric analysis of breast compression in FFDM by investigating relationships among anatomical, mechanical, and acquisition variables using correlation analysis and Principal Component Analysis (PCA); developing multivariable regression models for MGD estimation; and evaluating supervised machine-learning algorithms for predicting patient-reported pain tolerance.

II. MATERIALS AND METHODS

Study Dataset

A retrospective dataset comprising 208 women who underwent FFDM examinations using a Fujifilm Amulet Innovality system operating under automatic exposure control (AEC) was analyzed. Recorded variables included age, compressed and uncompressed breast thickness, compression force, compression percentage, kVp, mAs, breast type, chest wall-to-nipple distance, and MGD.

Patient-reported pain tolerance was categorized into three levels (low, moderate, and high), and breast type was encoded into three tissue-composition classes.

Data Preprocessing

Class imbalance was addressed using a customized Synthetic Minority Oversampling Technique (SMOTE) applied exclusively to the training data within each five-fold cross-validation split. Synthetic samples were generated using k-nearest-neighbor interpolation with controlled Gaussian perturbations while preserving clinically plausible ranges and physically consistent relationships among variables. Test sets remained unchanged to prevent information leakage.

Pain-Tolerance Classification

Supervised machine-learning algorithms were initially performed using the MATLAB Classification Learner toolbox. Based on five-fold cross-validation performance, the three best-performing classifiers: Fine KNN, Ensemble Bagged Trees, and KNN with PCA, were selected for detailed evaluation.

Performance was assessed using five-fold cross-validation (80% training and 20% testing). Feature normalization parameters were estimated from the training data and applied to the corresponding test set. SMOTE was applied only to the training subset of each fold. Classification performance was evaluated using accuracy, precision, recall, F1-score, and confusion matrices.

Correlation Analysis and Principal Component Analysis

Pearson correlation coefficients were calculated to evaluate relationships among anatomical, mechanical, acquisition, and dosimetric variables.

PCA was performed after z-score standardization to characterize the multivariate structure of the dataset, evaluate variable contributions, and generate PCA-derived predictors. The first five principal components were retained for regression modeling.

Dosimetric Regression Modeling

Three predictor configurations were evaluated:

- Dance Model: compressed breast thickness, mAs, kVp, and breast type.
- Full Model: age, compressed and uncompressed breast thickness, compression force, mAs, kVp, chest wall-to-nipple distance, and breast type.
- PCA Model: the first five principal components derived from the Full Model predictors.

Each predictor configuration was evaluated using Linear Regression (LR), third-order Polynomial Regression (Poly3), and GPR with a Matérn 5/2 kernel. Predictive performance was assessed using five-fold cross-validation with R^2 and RMSE.

External Validation

Model generalization was evaluated using an independent dataset of 30 FFDM examinations acquired with the same mammography system. Following model selection, the optimal regression models were retrained using the complete development dataset and applied to the external cohort. Performance was quantified using R^2, RMSE and measured-versus-predicted MGD comparisons.

III. RESULTS

Correlation Analysis

Pearson correlation analysis identified mAs as the variable most strongly associated with MGD (r = 0.96), followed by kVp (r = 0.53), compressed breast thickness (r = 0.52), and uncompressed breast thickness (r = 0.45) (Figure 1). In contrast, compression force showed only a weak correlation with MGD (r = 0.14).

Compressed breast thickness was strongly correlated with kVp (r = 0.93), mAs (r = 0.56), and uncompressed breast thickness (r = 0.85), reflecting the expected behavior of the AEC system.

Overall, MGD was primarily influenced by breast geometry and acquisition parameters, whereas demographic and mechanical variables had limited effects.

Principal Component Analysis

The first three principal components (PC1–PC3) explained 76.2% of the total variance, while the first five components accounted for 92.6%, indicating that most dataset variability was preserved in a reduced-dimensional space. PC1 was primarily associated with breast thickness and acquisition parameters, PC2 with anatomical and mechanical variables, and PC3 with breast tissue composition (Figure 2).

PCA Projection

The three-dimensional PCA projection (Figure 3) showed substantial overlap among pain-tolerance categories, with no distinct class separation despite the high proportion of explained variance. These findings indicate that linear combinations of the original variables were insufficient to discriminate pain-tolerance levels, supporting the use of nonlinear machine-learning methods.

Dosimetric Regression Modeling

Three dosimetric predictor configurations were evaluated using five-fold cross-validation (Table 1): the Dance Model (compressed breast thickness, mAs, kVp, and breast type), the Full Model (eight anatomical and acquisition variables), and the PCA Model (the first five principal components).

The Full Model achieved the highest predictive accuracy, with GPR achieving the best performance (R^2 = 0.687; RMSE = 0.410 mGy). The Dance Model performed similarly (R^2 = 0.681; RMSE = 0.414 mGy), whereas the PCA Model showed lower accuracy, suggesting that dimensionality reduction removed information relevant for dose estimation.

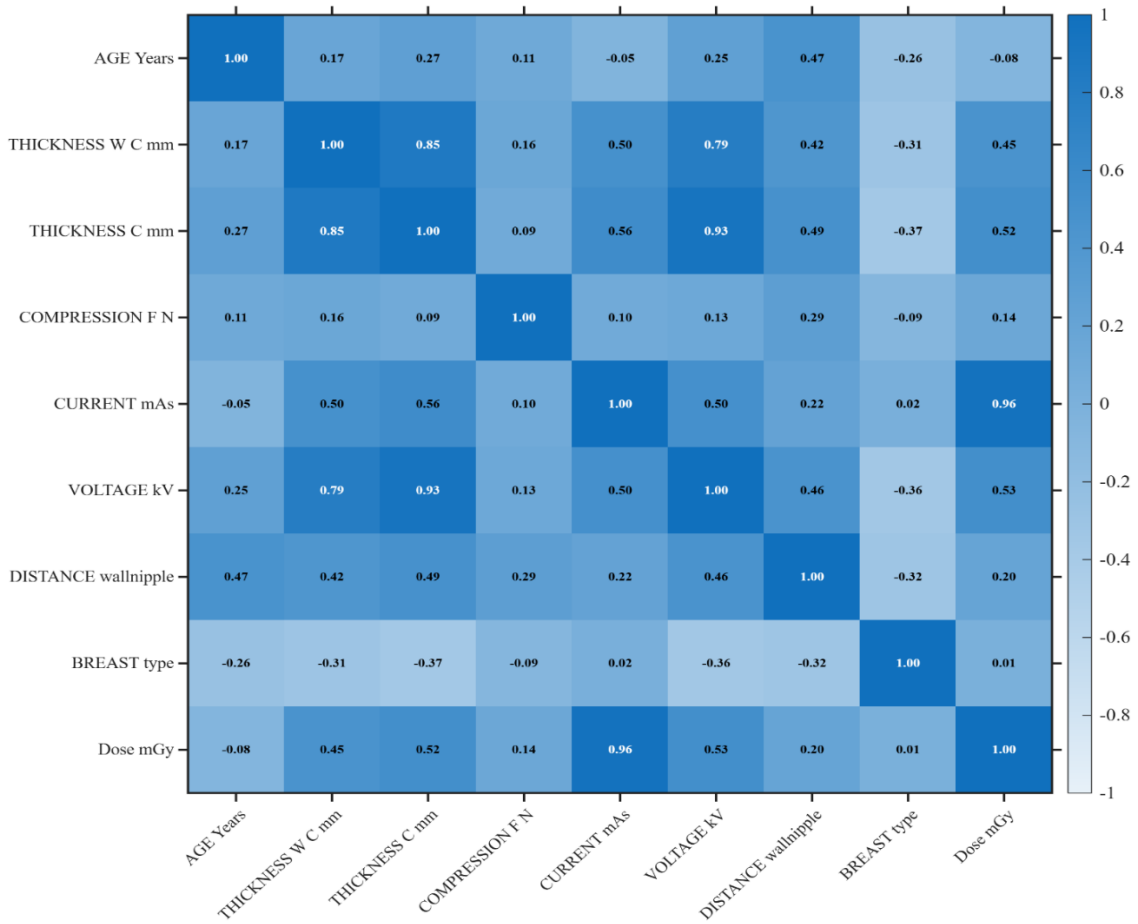

Figure 1. Pearson correlation matrix showing relationships among demographic, anatomical, mechanical, acquisition, and dosimetric variables

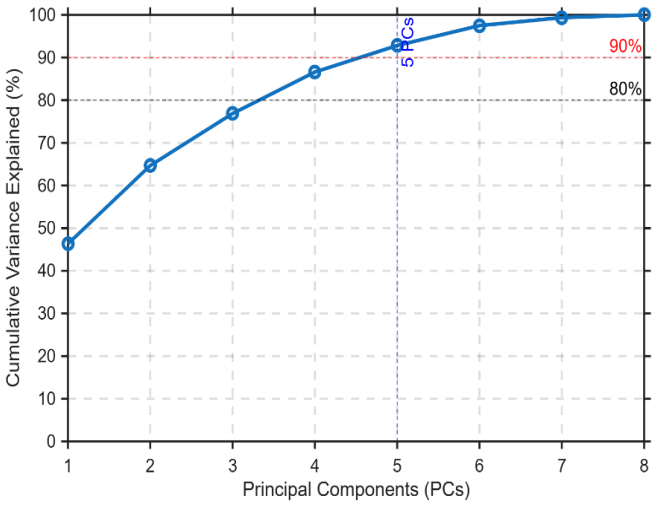

Figure 2. Variable loadings of the first five principal components

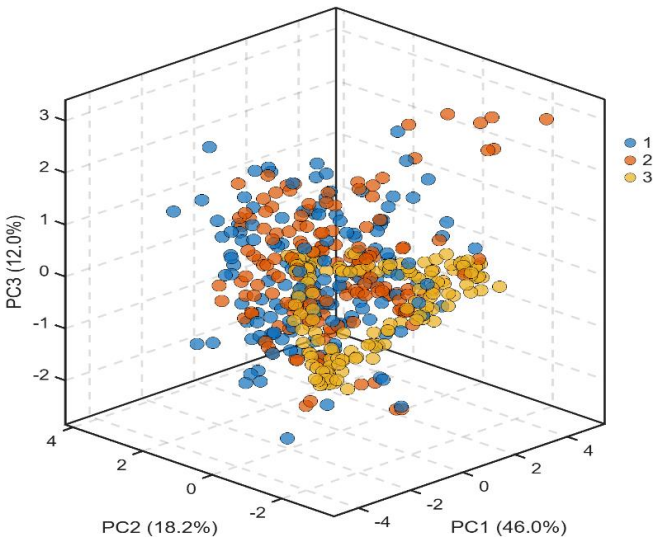

Figure 3. Three-dimensional PCA projection of the study dataset using the first three principal components

Table 1. Predictive performance of the Dance, Full, and PCA dosimetric models evaluated using five-fold cross-validation

Predictor configuration	Regression method	R^2	RMSE (mGy)
Dance Model	Gaussian Process Regression (Matérn 5/2)	0.681	0.414
Dance Model	Linear Regression	0.680	0.414
Dance Model	Third-Order Polynomial Regression	0.665	0.424
Full Model	Gaussian Process Regression (Matérn 5/2)	0.687	0.410
Full Model	Linear Regression	0.675	0.420
Full Model	Third-Order Polynomial Regression	0.670	0.414
PCA Model	Gaussian Process Regression (Matérn 5/2)	0.617	0.453
PCA Model	Linear Regression	0.601	0.463
PCA Model	Third-Order Polynomial Regression	0.603	0.461

External Validation

The selected GPR models were evaluated using an independent dataset of 30 FFDM examinations acquired with the same mammography system. As shown in Figure 4, the Dance and Full models achieved similar predictive performance (R^2 = 0.957 and 0.951; RMSE = 0.155 and 0.166 mGy, respectively), both outperforming the PCA Model (R^2 = 0.890; RMSE = 0.248 mGy). Predicted and measured MGD values showed close agreement across the external dataset, confirming the robustness of the proposed regression models.

Feature Importance Analysis

Automatic Relevance Determination (ARD) within the GPR framework was used to estimate the relative contribution of predictors included in the Full Model. The mAs was the most influential predictor (42.1%), followed by compressed breast thickness. Compression force, kVp, chest wall-to-nipple distance, and breast type showed smaller contributions, whereas age and uncompressed breast thickness had minimal influence. These findings are consistent with the correlation and PCA analyses, highlighting the dominant role of acquisition parameters and breast geometry in dose estimation.

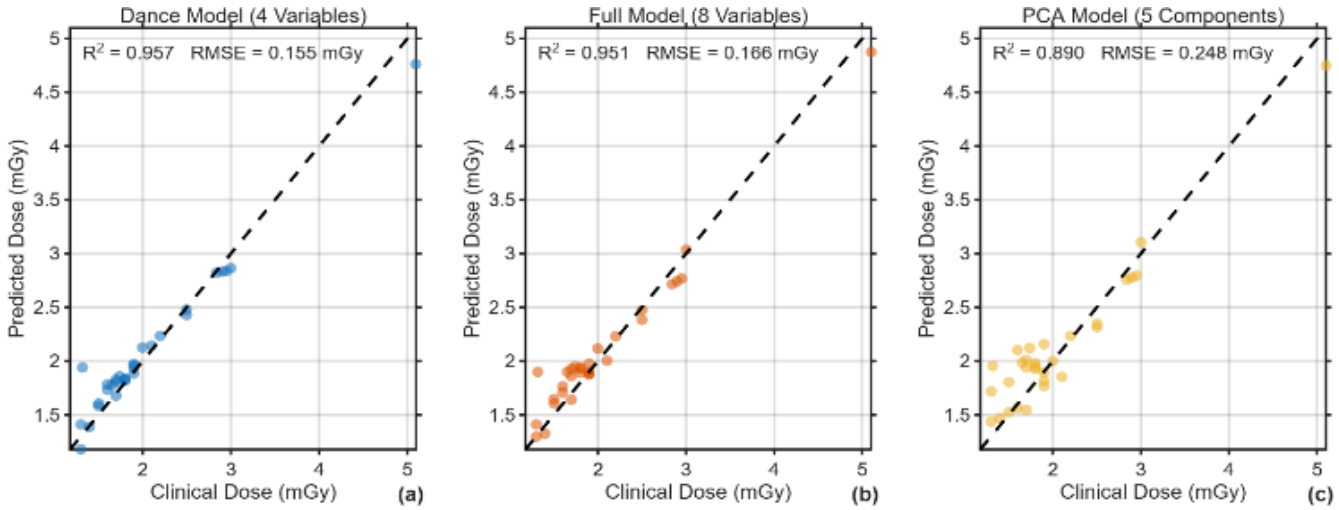

Figure 4. Predicted versus measured mean glandular dose (MGD) for the independent external validation dataset using the Dance, Full, and PCA Gaussian Process Regression (GPR) models. The dashed line represents the line of identity

Pain-Tolerance Classification

Classification results are summarized in Table 2. During five-fold cross-validation, Fine KNN achieved the highest overall accuracy (87.4%), followed by Ensemble Bagged Trees (82.3%) and KNN + PCA (79.3%). During external validation, however, Fine KNN showed poor generalization (26.7%), whereas Ensemble Bagged Trees and KNN + PCA achieved accuracies of 93.3% and 96.7%, respectively.

Although KNN + PCA achieved the highest external accuracy, Ensemble Bagged Trees classifier provided the most balanced performance across pain-tolerance categories and the most consistent behavior between cross-validation and external validation (Figure 5). Overall, pain perception was influenced by multiple interacting anatomical and acquisition variables and could be effectively modeled using machine-learning methods.

Predictor Sensitivity Analysis

A leave-one-variable-out sensitivity analysis using the Ensemble Bagged Trees classifier to evaluate the contribution of individual predictors to pain-tolerance classification. Removal of age produced the largest reduction in accuracy, decreasing performance from 84.1% to 77.2%. Chest wall-to-nipple distance was the second most influential

predictor, with accuracy decreasing to 81.0% when excluded. In contrast, removing the remaining variables, including breast thickness parameters, compression force, tube current–time product, tube voltage, and breast type, produced minimal changes in classification performance (≤1 percentage point).

These results suggest that pain perception during mammographic compression is not determined by a single acquisition parameter but rather by the combined contribution of multiple anatomical, mechanical, and patient-related factors.

IV. DISCUSSION

The present study investigated the relationships among breast compression, MGD, and patient-reported pain tolerance in full-field digital mammography using multivariable regression and machine-learning approaches. The findings demonstrate that both radiation dose and pain perception depend on the interaction of anatomical, mechanical, and acquisition-related variables rather than on any single predictor.

Table 2. Classification performance of the evaluated classifiers during five-fold cross-validation (CV) and independent external validation (Ext). Precision, recall, and F1-score are reported for each pain-tolerance category.

Classifier	Evaluation	Pain tolerance	Precision (%)	Recall (%)	F1-score
Ensemble Bagged Trees	CV (Accuracy 82.3%)	Class 1	75.5	77.6	76.5
		Class 2	78.9	71.2	74.9
		Class 3	92.5	98.1	95.2
Fine KNN	CV (Accuracy 87.4%)	Class 1	86.8	75.6	80.8
		Class 2	80.9	88.5	84.5
		Class 3	94.7	98.1	96.4
KNN + PCA	CV (Accuracy 79.3%)	Class 1	77.8	62.8	69.5
		Class 2	71.0	76.3	73.5
		Class 3	92.4	98.7	95.4
Ensemble Bagged Trees	Ext (Accuracy 93.3%)	Class 1	90.0	90.0	90.0
		Class 2	100.0	90.0	94.7
		Class 3	100.0	100.0	100.0
Fine KNN	Ext (Accuracy 26.7%)	Class 1	25.0	10.0	14.3
		Class 2	31.8	70.0	43.8
		Class 3	0.0	0.0	0.0
KNN + PCA	Ext (Accuracy 96.7%)	Class 1	90.0	90.0	90.0
		Class 2	100.0	100.0	100.0
		Class 3	100.0	100.0	100.0

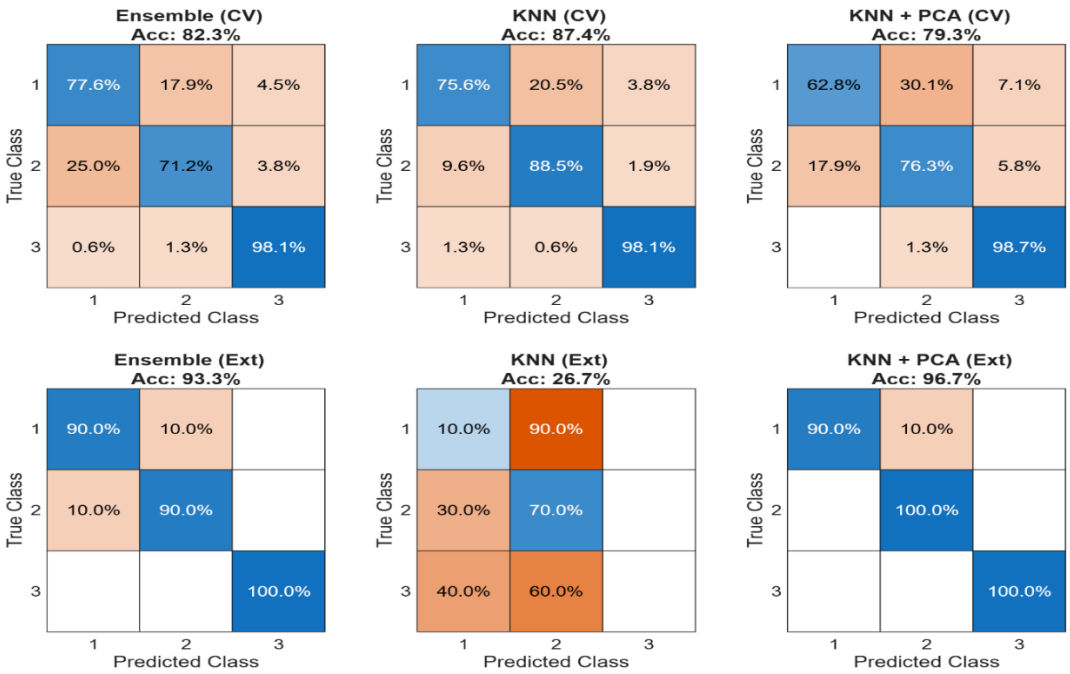

Figure 5. Confusion matrices for the Ensemble Bagged Trees, Fine KNN, and KNN + PCA classifiers obtained during five-fold cross-validation (upper row) and independent external validation (lower row)

Dosimetric Modeling

Among the evaluated regression approaches, GPR provided the best predictive performance, particularly when combined with the Full Model predictor configuration. However, the Dance Model achieved comparable accuracy, indicating that a reduced number of clinically relevant variables may be sufficient for reliable MGD estimation.

Feature importance analysis identified mAs and compressed breast thickness as the dominant predictors, consistent with the correlation and PCA findings. This observation agrees with previous reports indicating that

breast thickness and exposure parameters are major determinants of mammographic dose [4]. External validation demonstrated close agreement between predicted and measured MGD values, supporting the applicability of the proposed regression framework under consistent acquisition conditions.

Principal Component Analysis

PCA showed that most dataset variability could be represented by a reduced number of components, mainly associated with breast geometry, acquisition parameters, and tissue composition. However, the persistent overlap among pain-tolerance categories indicated that linear combinations of variables were insufficient for class separation, supporting the use of nonlinear machine-learning approaches.

Pain-Tolerance Classification

Machine-learning classifiers predicted pain tolerance with good overall performance. Although Fine KNN achieved the highest cross-validation accuracy, its marked decrease during external validation indicated limited generalization. In contrast, Ensemble Bagged Trees showed the most consistent performance across internal and external evaluations.

Sensitivity analysis identified age and chest wall-to-nipple distance as the most influential predictors, whereas removing individual acquisition parameters produced only minor changes in performance. These findings support the multifactorial nature of pain perception and agree with previous studies showing that mammographic discomfort is influenced by multiple anatomical and mechanical factors rather than compression force alone [5,6,10-12]

Clinical Implications

Optimization of mammographic examinations should consider not only radiation dose and image quality but also patient comfort [4,5]. The proposed dosimetric models enable MGD estimation from routinely available variables, while supervised classification may assist in predicting patient tolerance to compression. Machine-learning approaches have increasingly been applied in medicine to model complex interactions and support personalized decision-making [7]. Together, these approaches may facilitate personalized mammographic protocols that optimize radiation exposure, diagnostic performance, and patient experience.

Limitations

This study has several limitations. Data was obtained from a single institution using one mammography system, which may limit generalizability. External validation was performed on a relatively small independent cohort acquired under the same clinical conditions, and larger multicenter studies are required to confirm model generalization.

Although SMOTE improved class balance during training, synthetic samples may influence the performance of distance-based classifiers. In addition, pain perception is inherently subjective and may be affected by psychological, emotional, and contextual factors not included in the present dataset.

V. CONCLUSION

This study demonstrated that mean glandular dose is primarily determined by the combined effects of breast geometry and acquisition parameters, whereas pain tolerance arises from complex interactions among anatomical, demographic, and imaging-related factors.

Among the evaluated regression approaches, Gaussian Process Regression with the Full Model provided the most accurate MGD estimation. For pain-tolerance classification, Ensemble Bagged Trees showed the most consistent performance across internal and external validation, despite the higher cross-validation accuracy of Fine KNN.

Although PCA effectively summarized dataset variability, its use as a predictive input reduced model performance, suggesting that dimensionality reduction removed information relevant for dose estimation.

Overall, these findings support the integration of regression modeling and machine-learning techniques to develop personalized mammographic protocols that optimize radiation dose, image quality, and patient comfort.

VI. REFERENCES

1. Sung, H., Ferlay, J., Siegel, R. L., Laversanne, M., Soerjomataram, I., Jemal, A., & Bray, F. (2021). Global cancer statistics 2020: GLOBOCAN estimates. *CA: A Cancer Journal for Clinicians, 71*(3), 209–249. https://doi.org/10.3322/caac.21660.
2. Tabár, L., Vitak, B., Chen, H. H., Duffy, S. W., & Yen, A. M. F. (2011). Swedish two-county trial: Impact of mammographic screening. *Radiology, 260*(3), 658–663.
3. Sechopoulos, I. (2013). A review of breast tomosynthesis. *Radiology, 267*(1), 22–35. https://doi.org/10.1148/radiol.12120518.
4. Dance, D. R., Young, K. C., van Engen, R. E., & Thilander-Klang, A. (2011). Breast dosimetry in digital mammography. *Physics in Medicine & Biology, 56*(3), R1–R25.
5. Whelehan, P., Evans, A., & Wells, M. (2013). Pain and discomfort in mammography. *European Journal of Cancer Care, 22*(4), 582–590.
6. Kornguth, P. J., et al. (1993). Factors influencing pain during mammography. *Radiology, 186*(1), 81–85.
7. Deo, R. C. (2015). Machine learning in medicine. *Circulation, 132*(20), 1920–1930.
8. Chawla, N. V., Bowyer, K. W., Hall, L. O., & Kegelmeyer, W. P. (2002). *SMOTE: Synthetic Minority Over-sampling Technique*. Journal of Artificial Intelligence Research, 16, 321–357. https://doi.org/10.1613/jair.953.
9. Rasmussen, C. E., & Williams, C. K. I. (2006). *Gaussian Processes for Machine Learning*. Cambridge, MA: MIT Press.
10. Miller, D., et al. (2008). Compression force and patient discomfort in mammography. *AJR American Journal of Roentgenology, 191*(3), 744–750.

11. Lundgren, M., et al. (2004). Predictors of pain in mammography. *Acta Radiologica, 45*(7), 764–771.
12. Blanco, S., Di Risio, C., Andisco, D., Rojas, R. R., & Rojas, R. M. (2017). Parámetros mamográficos: compresión, dosis y disconfort. *Revista Argentina de Radiología, 81*(2). https://doi.org/10.1016/j.rard.2017.04.006.

Contacts of the corresponding author:

Authors: Rosana Pirchio
Institute: Comisión Nacional de Energía Atómica
City: Buenos Aires
Country: Argentina
Email: rosana.roqui69@gmail.com

OBJECTIVE VS SUBJECTIVE MEASURE OF THE LOW CONTRAST PENETRATION TEST IN ULTRASOUND IMAGING

D. R. Hewer [1], M. L. Camilleri [1], M. Busuttil [1], K. Vella [1], A. Pule [1], K. A. Micallef [1]

[1] Department of Medical Physics, Faculty of Health Sciences, University of Malta, Malta

Abstract – **This study compares subjective and objective approaches for measuring low contrast penetration (LCP) in ultrasound (US) quality assurance (QA). Thirty repeated phantom tests were conducted using two linear, and one curvilinear probe. An objective single phantom image (SPI) method determined the depth of penetration from signal-to-noise ratio (SNR) curves using a polynomial fit and defined thresholds. SPI measurements showed markedly lower variability (standard deviation (SD) < 2 mm) compared to manual measurements (SD up to 9 mm). Agreement between methods was strongest for the curvilinear probe. The findings support integrating objective LCP analysis into routine US QA programmes.**

Keywords – **ultrasound, low contrast penetration, automated methods, quality assurance.**

I. INTRODUCTION

Low contrast penetration (LCP) testing evaluates an ultrasound (US) system's sensitivity by measuring the depth at which speckle signals are distinguishable from the background scattering material in a phantom [1]. It is a critical parameter for identifying gradual performance degradation over time, often preceding visible artefacts or system failure [2,3]. According to professional standards such as IPEM Report 102 [4] and AAPM Report No. 1 [5], LCP assessment is typically assessed visually by measuring the depth at which the last discernible structure is observed. However, this subjective approach introduces inter- and intra-observer variability, dependent on experience, visual acuity, and ambient conditions such as display brightness or room lighting.

To mitigate this subjectivity, objective computational methods have been proposed, with Gorny et al. (2005) [6] introducing the single phantom image (SPI) approach for deriving depth of penetration (DOP) from quantitative image analysis. The SPI method computes signal-to-noise ratio (SNR) profiles across depth and defines the penetration limit as the depth at which the SNR falls below a predefined threshold. Despite its promise, few studies have compared SPI-derived DOP values against manual measurements in routine quality assurance (QA) settings.

This study aims to evaluate the consistency and reliability of the SPI method against traditional visual estimation for different US probe types, thus determining its suitability as a standardised, observer-independent measure of LCP.

II. MATERIALS AND METHODS

Data Acquisition

US uniformity images were acquired from thirty repeated US phantom scans performed using the same single diagnostic system at the Medical Imaging Department of Mater Dei Hospital, Malta. Three probes were assessed: i18LX5, i24LX8 (linear), and i8CX1 (curvilinear). Each scan maintained consistent imaging parameters, including depth, focus, and gain settings, while minor variations in time-gain compensation (TGC) were recorded. For the curvilinear probe, the maximum analysis depth was limited to 170 mm to exclude reverberation artefacts from the phantom base.

Manual Method

Five medical physicists (MPs) (MP1–MP5) independently reviewed stored images and recorded the DOP at which the final visible structure could be identified. Observer experience varied from <1 year to >8 years, providing a broad representation of practical variability.

Objective Method

The SPI analysis was implemented in Python. For each test, the SNR was computed as the ratio of mean pixel value (MPV) within the phantom to the background noise from an in-air region, using a vertical line profile across image depth (Eq 1) [6]. The tail region of the SNR curve, beginning after the maximum signal, was fitted using a second-degree polynomial. The DOP was then determined as the depth where the fitted curve intersected the SNR threshold (4.5 for linear, 1.4 for curvilinear probes), as described by Gorny et al. (2005) [6]. Figure 1 shows an example of the curve-fitting process, for the i18LX5 probe. Equation 1 shows the calculation for the SPI method.

$$SNR(d) = \mu_1(d) \div \mu_a(d) \quad (1)$$

where $\mu_1(d)$ is the MPV for the phantom image, and $\mu_a(d)$ is the MPV of the in-air image, both at depth d.

Statistical Analysis

Descriptive statistics were computed for both manual and SPI-derived DOPs. Standard deviation (SD) was used as a measure of repeatability. Inter-observer variability was evaluated, and comparisons between objective and subjective methods were analysed across probe types.

Software-related uncertainty arising from ImageJ-based measurements was estimated at ±0.001 mm.

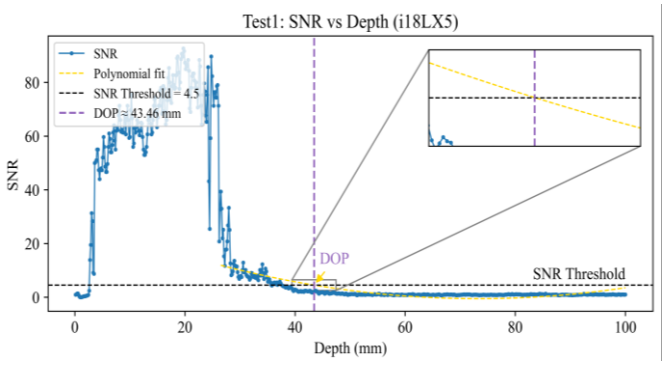

Fig. 1 Graph of SNR vs Depth for i18LX5 probe (test 1)

III. RESULTS

The SPI method demonstrated markedly lower variability across all probe types, with SD below 2 mm compared to manual values that reached SD of 6-9 mm, especially among less experienced observers. For the linear probes (i18LX5, i24LX8), SPI-derived DOPs were consistently lower (~30-50 mm) than manual readings (~60-70 mm), reflecting the stricter SNR threshold criterion. In contrast, for the curvilinear probe (i8CX1), agreement between manual and SPI DOPs was stronger (130-165 mm), aligning with expectations for lower-frequency transducers that exhibit slower signal attenuation. Less experienced MPs (MP5) yielded inconsistent readings, further illustrating the subjectivity of visual interpretation. Table 1 shows the automated and manual DOP measurements, performed by each MP, for the i8CX1 probe.

Table 1: i8CX1 curvilinear probe automated and manual DOP (mm) measurements

Test no.	SPI	MP1	MP2	MP3	MP4	MP5
1	138.06	157.35	150.11	147.91	157.62	144.00
2	141.83	156.40	162.88	145.13	152.04	150.35
⋮	⋮	⋮	⋮	⋮	⋮	⋮
30	144.05	162.58	154.27	141.65	155.29	142.44
Mean	145.89	158.20	157.46	143.36	154.36	146.66
SD	3.75	2.99	3.80	2.39	2.96	12.54

Figure 2 shows a plot of both manual and automated DOP measurements for each test, for the i8CX1 probe.

Similarly, tables 2 and 3 show the automated and manual DOP measurements, for the linear i18LX5 and i24LX8 probes respectively, while figures 3 and 4 display plots of both manual and automated DOP measurements for each test, for the i18LX5 and i24LX8 probes respectively.

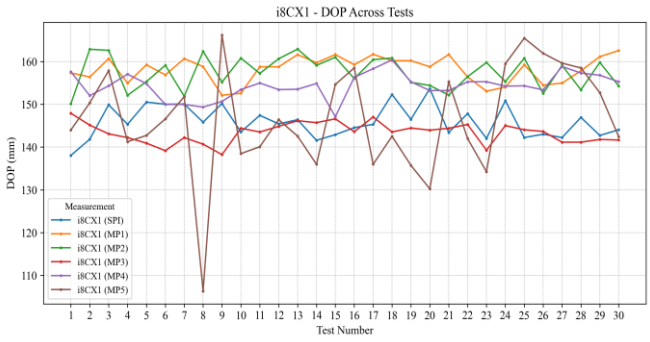

Fig. 2 DOP measurements for each test for the i8CX1 probe

Table 2: i18LX5 linear probe automated and manual DOP (mm) measurements

Test no.	SPI	MP1	MP2	MP3	MP4	MP5
1	43.46	53.48	49.13	64.02	52.41	52.26
2	46.45	52.80	59.56	67.79	58.85	64.22
⋮	⋮	⋮	⋮	⋮	⋮	⋮
30	46.56	51.44	51.51	64.08	52.32	63.74
Mean	46.45	56.99	54.55	66.93	54.73	64.09
SD	1.88	2.67	3.10	1.13	2.61	7.73

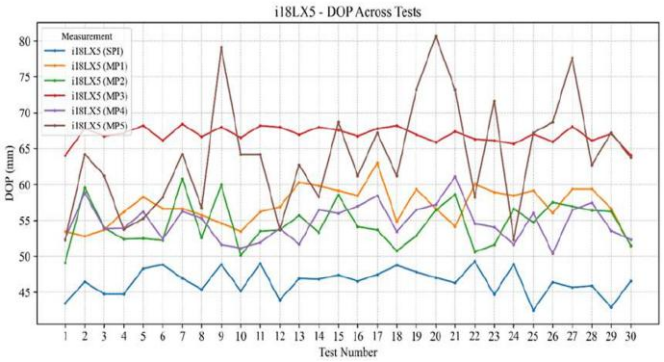

Fig. 3 DOP measurements for each test for the i18LX5 probe

Table 3: i24LX8 linear probe automated and manual DOP (mm) measurements

Test no.	SPI	MP1	MP2	MP3	MP4	MP5
1	29.50	56.79	58.27	54.87	58.18	78.03
2	30.18	59.49	46.47	54.77	58.41	68.59
⋮	⋮	⋮	⋮	⋮	⋮	⋮
30	29.86	60.91	55.13	55.49	57.60	61.12
Mean	30.22	57.09	54.44	55.10	55.66	42.22
SD	0.89	1.63	3.82	1.21	2.83	11.69

Table 4 demonstrates the coefficient of variance (COV) produced by both methods, for each probe. Equation 2 shows the calculation for the COV.

$$COV = (\sigma \div \mu) \times 100\% \quad (2)$$

where σ is the standard deviation, and μ is the mean, of recorded DOP measurements, for each probe.

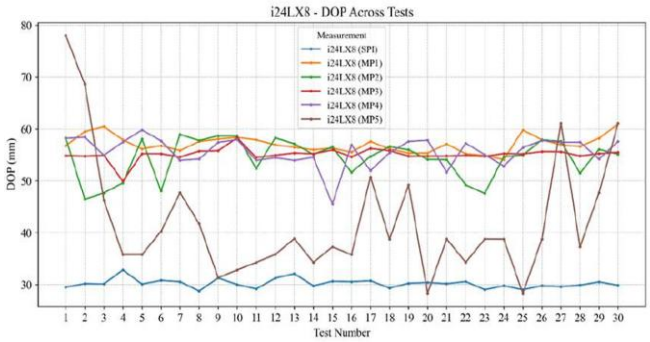

Fig. 4 DOP measurements for each test for the i24LX8 probe

Table 4: COV (%) for each probe

	i18LX5	i24LX8	i8CX1
SPI	4.04	2.96	2.57
MP1	4.68	2.85	1.89
MP2	5.68	7.10	2.41
MP3	1.69	2.20	1.67
MP4	4.77	5.08	1.92
MP5	12.06	27.68	8.55

IV. DISCUSSION

The findings confirm that the SPI method provides a more stable and repeatable measure of LCP than manual assessment. Manual readings demonstrated significant inter-observer variability, primarily linked to experience level and visual acuity of faint echoes. Less experienced participants tended to overestimate DOP by identifying faint residual patterns below the noise threshold.

In the SPI method, DOP underestimation in high-frequency linear probes arises from steeper attenuation and the use of a second-degree polynomial fit, which may not optimally capture the complex decay of the SNR tail. Alternative curve-fitting approaches, such as exponential or spline models, could better model the asymptotic decline of the signal. The TGC slider positions were noted, to be replicated for each image, to achieve consistency. However, given that the images were taken on different consecutive days, each time the TGC were readjusted to the initial positions recorded, which may have contributed to some variations. Therefore, reinforcing the need for a fixed TGC preset for routine QA to avoid any variations.

Although the SPI implementation employed a simplified vertical line profile, it effectively met the purpose of the LCP test, which is to monitor consistency across repeated acquisitions rather than determining absolute imaging limits. The low SD values indicate that the SPI method is well suited for longitudinal QA applications.

The results are consistent with prior findings by Gorny et al. (2005) [6], Gibson et al. (2001) [2], and Fiori et al. (2023) [7], which similarly emphasise the value of objective SNR-based assessment in maintaining QA reliability. While the SPI method's simplicity may limit precision at significant depths, its automation potential and reproducibility make it a promising tool for LCP evaluations.

V. CONCLUSIONS

The objective SPI method demonstrated superior repeatability and lower measurement variability than subjective visual assessment across multiple US probes. Agreement with manual results was strongest in the curvilinear probe, where attenuation effects are less pronounced. Differences between methods were accentuated in high-frequency probes, underscoring the need for consistent system settings. The study supports integration of SPI-based analysis into US QA protocols to ensure consistent, and observer-independent evaluation of imaging depth performance.

VI. RECOMMENDATIONS

To enhance precision, future research should:

- Explore higher-order or adaptive curve-fitting models.
- Incorporate machine learning approaches to automate threshold detection and region of interest (ROI) selection.
- Standardise imaging settings, including TGC, across QA sessions.
- Expand the study across multiple US systems and phantom types to validate generalisability.

VII. ACKNOWLEDGMENT

The author thanks the supervisory team, the Medical Imaging Department of Mater Dei Hospital, and all participating medical physicists for their contribution to data collection and analysis.

VIII. REFERENCES

1. Dudley, N. J. and Gibson, N. M. (2017). Is grey level a suitable alternative to low-contrast penetration as a serial measure of sensitivity in computerised ultrasound quality assurance? Ultrasound in Medicine & Biology, 43(2):541–545.
2. Gibson, N. M., Dudley, N. J., and Griffith, K. (2001). A computerised quality control testing system for b-mode ultrasound. Ultrasound in medicine & biology, 27(12):1697–1711.
3. Hangiandreou, N. J., Stekel, S. F., Tradup, D. J., Gorny, K. R., and King, D. M. (2011). Four-year experience with a clinical ultrasound quality control program. Ultrasound in medicine & biology, 37(8):1350–1357.

4. Grazhdani, H., David, E., Ventura Spagnolo, O., Buemi, F., Perri, A., Orsogna, N., Gigli, S., and Chimenz, R. (2018). Quality assurance of ultrasound systems: current status and review of literature. Journal of ultrasound, 21(3):173–182.
5. Goodsitt, M. M., Carson, P. L., Witt, S., Hykes, D. L., and Kofler, J. M. (1998). Real-time B-mode ultrasound quality control test procedures.
6. Gorny, K. R., Tradup, D. J., and Hangiandreou, N. J. (2005). Implementation and validation of three auto mated methods for measuring ultrasound maximum depth of penetration: application to ultrasound quality control. Medical physics, 32(8):2615–2628.
7. Fiori, G., Fuiano, F., Schmid, M., Conforto, S., Sciuto, S. A., and Scorza, A. (2023). A comparative study on depth of penetration measurements in diagnostic ultrasounds through the adaptive SNR threshold method. IEEE Transactions on Instrumentation and Measurement, 72:1–8.

Contacts of the corresponding author:

Author:	Dylan Robert Hewer
Institute:	University of Malta
Street:	Tal-Qroqq
City:	Msida
Country:	Malta
Email:	dylanhewer.dh@gmail.com

HOW TO

A PRIMER ON FACILITY SPECIFIC PRIMO MONTE CARLO MODELING AND INITIAL VALIDATION OF A 6 MV PHOTON BEAM ELEKTA INFINITY LINAC

G.F. Acquah[1], A.A. Frimpong[2], T.B. Dery[3]. M. Pokoo-Aikins[3]

[1] Medical Physics Department, RPS Oncology, MN, USA
[2] Medical Physics Department, University of Ghana, Accra, Ghana
[3] Radiological and Medical Sciences Research Institute, Ghana Atomic Energy Commission, Accra, Ghana

Abstract— **PRIMO Monte Carlo (MC) software is widely used to simulate clinical linear accelerators. This study presents a facility-specific primer for PRIMO modeling of a 6 MV photon beam from an Elekta Infinity single-energy LINAC, with emphasis on accurate LINAC geometry construction and absorbed-dose estimation in water phantom. A 6 MV photon beam was modeled in PRIMO to simulate absorbed-dose distributions in water, and the results were compared with experimental measurements. Percentage depth dose (PDD) curve and lateral beam profiles were evaluated, and agreement between simulated and measured data was quantified using a local gamma index criteria of 2.0% dose difference and 2.0 mm distance-to-agreement, with a 95.0% pass-rate threshold. The simulated and measured PDDs showed excellent agreement, with a gamma passing rate of 99.66%. Gamma passing rates for the in-plane and cross-plane beam profiles were 95.30% and 95.97%, respectively, within acceptable tolerances. PRIMO MC-based modeling was feasible for the facility's 6 MV photon beam LINAC. Measurement-based verification of absorbed-dose distributions in water showed that the facility's LINAC can be simulated with high fidelity for future clinical quality assurance (QA) and treatment planning system (TPS) verification.**

Keywords— **PRIMO MC-based software, Percentage depth dose, Beam profiles, Elekta Infinity LINAC.**

I. INTRODUCTION

Radiotherapy plays a central role in cancer management, relying on precise dose delivery to achieve therapeutic effectiveness while minimizing exposure to surrounding healthy tissues. Modern external beam radiotherapy commonly employs medical linear accelerators (LINACs), which generate high energy photon beams capable of targeting tumors with sub-millimeter precision. In these systems, electrons are accelerated through a waveguide vacuum to energies in the megavolt range. Upon exiting the accelerating structure, the electron beam typically exhibits a narrow spatial and energy distribution, forming the starting point for most Monte Carlo (MC) simulations, which assume a primary electron source with predefined characteristics [1–2].

Advances in computational power and algorithm development have established MC methods as the gold standard for radiotherapy dose calculation, owing to their ability to model particle transport with high fidelity, even in the presence of complex geometries and tissue heterogeneities. PRIMO, a user-friendly MC platform, has been developed specifically for simulating medical LINACs and has demonstrated accuracy and efficiency across a range of clinical applications [3–6].

This study used photon beam data from the Centre International de Cancérologie de Lomé (CICL), in Lome, Togo, with the objective of providing an initial evaluation of PRIMO's accuracy in modeling absorbed dose distributions for its 6 MV photon beam. By comparing the simulated absorbed dose distributions with measured data using a 2.0% Dose Difference (DD), 2.0mm Distance-to-Agreement (DTA) gamma index analysis criteria with a 95.0% gamma index passing rate. The study assesses the level of agreement between the two datasets and examines PRIMO's reliability as a possible independent dose verification tool [7].

Ultimately, this study serves as a facility-specific primer on PRIMO Monte Carlo modeling for an Elekta Infinity LINAC, offering an initial benchmark for accurate dose calculation and verification in support of clinical radiotherapy practice.

II. MATERIALS AND METHODS

Using a refrence10 × 10 cm² field size, percentage depth dose, cross-plane and in-plane dose profiles were measured and compared with the PRIMO-calculated/simulated absorbed dose distribution parameters. The depth of maximum dose (dmax) and dose at depth of 10.0 cm were analyzed to assess PRIMO's photon beam modeling accuracy for the single 6 MV beam-LINAC.

Elekta Infinity Linear Accelerator

The single-photon-beam Elekta Infinity provides clinical flexibility for treating a wide range of cancers. Its Agility multileaf collimator (MLC) system improves target conformity through rapid beam shaping and ultra-low transmission, helping reduce dose to critical structures. The system includes 160 leaves, each 5 mm wide, for precise beam shaping; a 15% larger dynamic field size; fast leaf speed; ultra-low MLC leakage; and a high-dose-rate flattening-filter-free (FFF) mode. Rubicon optical technology enables real-time MLC leaf positioning, while integrated imaging supports treatment verification and patient positioning.

PRIMO Monte Carlo-based Simulation Software

Simulations were performed using PRIMO *v0.1.5.1307*, a software package designed for LINAC modeling and radiotherapy dose calculation. PRIMO uses the PENELOPE Monte Carlo (MC) code to model particle transport and particle interactions, enabling accurate dose distribution calculations. The software was installed and run on an HP Pavilion 15 laptop equipped with an Intel Core i7-6700HQ processor, 8.0 GB RAM, CPU speed of 2.44 GHz and a 1 TB HDD. PRIMO was used to model the Elekta Infinity LINAC, including the treatment head geometry and beam-shaping components, define the water phantom geometry, and calculate percentage depth dose (PDD) curves and lateral dose profiles for the 6 MV photon beam.

Dosimetry equipment

This study utilized PTW's dosimetry equipment, including the following.

Beamscan water phantom*:* The PTW BEAMSCAN water phantom is a 3D scanning system used to measure LINAC beam-output data for comparison with PRIMO simulations. It includes a built-in two-channel electrometer for field and reference detector connections, as well as software for data acquisition, analysis, and processing. The phantom was positioned at a source-to-surface distance (SSD) of 100 cm. Measurements were acquired from 30.0 cm to 0.0 cm depth for percentage depth dose (PDD) curves and at 10.0 cm depth for lateral dose profiles using 3D ionization scanning chambers.

Semiflex 3-D detectors*:* The PTW Semiflex 3-D waterproof ionization chamber was used for the relative dosimetry. Its small sensitive volume of 0.07 cm^3 and high spatial resolution make it well suited for the LINAC's relative beam data dosimetry. In this study, the 3-D chambers were used to acquire PDD curves and beam profiles.

Beamscan software (MEPHYSTO): The BEAMSCAN software provides advanced tools for rapid and accurate beam data acquisition and data processing. In this study, MEPHYSTO was used to acquire, process, analyze, save, and export the measured PDD and beam profile data.

Experimental measurements

Photon relative dose measurements included percentage depth dose profile, cross-plane profile, and in-plane profile were performed with the BEAMSCAN water phantom placed directly under the LINAC. PDD data for the 6 MV energy were acquired for reference 10 x 10 cm^2 field size at SSD of 100 cm. The PDD measurement was carried out in 1.0 mm increment from 0.0 cm to 3.0 cm depth and in 2.0 mm increments from 3.0 cm to 30.0 cm depth using the PTW semiflex 3-D ion chamber (TM31021). For photon beam profile measurements, the water phantom was set up with a source-to-detector distance (SDD) of 110 cm, at an isocenter depth of 10 cm, with the collimator and gantry angle fixed at 0 degree. The PTW MEPHYSTO data acquisition software *version 3.4* was used for data analysis using the Elekta 2020 protocol for beam profiles analysis (Flatness and Symmetry) and the AFSSAPS No. 93 protocol used for the PDD analysis respectively.

PRIMO software simulation

The simulation began by modeling the facility's Elekta Infinity LINAC in PRIMO. Using PRIMO's predefined configurations for commercial LINACs, the Elekta Infinity model was reconstructed to obtain final primary beam parameters. The 6 MV photon beam mode was selected, and photon production was simulated by modeling the interaction of the electron beam with the tungsten target in the LINAC head. All four laptop central processing units (CPUs) were used during the simulation, achieving a speed of 16.9 histories/s per CPU. The vendor-provided initial electron beam parameters included an energy of approximately 6 MeV and a Gaussian spot size. These parameters were iteratively refined to improve agreement with experimental measurements, particularly the PDD curve and lateral dose profiles.

To ensure accurate simulation of beam shaping and attenuation processes, the Infinity's treatment head was modeled to include four key components. The primary collimator, flattening filter, secondary collimators and the MLCs. The primary collimator was simulated to shape the initial photon beam and to eliminate off-axis photons, ensuring proper alignment with the treatment field. For the flattening filter, a conical tungsten filter was modeled to produce a uniform dose distribution across the treatment

field, also attenuating the photon beam to create the characteristic 6 MV energy spectrum. The X and Y jaws were configured to define a 10 × 10 cm^2 field size at the isocenter, playing a critical role in shaping the beam to match the treatment field. The last component (MLC) although not actively used in this study, was included in the simulation for completeness, as it is an integral part of the Elekta Infinity LINAC's beam-shaping system.

PRIMO generated a phase-space file at the end of the treatment head, containing detailed information for all particles leaving the LINAC head. This file was used as input for the subsequent dose calculation stage in the water

phantom. Absorbed dose distributions were then calculated in a virtual water phantom designed to replicate the experimental measurement setup. A 30 × 30 × 30 cm³ water phantom was modeled to provide adequate scatter conditions for the photon beam. The phantom was divided into 2 × 2 × 2 mm³ voxels to achieve high spatial resolution while maintaining computational efficiency and accurately representing dose gradients, particularly in the build-up and penumbra regions. The SSD was set to 100 cm, matching the experimental setup. The field size was defined as 10 × 10 cm² at the isocenter, which was achieved by configuring the positions of the secondary collimators (jaws) in the LINAC model. These parameters ensured that the simulation conditions were identical to those used in the experimental measurements.

Segments Simulation Process

The simulation was divided into two main stages, S1+S2 and S3, which correspond to the Monte Carlo modeling workflow shown in Figure 1. In the first stage, particle transport through the LINAC head (S1+S2) was simulated, including interactions among photons, electrons, and treatment head components such as the target, primary collimator, flattening filter, and jaws. This stage produced a phase-space file describing the beam exiting the treatment head. To improve efficiency without compromising accuracy, variance reduction methods, including enhanced bremsstrahlung splitting, were applied. In the second stage, the phase-space file was used for dose calculation in the water phantom (S3). Using the EGSnrc-DOSXYZnrc module, PRIMO calculated the absorbed dose in each voxel while accounting for secondary-particle interactions, including Compton scattering, pair production, and electron transport. The resulting 3-D dose distribution was used to generate PDD curve and lateral dose profiles, as shown in Figure 1. The total simulation time was 34 hours, 25 minutes, and 13 seconds.

Prior to simulation, the particle histories were configured to minimize statistical uncertainties. A total of 10^8 particle histories was simulated based on convergence tests, ensuring that the relative uncertainty in the dose calculation was below 1.0% in regions of clinical interest (d_{10cm} and d_{max}). The energy cutoffs were also configured and set to 10 keV for photon transport, and for electron transport to 521 keV (corresponding to the rest mass energy of electrons). These cutoffs ensured accurate modeling of low-energy interactions while optimizing computational efficiency. The final configuration was the variance reduction techniques. Variance reduction techniques such as the range rejection and directional bremsstrahlung splitting were implemented to enhance computational speed without compromising the accuracy of the dose calculations.

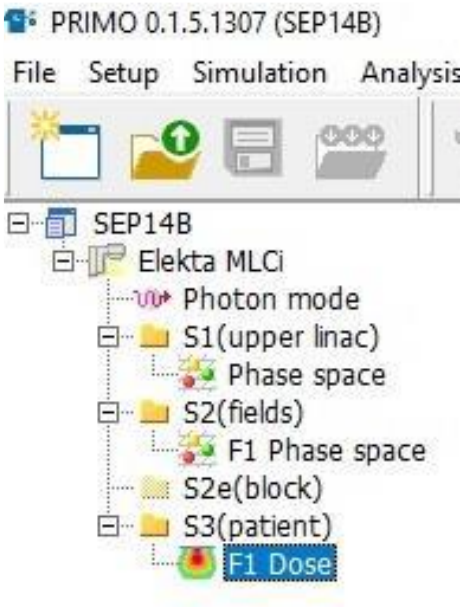

Fig. 1 PRIMO interface showing the three various simulated segments.

Simulation Output Analysis

The simulated (calculated) absorbed dose distributions were compared with experimental measurements (measured). The relative dose as a function of depth in the water phantom was generated and normalized at 100% of maximum dose. This curve (calculated PDD) was compared with the measured PDD using a local gamma index passing criteria of 2.0%, 2.0 mm to assess the accuracy of the simulation in modeling dose penetration as captured in Figure 2. The red smooth curve is the measured PDD while the violet rough curve is the Primo calculated PDD.

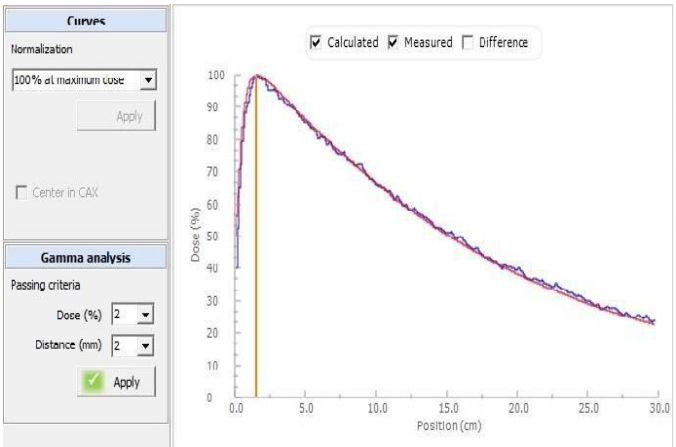

Fig. 2 PDD curves in PRIMO interface using gamma analysis

III. RESULTS AND DISCUSSIONS

Table 1 summarizes the final simulated electron parameters obtained after optimizing the initial electron beam parameters provided by the PRIMO developers for Elekta LINACs.

Table 1. Final simulation parameters

Initial Energy (MeV)	Energy FWHM (MeV)	Focal spot FWHM (cm)	Beam divergence (degree)
6.495	0.022	0.190	0.000

Table 2 summarized the statistics of particle transport during the PRIMO MC simulation of the facility's LINAC 6 MV photon beam. A total of 39,569,578 particles were simulated, including electrons, photons, and positrons, with detailed tracking of their energy ranges and production per history. The total particle counts included all three particle types, with an average of 1.6401 particles per history. The energy range for the total particles extended from 0.02 MeV to 6.490 MeV. These statistics highlight the dominance of photons in the simulation, reflecting the nature of a 6 MV photon beam, while secondary particles like electrons and positrons contributed to dose deposition through scattering and other interactions.

Table 2. Particle transport statistics for the simulated 6 MV photon beam

Particles	Counts	Particles/History	Min E (MeV)	Max E (MeV)
Electrons	178,552	0.022202	0.000	6.103
Photons	39,385,536	4.897345	0.020	6.490
Positrons	5,490	0.000683	0.102	5.050
TOTAL	39,569,578	4.920230	n/a	n/a

From figure 2 above, a strong correlation was observed between the simulated and measured PDD curves. The dmax was consistently located at a depth of 1.5 cm in both datasets, aligning with expected characteristics of 6 MV photon beams. Beyond the build-up region, the dose decreases progressively, with the simulated and measured curves demonstrating agreement within 5.0% throughout the dose fall-off region. All statistical assessments of the PDD dosimetric parameters analysed and compared are presented in Table 3.

The build-up region, extending from the surface to the depth of maximum dose (d_{max}), showed a rapid dose increase mainly due to the generation and scattering of secondary electrons. The PRIMO simulation reproduced this rise closely and agreed well with the experimental data, supporting the accuracy of the modeled initial beam energy and focal spot size. Minor differences in the build-up region may be attributed to experimental uncertainties, such as detector positioning errors, or to limitations in modeling secondary electron transport.

Table 3. Measured and calculated PDD comparison analysis

Points of comparison	**Measured**	**Simulated**	**Abs difference**
Position of Max (cm)	1.50	1.50	0.00
Dose at 10 cm depth	66.29	65.77	0.52
Gamma index			
Percentage of points passing the 2.0%/2.0mm criteria (%)	**99.66**		

A detailed comparison of the measured and calculated PDD curves analyzed using the PRIMO software is presented in Figure 3. This figure provides a comprehensive visualization of the agreement between the two curves, highlighting the accuracy of the PRIMO simulation in replicating the experimental data.

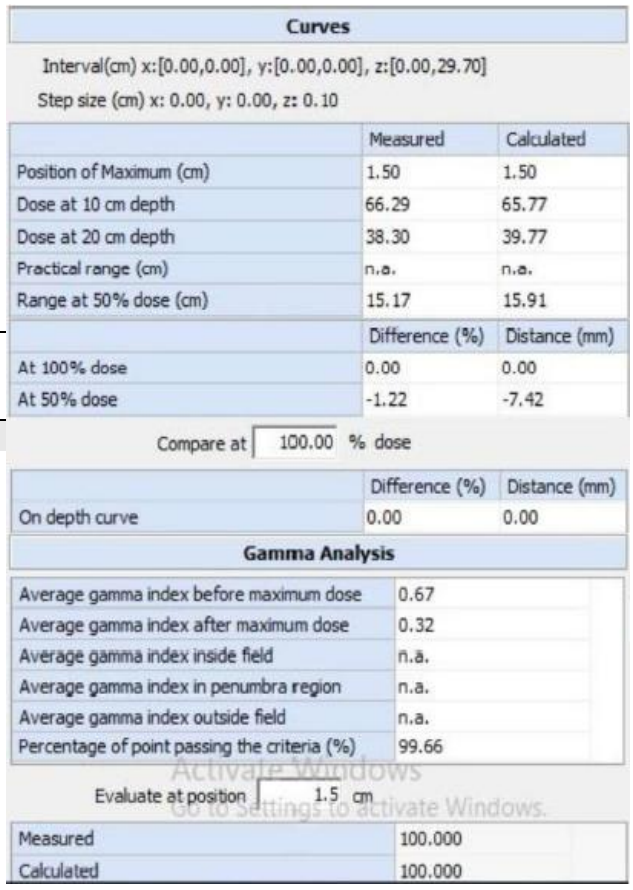

Fig. 3 Measured and calculated PDD comparison in PRIMO interface.

The simulated and measured depth dose curves both exhibited a maximum dose (d_{max}) at approximately 1.5 cm, consistent with the characteristic behavior of 6 MV photon beams. Normalizing both measured and PRIMO-calculated doses to 100% at d_{max} established a consistent reference point for comparison. The close agreement at dmax confirms the accuracy of the simulated energy spectrum characteristics.

Accurately reproducing d_{max} is crucial for clinical applications, particularly in treating superficial tumors, where precise dose delivery is essential for effective treatment outcomes. Beyond the depth of maximum dose, the dose gradually decreases due to the attenuation and scattering of photons within the water phantom. The PRIMO simulation demonstrated excellent agreement with the experimentally measured dose fall-off curve, accurately capturing photon interactions at increasing depths. This concurrence is critical for ensuring reliable dose predictions in deeper tissues, particularly for tumors situated in midline or posterior regions, where accurate dosimetry is vital for effective treatment planning.

At the depth of 10 cm, the measured dose was 66.3%, while the PRIMO-calculated dose was 65.8%. The percentage difference between the measured and simulated doses at depth of 10 cm was 0.79%, which falls well within clinically acceptable 1.0% limit. This close agreement underscores the accuracy of the Monte Carlo model in predicting dose attenuation and scatter effects, which are essential for ensuring precise dose delivery to deep-seated tumors. For the 10 × 10 cm² field size, the gamma passing rate surpassed 95% under the 2.0%/2.0 mm criteria, a standard benchmark for clinical dose verification. The gamma index evaluates both dose magnitude differences and spatial discrepancies between simulated and measured data. Achieving a passing rate above 95% indicates that the PRIMO simulation demonstrated excellent agreement with experimental measurements centrally. This high passing rate of 99.66% underscores PRIMO's reliability for future clinical quality assurance, dose verification, and treatment planning system validation for the facility.

The profiles were also examined in two perpendicular directions; the transverse (X-profile/In-plane) and longitudinal (Y-profile/ Cross-plane), at a depth of 10 cm using a reference 10 × 10 cm² field size. These profiles play a crucial role in assessing the accuracy of PRIMO Monte Carlo simulations in replicating the dose distributions delivered by the facility's LINAC, providing valuable insights into the reliability of the simulation model.

Table 4 and Table 5 respectively present the beam profiles in both transverse and longitudinal directions which demonstrated a high degree of agreement between PRIMO simulations and experimental measurements. The flatness and symmetry of the central region were modeled with high precision. Both the simulated in-plane and cross-plane beam profiles when compared to the measured profiles recorded local gamma index pass rate above the 95.00% threshold criteria. PRIMO effectively captured the rapid dose fall-off beyond the field edges, accurately accounting for scatter and leakage radiation.

Table 4. Measured and calculated transverse beam profile comparison analysis

Points of comparison	Measured	Simulated	Abs. difference
Left off-axis distance at 50% dose (cm)	-6.05	-5.98	0.07
Right off-axis distance at 50% dose (cm)	6.10	5.99	0.11
Gamma index			
Percentage of points passing the 2.0%/2.0mm criteria (%)	**95.30**		

Table 5. Measured and calculated longitudinal beam profile comparison analysis

Points of comparison	Measured	Simulated	Abs. difference
Left off-axis distance at 50% dose (cm)	-6.20	-6.12	0.08
Right off-axis distance at 50% dose (cm)	6.20	6.07	0.13
Gamma index			
Percentage of points passing the 2.0%/2.0mm criteria (%)	**95.97**		

IV. CONCLUSION

The simulation of the facility's single-energy 6 MV Elekta Infinity LINAC was demonstrated to be fully feasible using the PRIMO Monte Carlo software. The study successfully established an accurate, facility-specific PRIMO model through careful reconstruction of the LINAC geometry and detailed configuration of beam parameters. PRIMO achieved excellent agreement with the machine's measured data, reproducing the reference percent depth dose (PDD) curve and lateral dose profiles with high fidelity. These results confirm that PRIMO can reliably estimate absorbed dose in water phantom for this LINAC, supporting its use as a robust tool for independent dose verification and advanced radiotherapy simulation tasks. Although the simulation achieved strong dosimetric agreement, the simulation-based data verification would benefit from higher particle histories or longer simulation times, or alternatively, the use of a more powerful CPU (e.g., an 8-core system). These improvements would further smooth the calculated curves and help achieve a 100% gamma pass rate with minimal deviations from other vital absorbed dose distribution measured parameters (points of comparison). With enhanced computational resources, the total simulation time could be reduced to 1–3 hours, compared to the 34 hours required in this study.

Further research should extend PRIMO validation to more complex treatment scenarios, including small and irregular fields as well as dynamic techniques such as intensity modulated radiotherapy (IMRT) and volumetric modulated arc therapy (VMAT). As PRIMO becomes more routinely implemented in the facility, it can be incorporated into routine QA workflows as an independent verification tool, particularly for this busy facility with limited LINAC access for patient-specific QA. Beyond clinical use, PRIMO can also be used for education and research, enabling investigations into advanced LINAC modeling, dose optimization strategies, and emerging treatment modalities.

Overall, this work serves as a starting point for the facility, providing a validated PRIMO configuration and a pre-calculated phase-space file that future users can adopt and refine for subsequent modeling, verification, and research applications.

ACKNOWLEDGMENT

The authors acknowledge the medical physicist and staff of the radiotherapy facility for their support throughout this project. Their assistance with LINAC access and machine data measurements made this study possible.

REFERENCES

1. Ahnesjö A, Saxner M, Trepp A, et al. (1992) A pencil beam model for photon dose calculation. Med Phys. 19(2):263- 73.
2. Sheikh-Bagheri D, Rogers DW et al. (2002) Monte Carlo calculation of nine megavoltage photon beam spectra using the BEAM code. Med Phys. 29(3):391-402.
3. Rodriguez M, Sempau J, Brualla L et al. (2013) PRIMO: a graphical environment for the Monte Carlo simulation of Varian and Elekta Linacs. Strahlenther Onkol.189(10):881-886.
4. Rodriguez M, Sempau J, Fogliata A, et al. (2015) A geometrical model for the Monte Carlo simulation of the TrueBeam Linac, Phys. Med. Biol. 60 (2015) N219 N229.
5. González W, García-Ferreira I-B, Anguiano M, et al. (2015) A general photon source model for clinical Linac heads in photon mode, Rad. Phys. Chem. 117, 140-152.
6. Brualla L, Rodriguez M, and Lallena A.M (2016), Monte Carlo systems for treatment planning and dose verification, Strahlenther. Onkol. 193, 243 259.
7. Sempau J, Wilderman S.J, and Bielajew A.F (2000) DPM, a fast, accurate Monte Carlo code optimized for photon and electron radiotherapy treatment planning dose calculations, Phys. Med. Biol. 45,2263 2291.

Contacts of the corresponding author:

Author:	George Felix Acquah, PhD.
Institute:	RPS Oncology
Street:	5955 Norwich Ave N, Stillwater
City:	MN
Country:	USA
Email:	gacquah.felix@gmail.com

ASSESSMENT OF PATIENT RADIATION DOSE TO UPDATE LOCAL DRLs FROM NEWLY INSTALLED CT SYSTEMS

W. Suksancharoen[1], S. Ruenjit[1], A. Krisanachinda[2]

[1] Department of Radiology, King Chulalongkorn Memorial Hospital, Thai Red Cross Society, Bangkok, Thailand
[2] Department of Radiology, Faculty of Medicine, Chulalongkorn University, Bangkok, Thailand

Abstract. — **After the installation of two Computed Tomography (CT) systems between the year 2018 and 2020, at King Chulalongkorn Memorial Hospital, Bangkok, Thailand, the Local Diagnostic Reference Levels (LDRLs) for CT examinations had been established in 2022 for the optimization of radiation protection of patients. Other three CT systems were installed in the year 2022, 2024 and 2025, with more CT examinations on both anatomical and clinical indications. The objectives of this study are to assess the patient radiation dose and update the LDRLs for the optimization on patient dose and image quality. Patient radiation dose had been collected from all CT examinations at the Division of Diagnostic Radiology, Department of Radiology, King Chulalongkorn Memorial Hospital (KCMH), Thai Red Cross Society, in the year 2025. The data included the patients aged 18 years and above with the body weight between 45 and 75 (60 ± 15) kg. Eight common CT examinations based on the location region, include: 1) Brain 2) Brain including cervical spine 3) Neck 4) Chest 5) The angiography of the whole aorta 6) Upper abdomen multi - phases 7) Whole abdomen 8) Chest and whole abdomen. In addition, eight common CT examinations based on clinical diagnostic indications had also been collected as: 1) CTA carotid system for acute stroke 2) CTPA (CT pulmonary angiography) 3) Low-dose CT screening for lung cancer 4) HRCT 5) Coronary artery calcium scoring 6) Coronary CTA with retrospective ECG gating 7) Acute appendicitis 8) Urinary stone detection. Both results on LDRLs - Location and Clinical Indications based were compared to the National Diagnostic Reference Levels (NDRLs Thailand) updated in 2025. The updated LDRLs for most CT protocols in this study were lower than the NDRL CT, and close to the previous LDRL established in 2022.**

Keywords— **Diagnostic Reference Levels, Clinical Indication DRLs, Local DRL, National DRL, Computed Tomography.**

I. INTRODUCTION

The establishment of Diagnostic Reference Levels (DRLs) is one of the tools for controlling and optimizing the patient radiation dose from CT examinations [1-5]. DRLs serve as a benchmark for comparing patient radiation doses to the national or international standards, enabling the identification and timely revision of examination protocols according to unnecessary high radiation doses.

After the clinical applications of the new CT scanners, the patient radiation doses from various parameters, selected protocols, software functionality, and dose-reduction technologies should be considered and compared to the previous LDRLs for changes. As a result, the previously established LDRLs within the institution may no longer reflect the current clinical practice. Continued use of outdated LDRLs may therefore lead to inaccurate assessments of patient radiation dose.

Therefore, it is necessary to evaluate the patient radiation doses especially from the new CT systems to establish and update the LDRLs for the modern CT technology, to align with the recommendations from the International Commission on Radiological Protection (ICRP) and the International Atomic Energy Agency (IAEA) for the patient dose management [6-8]. Updated LDRLs with accurate information will help improving the quality of CT examinations, enhancing the patient safety, and supporting the long-term development on the effective use of radiation in the department.

This will enable us to evaluate the Local Diagnostic Reference levels (LDRLs) for all CT scanners in the hospital. LDRLs for CT examinations in 2025 will be compared to LDRLs for CT examinations in 2022, and the National Diagnostic Reference Levels (NDRLs, 2025) [9]. The results will provide further improvement and optimization of radiation dose management for the hospital.

II. MATERIALS AND METHODS

Study design and setting

The analytical, observational, retrospective study has been conducted at Department of Radiology, King Chulalongkorn Memorial Hospital. The Institutional Review Board, Faculty of Medicine Chulalongkorn University approved the COA No.0360/2026 IRB No.0017/69 title “Assessment of Patient Radiation Dose to Update Local DRLs from Newly Installed CT Systems”. Patient radiation dose had been collected from all CT examinations performed at the Division of Diagnostic Radiology, Department of Radiology, King Chulalongkorn Memorial Hospital, in the year 2025. The study includes all patients aged 18 years and above with body weight between 45 and 75 (60 ± 15) kg. The study covers eight CT examination protocols of common anatomical region, with the number of examinations as shown in Table 1. Eight CT examination protocols of common clinical diagnostic indications, with the number of examinations are shown in Table 2.

Table 1 Eight CT examination protocols based on common anatomical regions or Location-based and number of examinations for each protocol

CT examination protocols	Number of Exams
1. Brain	5,312
2. Brain including cervical spine	239
3. Neck	1,128
4. Chest	6,749
5. CT angiography of whole aorta	186
6. Upper abdomen multi-phases	2,999
7. Whole abdomen	2,927
8. Chest and whole abdomen	5,516
Total CT Examinations	**25,056**

A total number of 27,790 examinations from 16 CT examination protocols were included in the study (Table1 and Table2). The radiation metric, Volumetric CT Dose Index, $CTDI_{vol}$, and Dose Length Product, DLP values were collected from the Dose Monitoring System (DMS), using the Radimetrics software (version 3.4.2), manufacturer Bayer, S/N HPE: SGH729XNK3.

The specification of five CT scanners serviced at the Division of Diagnostic Radiology, Department of Radiology, King Chulalongkorn Memorial Hospital, Thai Red Cross Society as shown in Table 3, are variety, depend on the technology between manufacturers and the year of installation, which affect the patient radiation dose. [10-12].

New CT scanners are typically equipped with advanced software and technologies designed for the patient dose reduction while maintaining the image quality for clinical interpretation by radiologists [13-14]. These technological differences may directly influence the LDRLs for CT examinations.

Table 2 Eight CT examination protocols based on clinical indications or Indication-based and number of examinations for each protocol.

CT examination protocols	Number of Exams
1. CTA carotid system for acute stroke	1,251
2. CTPA	419
3. Low-dose screening for lung cancer	88
4. HRCT	347
5. Coronary artery calcium scoring	103
6. Coronary CTA retrospective ECG gating	71
7. Acute appendicitis	64
8. Urinary stone detection	391
Total CT Examinations	**2734**

Table 3 Specifications of five CT Equipment at King Chulalongkorn Memorial Hospital, Thai Red Cross Society. (Mar 2026)

Specifications	Manufacturers				
	GE	Philips	GE	GE	Siemens
Model	Revolution CT EX	Incisive	Revolution CT Apex	Revolution CT Apex Elite	Somatom Force
Year of installation	2018	2020	2022	2024	2025
Detector rows	256	64	256	256	192 (96x2)
Maximum detector coverage (cm)	16	4	16	16	18.4
Detector element size (mm)	0.625	0.625	0.625	0.625	0.6
kV range	70 – 140	70 – 140	70 – 140	70 – 140	70 - 150
Dual energies	Ultrafast kVp switching	N/A	Ultrafast kVp switching	Ultrafast kVp switching	Dual Sources
keV range	40-140	N/A	40-140	40-140	40-190
Dose modulation	Smart mA Auto Prescription	3D Dose-Modulation (3D-DOM)	Smart mA Auto Prescription	Smart mA Auto Prescription	CARE Dose 4D

In 2025, Department of Medical Sciences, Ministry of Public Health, Thailand, updated and published NDRL for CT examinations conducted in diagnostic radiology for the $CTDI_{vol}$ and DLP (75^{th} percentile). The NDRLs categorized on the location-based CT examinations in adults, comprise of eight examinations as shown in Table 4. The eight examination types of CT on clinical indication-based in adults of smaller examination numbers than the location based is shown in Table 5, resulting of 16 CT examination types in total.

Table 4 National Diagnostic Reference Levels (NDRLs) - CTDIvol and DLP (75^{th} percentile), Location-based CT Examinations for adults in 2025 [9].

CT Examinations	CTDIvol (mGy)	DLP per phase (mGy·cm)	Total DLP per study (mGy·cm)
1. Brain	58.0	1,188	-
2. Brain including cervical spine	58.1	1,483	-
3. Neck	18.4	653	1,139
4. Chest	10.2	381	766
5. CT angiography of whole aorta	10.5	862	2,446
6. Upper abdomen multi-phases	11.8	392	1,536
7. Whole abdomen	12.5	631	2,059
8. Chest and whole abdomen	12.4	838	2,339

Table 5 National Diagnostic Reference Levels (NDRLs) - CTDIvol and DLP (75thpercentile), Indication-based CT examinations for adults in 2025[9].

CT Examinations	Phantom diameter (cm)	NDRLs Thailand	
		CTDIvol (mGy)	DLP (mGy·cm)
1. CTA carotid system for acute stroke			
Arterial phase (vertex to aortic arch)	32	15.4	601
	16	30.8	1,202
All phases	32	-	2,001
	16	-	4,002
2. CTPA			
Arterial phase	32	12.0	429
All phases	32	-	1,234
3. Low-dose screening for lung cancer			
Non-contrast phase	32	2.4	101
4. HRCT			
Supine, inspiration, helical mode	32	10.2	388
Supine, expiration, helical mode	32	8.8	314
All phases	32	-	693
5. Coronary artery			
Calcium scoring	32	7.8	118
6. Coronary CTA			
Retrospective ECG gating	32	46.8	808
All phases	32	-	1,197
7. Acute appendicitis			
Single phase	32	12.2	491
All phases	32	-	902
8. Urinary stone detection			
Non-contrast phase	32	12.8	621

III. RESULTS

From the collected data of patients who underwent CT examinations that met the predefined inclusion criteria using five CT systems, 27,790 examinations covering 16 protocols were included in 2025. Statistical analysis was performed to determine the 50th percentile (median) values of CTDIvol (mGy) and DLP (mGy·cm) for examinations protocols based on common anatomical regions (Location-based) and protocols based on clinical indications (Indication-based). The Local Diagnostic Reference Levels (LDRLs) was updated and presented in Tables 6 and 7.

Table 6 Comparison of the Local DRLs (50th percentile) at KCMH to the NDRLs (75th percentile) Thailand, Japan, Korea, USA (ACR DIR) and RDRLs (50th percentile) EU for Location-based CT Examinations for adults in 2025 for CTDIvol (mGy) and DLP (mGy.cm).

CT Examinations	LDRL KCMH (50th percentile) 2025		LDRL KCMH (50th percentile) 2022		NDRLs Thailand (75th percentile) 2025		NDRLs Japan (75thpercentile) 2025		NDRLs Korea (75th percentile) 2021		NDRLs USA ACR DIR (75th percentile) 2017		RDRL EU (50th percentile of NDRLs) 2021	
	$CTDI_{vol}$ (mGy)	DLP (mGy·cm)	$CTDI_{vol}$ (mGy)	DLP (mGy·cm)	$CTDI_{vol}$ (mGy)	DLP (mGy·cm)	$CTDI_{vol}$ (mGy)	DLP (mGy·cm)	$CTDI_{vol}$ (mGy)	DLP (mGy·cm)	$CTDI_{vol}$ (mGy)	DLP (mGy·cm)	$CTDI_{vol}$ (mGy)	DLP (mGy·cm)
1. Brain	50.0	1,090	46.9	988	58.0	1,188	67	1,260	52.2	970	57	1011	48	1386
2. Brain including cervical spine	46.9	1,774	-	-	58.1	1,483	-	-	-	-	-	-	-	-
3. Neck	14.0	496	15.5	466	18.4	653	-	-	13.4	597	20	572	-	-
4. Chest	7.2	284	9.3	371	10.2	381	11	430	7.6	324	16	596	9	364
5. CT angiography of Whole Aorta	8.8	599	-	-	10.5	862	-	-	-	-	-	-	-	-
6. Upper Abdomen Multi-phases	11.6	369	10.5	291	11.8	392	13	-	9.3	-	-	-	9	-
7. Whole Abdomen	11.5	584	9.9	437	12.5	631	14	720	8.9	474	19	995	9	874
8. Chest and Whole Abdomen	11.4	808	9.3	606	12.4	838	13	940	-	-	-	-	-	-

Table 7 Comparison of the LDRL (50th percentile) at KCMH to the NDRLs (75th percentile) Thailand, Japan, Korea, USA (ACR DIR) and RDRLs EU on Indication-based CT Examinations for adults in 2025 - CTDIvol (mGy) and DLP (mGy.cm).

CT Examinations	Phantom diameter (cm)	LDRLs (KCMH) (50th percentile) 2025		LDRLs (KCMH) (50th percentile) 2022		NDRLs Thailand (75th percentile) 2025		NDRLs Japan (75th percentile) 2025		NDRLs Korea (75th percentile) 2021		NDRLs USA ACR DIR (75th percentile) 2017		RDRL EU (50th percentile of NDRLs) 2021	
		CTDIvol (mGy)	DLP (mGy·cm)	CTDIvol (mGy)	DLP (mGy·cm)	CTDIvol (mGy)	DLP (mGy·cm)	CTDIvol (mGy)	DLP (mGy·cm)	CTDIvol (mGy)	DLP (mGy·cm)	CTDIvol (mGy)	DLP (mGy·cm)	CTDIvol (mGy)	DLP (mGy·cm)
1. CTA carotid system for acute stroke															
Arterial phase (vertex	32	9.5	391	9.4	385	15.4	601	-	-	-	-	-	-	-	-
to aortic arch)	16	-	-	-	-	30.8	1,202	-	-	-	-	-	-	-	-
All phases	32	-	-	-	-	-	2,001	-	-	-	-	-	-	-	-
	16	-	-	-	-	-	4,002	-	-	-	-	-	-	-	-
2. CTPA															
Arterial phase	32	9.2	321	12.2	389	12.0	429	12.0	-	-	-	18.0	557	8.0	628
All phases	32	-	-	-	389	-	1,234	-	2,300	-	-	-	-	-	-
3. Low-dose screening for lung cancer															
Non-contrast phase	32	2.9	128	3.6	252	2.4	101	-	-	2.7	110	-	-	-	-
4. HRCT															
Supine inspiration helical mode	32	7.6	291	6.7	259	10.2	388	-	-	-	-	-	-	-	-
Supine expiration helical mode	32	1.9	63	-	-	8.8	314	-	-	-	-	-	-	-	-
All phases		-	-	-	307	-	693	-	-	-	-	-	-	-	-
5. Coronary artery															
Calcium scoring	32	3.7	60	2.7	43	7.8	118	8.0	160	5.9	96	-	-	4.0	81
6. Coronary CTA															
Retrospective ECG gating	32	44.7	815	59.5	1,090	46.8	808	57	940	-	-	-	-	-	-
Prospective ECG gating		21.5	307	23.1	301	-	-	49	770	19.2	327	-	-	25.0	459
All phases	32	-	-	-	-	-	1,197	-	-	-	-	-	-	-	-
7. Acute appendicitis															
Single phase	32	10.4	387	11.3	430	12.2	491	-	-	-	-	-	-	-	-
All phases	32	-	-	-	430	-	902	-	-	-	-	-	-	-	-
8. Urinary stone detection															
Non-contrast phase	32	3.5	193	7.2	359	12.8	621	-	-	-	-	-	-	-	-

IV. DISCUSSION

The Department of Medical Sciences has updated the National Diagnostic Reference Levels (NDRLs) for diagnostic imaging using computed tomography (CT) in the year 2025, for both Location-based and Indication-based categories, in order to ensure that the reference values are up-to-date and standardized. This update aims to provide consistent benchmarks for diagnostic dose reference values, protect the patients from the high radiation dose, promote the safe use of radiation, and prevent radiation hazards in accordance with established standards [15-18].

At King Chulalongkorn Memorial Hospital, The Thai Red Cross Society, several high-performance CT systems are in clinical service. To maintain institutional standards and support proper and appropriate radiation dose management, the hospital has therefore updated its local diagnostic reference levels to reflect the performance of these newly installed CT systems. The updated LDRL (2025) were subsequently compared to the previous LDRL established in 2022 and the NDRLs Thailand announced by the Department of Medical Sciences in 2025, across all 16 key protocols, for both Location-based and Indication-based examinations.

The results showed that the LDRLs KCMH for most examination protocols in this study were lower than the NDRLs Thailand and close to previous LDRL KCMH established in 2022. In addition, the results were compared to NDRLs in Asian countries, such as Japan and Korea [19-20]. The LDRL 2025 (KCMH) was lower than NDRLs reported by Japan in 2025, but $CTDI_{vol}$ Neck, Upper Abdomen and Whole Abdomen were higher than NDRLs Korea in 2021.

Furthermore, when compared LDRLs KCMH with the US and EU, the LDRLs (KCMH) was lower than NDRL reported by American College of Radiology (ACR) (2017) [21]. CTDIvol Brain, Upper Abdomen and Whole Abdomen were higher than the European Union (EU) estimated at 50th percentile (median) of NDRL (2021) [22], as shown in Tables 6 and 7.

In this study, LDRL for brain including cervical spine protocol on location based, the CTDIvol is lower than the NDRLs Thailand; however, the DLP is higher than the NDRLs Thailand due to the long scan length. Number of phases is another parameter increasing the radiation metric, DLP. Therefore, the training and education should be provided to CT personnel to raise awareness of the importance of appropriate scan range and number of phases

and to establish suitable anatomical reference points for the organs being examined in order to address this issue. For Indication-based, most protocols particularly coronary artery examination for calcium scoring and urinary stone detection showed LDRLs are relatively lower than the NDRLs Thailand and other countries. The image quality remained sufficient for radiologists to interpret the images accurately. This result is attributed to the performance of modern CT scanners, equipped with advanced dose-reduction software and technologies that enhance image quality while reducing radiation exposure.

V. CONCLUSION

The installation of five CT scanners at the Department of Radiology, KCMH, from 2018 to 2025 led to the establishment of LDRLs CT in 2022 and updated in 2025 for both location and clinical indication based. The LDRL clinical indications showed the radiation doses tailored to specific disease areas, maximize patient benefits and appropriateness of care. It is worth noting that besides considering anatomical-based DRLs, determining radiation doses tailored to specific disease areas can maximize patient benefits and appropriateness of care. This approach leads to better outcomes for patients, as it ensures appropriate radiation doses while maintaining diagnostic efficacy.

It is also important to update the clinical practices and provide the continuous training for personnel to ensure proper use of the technology and to raise awareness of appropriate radiation dose management for patients. Such efforts will contribute to improving healthcare services and promoting radiation safety in the near future.

REFERENCES

1. Kanal K.M., Butler P.F., Sengupta D., Bhargavan-Chatfield M., Coombs L.P., Morin R.L.U.S. diagnostic reference levels and achievable doses for 10 adult CT examinations. Radiology. 2017; 284:120–133. doi: 10.1148/radiol.2017161911.
2. Vañó E., Miller D.L., Martin C.J., Rehani M.M., Kang K., Rosenstein M., Ortiz-López P., Mattsson S., Padovaniet R., Rogers A., et al. ICRP Publication 135: Diagnostic reference levels in medical imaging. Ann. ICRP. 2017; 46:1–144. doi: 10.1177/0146645317717209.
3. IPEM. Guidance on the establishment and use of diagnostic reference levels for medical x-ray examinations. IPEM Report 88. 2004.
4. Tonkopi E, Manos D, Tonkopi E, Duffy S, Abdolell M, Manos D. Diagnostic reference levels and monitoring practice can help reduce patient dose from CT examinations. AJR Am J Roentgenol 2017;208: 1073e81.
5. Foley S.J., McEntee M.F., Rainford L.A. Establishment of CT diagnostic reference levels in Ireland. Brit. J. Radiol. 2012; 85:1390–1397. doi: 10.1259/bjr/15839549
6. International Commission on Radiological Protection (1996) ICRP publication 73: Radiological protection and safety in medicine. Ann ICRP 26(2)
7. International Commission on Radiological Protection. ICRP 103: the 2007 recommendations of the international commission on radiological protection. Ann ICRP 2007; 37:330.
8. IAEA. Radiation Protection and Safety of Radiation Sources: International Basic Safety Standards. General Safety Requirements Part 3, No GSR Part 3 Interim; International Atomic Energy Agency: Vienna, Austria, 2014; Volume 3, pp. 1–303.
9. Department of Medical Sciences. Diagnostic reference levels for computed tomography (CT). Notification of the Ministry of Public Health, B.E. 2568 (2025). Nonthaburi, Thailand: Department of Medical Sciences; 2025. Available from: https://webapp1.dmsc.moph.go.th/petitionxray/web/download/%E0%B8%9B%E0%B8%A3%E0%B8%B0%E0%B8%81%E0%B8%B2%E0%B8%A8%20DRLs%20CT%202568.pdf. Accessed March 11, 2026.
10. McCollough, C. H. ; Primak, A. N. ; Braun, N. ; Kofler, J. ; Yu, L. ; Christner, J. Strategies for reducing radiation dose in CT. Radiol. Clin. N. Am. 2009, 47, 27–40.
11. Duan, X.;Wang, J.; Yu, L.; Leng, S.; McCollough, C.H. CT scanner X-ray spectrum estimation from transmission measurements. Med. Phys. 2011, 38, 993–997.
12. Loose RW, Vano E, Mildenberger P, et al. Radiation dose management systems requirements and recommendations for users from the ESR Euro Safe imaging initiative. Eur Radiol. 2021;31(4):2106-2114.
13. Ning P, Zhu S, Shi D, Guo Y, Sun M. X- ray dose reduction in abdominal computed tomography using advanced iterative reconstruction algorithms. PLoS One. 2014; 9(3): e92568.
14. Héliou R, Normandeau L, Beaudoin G. Towards dose reduction in CT: patient radiation dose assessment for CT examinations at university health center in Canada and comparison with national diagnostic reference levels. Radiat Prot Dosimetry. 2012;148(2): 202-210.
15. European Commission (2014) Diagnostic reference levels in thirty-six European countries, Radiation Protection No 180. Publications Office of the European Union, Luxembourg.
16. Medicare Payment Advisory Commission (2019). A data book: Healthcare spending and the Medicare program. Medicare Payment Advisory Commission, Washington, DC.
17. Tsapaki, V.; Aldrich, J.E.; Sharma, R.; Staniszewska, M.A.; Krisanachinda, A.; Rehani, M.; Hufton, A.; Triantopoulou, C.; Maniatis, P.N.; Papailiou, J.; et al. Dose reduction in CT while maintaining diagnostic confidence: Diagnostic reference levels at routine head, chest, and abdominal CT-IAEA-coordinated research project. Radiology 2006, 240, 828–834.
18. Alashban Y., Shubayr N. Establishing diagnostic reference levels for CT examinations in the south region of Saudi Arabia. Radiat. Phys. Chem. 2022; 201: 110407. doi: 10.1016/j.radphyschem.2022.110407.
19. Japan Network for Research and Information on Medical Exposure (J-RIME). National Diagnostic Reference Levels in Japan (2025): Japan DRLs 2025. Tokyo: J-RIME; 2025 Jul 7. Representative: Hosono M. Available from: https://j-rime.qst.go.jp/report/JapanDRLs2025_en.pdf. Accessed March 11, 2026.
20. Nam S, Park H, Kwon S, et al. Updated national diagnostic reference levels and achievable doses for ct protocols: a national survey of Korean hospitals. Tomography. 2022; 8(5): 2450-2459.
21. Kanal K.M., Butler P.F., Sengupta D., Bhargavan-Chatfield M., Coombs L.P., Morin R.L.U.S. diagnostic reference levels and achievable doses for 10 adult CT examinations. Radiology. 2017; 284:120–133. doi: 10.1148/radiol.2017161911.
22. Tsapaki V, Damilakis J, Paulo G, et al. CT diagnostic reference levels based on clinical indications: results of a large-scale European survey. Eur Radiol. 2021;31(7):4459-4469.

Contacts of the corresponding author:

Author:	Anchali Krisanachinda,
Institution:	Department of Radiology, Faculty of Medicine, Chulalongkorn University
Street:	Rama IV Road,
City:	Bangkok 10330,
Country:	Thailand
Email:	anchali.kris@gmail.com

EVALUATION OF RADIATION TRANSPORT AND DOSE DISTRIBUTION IN BORON NEUTRON CAPTURE THERAPY USING PHITS

N.M. Lininding[1,2*], C.G. Dalumpines[1,2], V.C. Convicto[1,2]

[1] Computational and Medical Physics Group, Department of Physics, Mindanao State University-Main Campus, 9700 Marawi City, Philippines

[2] Department of Physics, Mindanao State University-Main Campus, 9700 Marawi City, Philippines

Abstract— **Monte Carlo simulation is used to accurately model a complex radiation transport and dose distributions in Boron Neutron Capture Therapy. BNCT is a type of radiation therapy that uses the interaction of boron and slow neutrons to destroy cancer cells without harming the healthy tissues. This study aims to track millions of particle interactions such as photon, boron, nitrogen and hydrogen via random sampling using Particle Heavy Ion Transport code System (PHITS). The boron concentration was varied from 10-100 μg/g tissue. The cancer geometry was divided into three volumes (Gross Target Volume, Clinical Target Volume, and Planning Target Volume). To ensure an accurate radiation transport and dose distribution, the material compositions were selected from NIST and ICRP 110. The alpha particle and lithium-7 particle flux from the interaction of thermal neutron and boron are restricted to the cancer geometries. This result validates that concept that BNCT can selectively destroy the cancer cells while sparing the healthy tissues. The results showed that increasing boron concentration increases the boron dose, while decreasing the nitrogen dose and photon dose. Lastly, the hydrogen dose stays the same because the hydrogen content in the material composition is almost identical.**

Keywords— **BNCT, PHITS, Dose distribution**

I. INTRODUCTION

The discovery of the interaction between boron-10 and slow neutron, which results in energetic particles that can destroy cells, gave rise to Boron Neutron Capture Therapy in the 1930s [1]. BNCT is a radiation method that delivers a high radiation dose to tumour cells while minimizing damage to surrounding healthy tissue and it is a benign method for treating malignant tumours [2]. BNCT depends on two phenomena. First, the tumour tissue is injected with a non-radioactive boron medication. After then, the patient is exposed to epithermal neutrons until the normal tissue dose limit is reached. When the nonradioactive boron atom captures the thermalized neutron, a decaying process occurs in which the thermalized neutron decays via short-range particles and recoils the Li-7 nucleus [3]. This energy has the power to locally destroy the cancerous cell containing the boron drugs while causing no harm to the surrounding healthy tissue. To achieve a decent result, two parameters need to be considered: boron concentration and neutron beam [2]. Thermal neutrons are the most important for BNCT because they initiate the Li capture reaction. However, because they have a limited depth of penetration, epithermal neutrons, which lose energy and fall into the thermal range as they penetrate tissues, are now preferred for clinical therapy. Several reactors with very good neutron beam quality have been developed and currently are being used clinically [4].

Dosimetry in BNCT is complex since the total absorbed dose is a mixture of different radiation components with different weighting factors [5,6]. These dose components are generally: boron dose, photon dose, nitrogen dose, and hydrogen dose.

Monte Carlo simulation has been used extensively in medical physics for research in radiotherapy, dose analysis, dosimetry, and advanced clinical applications [7]. Several Monte Carlo codes have been extensively utilized in evaluating BNCT such Particle Heavy Ion Transport code System (PHITS), and Monte Carlo N-Particle Transport code (MNCP) to model the complex interactions of neutrons, gamma rays, and other particles within the human tissue to calculate the dose delivered to the cancerous tissues compared to the normal tissues [8].

The BNCT dose calculations in PHITS includes implementing Gross Target Volume, Clinical Target Volume, and Planning Target Volume regions in your simulations, calculating the four dose components in namely boron dose, proton dose, gamma dose and neutron dose.

This study utilizes PHITS to model the dose distribution in brain cancer and to investigate how variation of boron concentration influences the four doses in BNCT simulation.

II. METHODOLOGY

It is necessary to build the geometry model before doing a simulation for BNCT. This study was conducted using the Monte Carlo simulation software PHITS version 3.341 in HP Laptop 15-fd0xxx [9]. The process of the research simulation is shown in Fig. 1.

The variation of boron concentrations was varied from 10-100 μg/g, and increment of 10. The neutron source used in the simulation is an epithermal neutron with a 10 keV energy. The neutron source was ensured to be directed

towards the target regions that contains the boron concentrations.

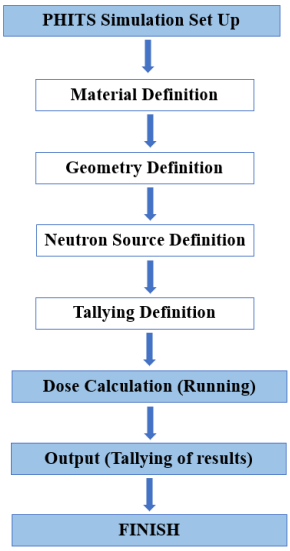

Fig. 1 Flow chart of the simulation approach

For accuracy purposes, the material compositions used in the simulation are brain, bone, skin and cerebral spinal fluid (CSF) which were derived from the elemental composition provided by National Institute of Standard and Technology and ICRP 110 [10,11].

The cancer was divided into three regions, namely, Gross Target Volume (GTV), Clinical Target Volume (CTV) and Planning Target Volume (PTV) and the radii for each part were 2.5, 3.0 and 3.5 cm, respectively. The ratio of the boron concentration in the target regions was 10:5:1.

Table 1 Mass fraction of the normal tissues provided by NIST and ICRP110

Material Composition	Mass Fraction			
	Brain	Bone	Skin	CSF
Hydrogen	0.110667	0.110667	0.100588	0.11000
Carbon	0.125420	0.125420	0.228250	
Nitrogen	0.013280	0.013280	0.046420	
Oxygen	0.737723	0.737723	0.619002	0.89000
Sodium	0.001840	0.001840	0.000070	
Magnesium	0.000150	0.000150	0.000060	
Phosphorous	0.003540	0.003540	0.000330	
Sulfur	0.001770	0.001770	0.001590	
Chlorine	0.002360	0.002360	0.002670	
Potassium	0.003100	0.003100	0.000850	
Calcium	0.000090	0.000090	0.000150	
Iron	0.000050	0.000050	0.000010	
Zinc	0.000010	0.000010	0.000010	

The tallying functions used in the simulation for different types of dose calculation of the four doses (boron, photon, nitrogen and hydrogen) are t-track. The number of batches (maxbch) and particles per batch (maxcas) depends on the required accuracy and computational power. More batches help improve statistical averaging of the simulation and more particles per batch reduce the variance in scoring [12]. For high precision and accuracy, it is recommended to use 10 million neutron histories for BNCT simulation.

III. RESULTS AND DISCUSSION

In Fig. 2, region one to three are the target volumes. Region 1 is the Gross Target Volume where most of the cancer is located, region 2 is the Clinical Target Volume which comprises of 50% of the cancer cells, and region 3 is the Planning Target Volume which is just a marginal part of the cancer. The rest of the layering regions are the normal regions (brain, bone, Cerebral Spinal Fluid and skin). As seen Fig. 2, the combined flux map distribution of alpha particle and Lithium-7 is severely restricted to the target volumes where the boron is located. This is due to their short range of these particles which validates the selective generation of high-LET particles at the boron-loaded region.

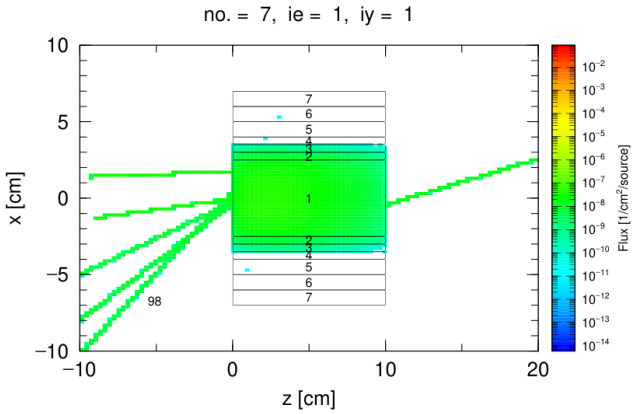

Fig. 2 Alpha + lithium-7 particle flux map distribution in r-z mesh

The simulated boron dose per source which selectively hits the tumour came from the high-LET alpha particle and lithium-7 recoil produced from boron capture. The photon dose came from the prompt captures of gamma (mainly boron and hydrogen) and other reactions contributing to a low-LET, whole body background dose). The hydrogen is mainly from the recoil of protons created by fast neutron scattering on hydrogen. Nitrogen is from the energetic protons emitted from carbon 14. The simulated boron, nitrogen, photon and hydrogen dose are shown in Figures 3, 4, 5, and 6 respectively.

In BNCT, the simulated doses are the calculation of the absorbed energy transmitted to a tissue. As seen in Fig. 3,

the simulated boron dose in Gross Target Volume, Clinical Target Volume and Planning Target Volume increases as the boron concentration is increased as the dose is directly proportional to the boron content within the cancerous cells. Increasing the boron concentration will lead to a larger fraction of neutron that creates an alpha particle and a lithium nucleus, and these particles produce a charge particle, hence the dose shifts toward a less gamma dose.

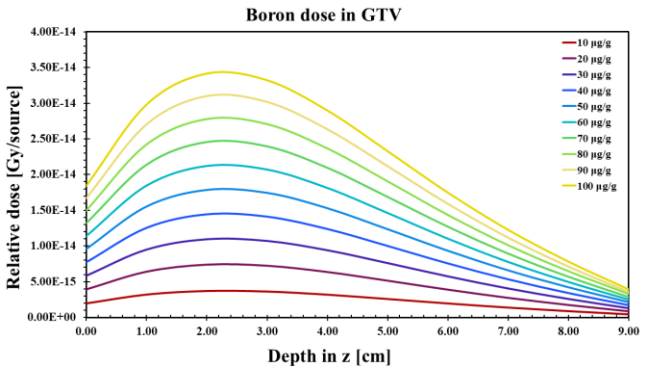

Fig. 3 (a) Boron dose at GTV (assumed to have 100% concentration)

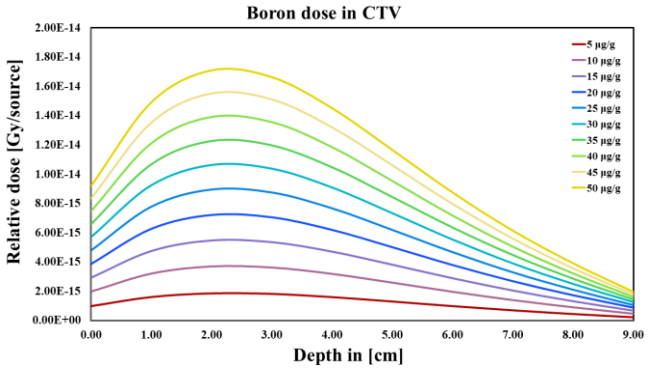

Fig. 3 (b) Boron dose at CTV (assumed to have 50% concentration)

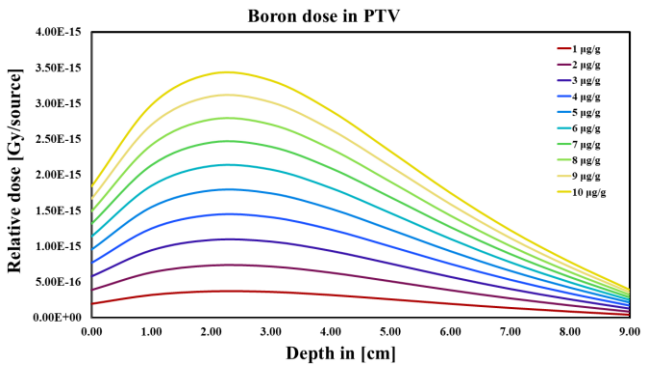

Fig. 3 (c) Boron dose at PTV (assumed to have 10% concentration)

Thus, as seen in Figure 4, the photon dose decreases with increasing boron concentration. Gamma rays are likely to be absorbed as tissues with high boron concentration have a slightly higher density and slightly higher gamma attenuation coefficient. Additionally, increasing the boron concentration produces more epithermal neutrons to thermal neutrons.

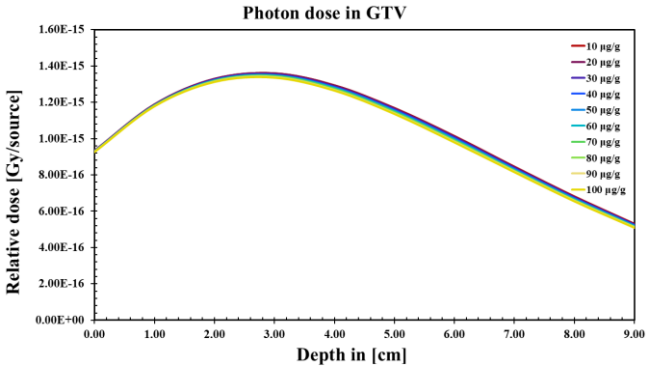

Fig. 4 (a) Photon dose at GTV (assumed to have 100% concentration)

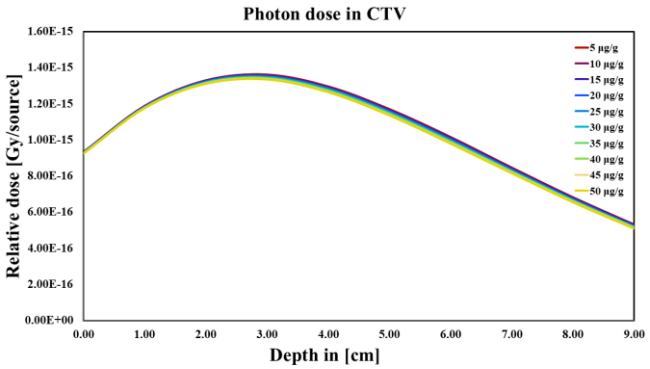

Fig. 4 (b) Photon dose at CTV (assumed to have 50% concentration)

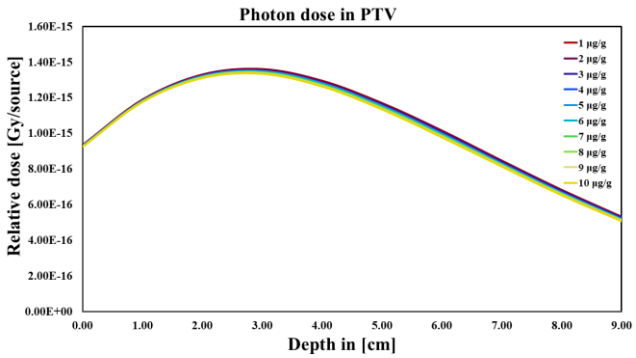

Fig. 4 (c) Photon dose at PTV (assumed to have 10% concentration)

This interaction causes an increase of nitrogen dose when the boron concentration is increased as seen in Fig. 6. Meanwhile, the hydrogen dose (see Fig. 5) does not change, or the changes is barely seen in the figure.

The hydrogen dose comes from the elastic scattering of neutron which produces proton recoil. This is because the hydrogen contents within the materials and the density of the materials are almost the same. Hydrogen dose depends on the density of the material, neutron flux specifically for fast neutron. So, when boron concentration is increased, the hydrogen dose stays almost identical.

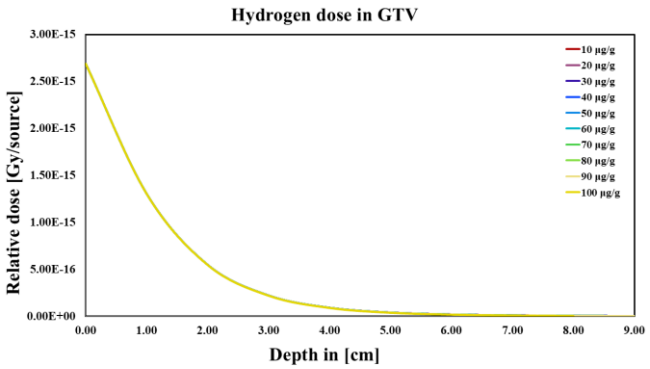

Fig. 5 (a) Hydrogen dose at GTV (assumed to have 100% concentration)

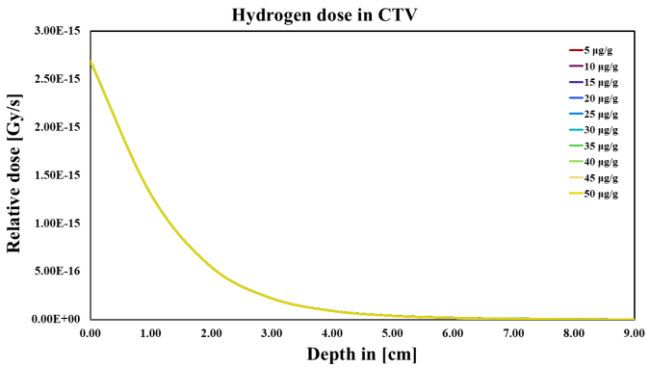

Fig. 5 (b) Hydrogen dose at CTV (assumed to have 50% concentration)

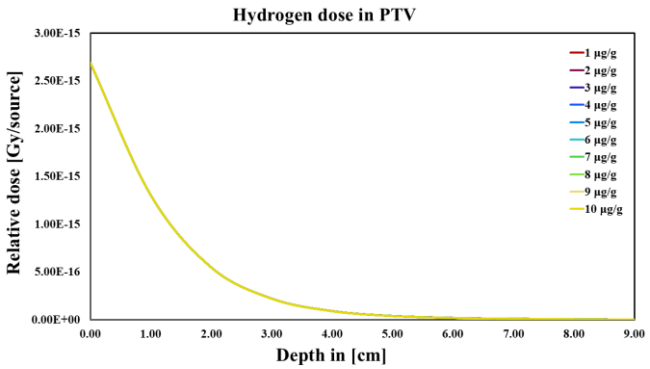

Fig. 5 (C) Hydrogen dose at PTV (assumed to have 10% concentration)

Nitrogen is naturally present in a human body; they could be protein or even in DNA. Similarly, the nitrogen dose decreases with increasing boron concentration due to the fact that boron is ten times more attractive than nitrogen, which tends for neutron to interact with boron before they can interact with nitrogen atom. These results and observation are similar to photon wherein increasing boron concentration decreases the photon dose.

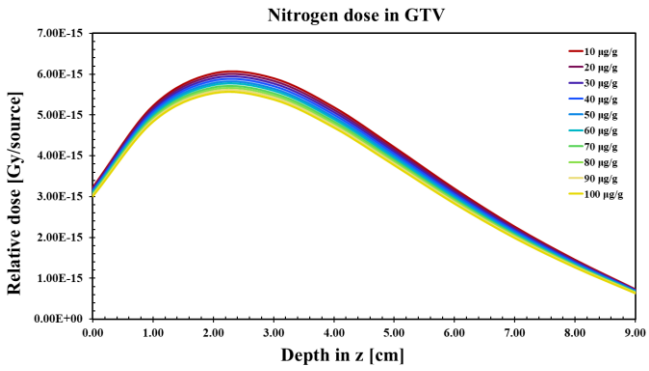

Fig. 6 (a) Nitrogen dose at GTV (assumed to have 100% concentration)

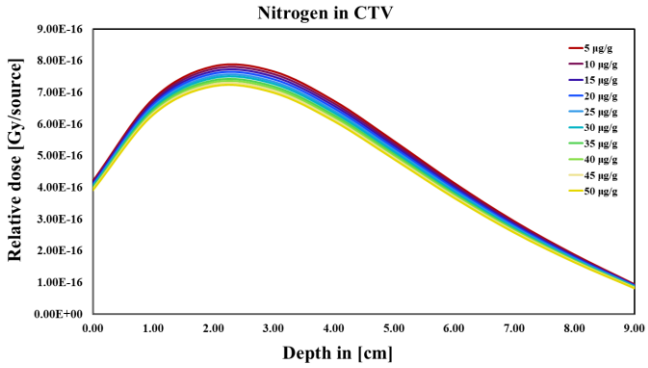

Fig. 6 (b) Nitrogen dose at CTV (assumed to have 50% concentration)

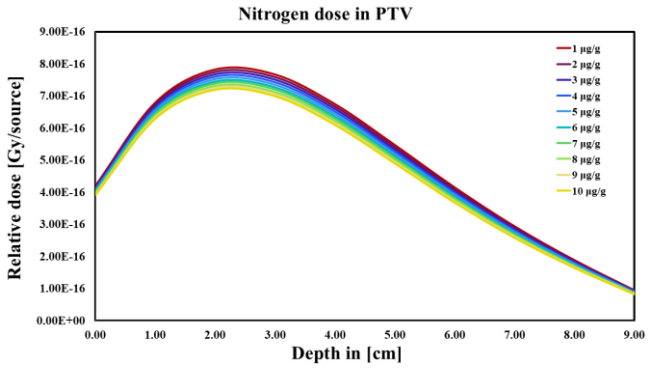

Fig. 6 (c) Nitrogen dose at PTV (assumed to have 10% concentration)

These following observations are all the same in the defined target volumes in the cancer geometry. However, in the normal tissues defined in the simulation (brain, CSF, bone and skin), changes are not seen in the boron dose, nitrogen dose, photon dose and hydrogen dose. This is because those tissues are assumed to be normal tissues and ensured that they will not be affected by the irradiation.

IV. CONCLUSIONS

The simulation result demonstrates a clear correlation between the boron-loaded regions and the generation of the therapeutic particles. The analysis from the r-z mesh flux maps validates the microscopic selectivity of BNCT as the high-LET alpha and lithium-7 particles are restricted to the target volumes while sparing the normal tissues. This is due to the short range of these particles (approx. 5-9 μm); thus, the nuclear reaction is within the area where the cancer is located [13]. The correlation of boron concentration to the four doses in BNCT were investigated thoroughly. The boron dose and boron concentration has a linear correlation which demonstrates that higher boron uptake significantly increases the destruction of the cancer cells. In contrast, increasing the boron concentration decreases the photon and nitrogen dose. Lastly, the stability of the hydrogen dose is from the fast neutron recoils which remains unchanged as the concertation is increased. These results demonstrates that increasing boron concentration provides secondary benefit sparing the healthy tissues from destructive doses from the nuclear reaction of boron and slow neutron. These results suggest that a higher boron-to-tissue ratio significantly improves the therapeutic gain without increasing the fast neutron background.

V. ACKNOWLEDGMENT

The authors acknowledge the support extended by Dr. Hiroshi Takemiya, Director of the Centre for Computational Science & E-Systems at the Japan Atomic Energy Agency (JAEA) for the use of Particle and Heavy Ion Transport code System (PHITS). We also acknowledge the DOST Learning Resource Centre for the computer resources used for simulation. Likewise, N. M. Lininding and C. G. M. Dalumpines acknowledge the DOST-SEI for the STRAND scholarship grant.

VI. REFERENCES

1. Barth R. F, Zhang Z, Liu T (2018) A realistic appraisal of boron neutron capture therapy as a cancer treatment modality. Cancer Communications. pp. 1-7
2. Anderson B. A, Bagaswoto P (2018) Overview of boron neutron capture therapy: a medical aspect. ASEAN Journal on Science and Technology for Development, vol. 35, no. 0217-5460, 217-221
3. Horiguchi H, Sato T, Kumada H, et al (2014). Estimation of relative biological effectiveness for boron neutron capture therapy using PHITS code coupled with a microdosimetric kinetic model. Journal of Radiation Research, 56(2), 382-390
4. Kumada H, Takada K (2018) Treatment planning system and patient positioning for boron neutron capture therapy. Therapeutic Radiology and Oncology, 2, 50-50.
5. Barth R. F, Gupta N, & Kawabata S, (2024) Evaluation of sodium borocaptate (BSH) and boronophenylalanin (BPA) as boron delivery agents for neutron capture therapy (NCT) of cancer: An update and a guide for the future clinical evaluation of new boron delivery agents for NCT. Cancer Communication.
6. Wang S, Zhang Z, Miao L, et al (2022). Boron neutron capture therapy: current status and challenges. Frontiers in Oncology, vol. 12.
7. Shields J (2022) A review on monte carlo methods and their application in medical physics for simulating radiation transport. Honors Theses and Capstones. 657
8. Seco J, and Verhaegen F (2021) Monte carlo techniques in radiation therapy: applications to dosimetry, imaging, and preclinical radiotherapy. Biomedical Engineering
9. Sato T, Niita K, Matsuda N, et al (2022) Particle and Heavy Ion Transport code System (PHITS), version 3.34 User's Manual. Japan Atomic Energy Agency
10. International Commission on Radiological Protection, (2009) Adult Reference Computational Phantoms, Annals of the ICRP 39
11. National Institute of Standard and Technology (2025), Atomic Weight and Isotropic Compositions with Relative Atomic Masses at https://www.nist.gov/pml/atomic-weight-and-isotropic-compositions-relative-atomic-masses
12. Uyar E, Gunekbay Z (2023) Comparison of the number of particle history for monte carlo codes in gamma-ray spectroscopy. Journal of Science, Part A, 10(2): 176-183
13. Nedunchezhian K, Aswath N, Thiruppathy M, et al (2016). Boron neutron capture therapy - a literature review. Journal of Clinical and Diagnostic Research. pp. 1-4

Contacts of the corresponding author:

Author: Nihayah M. Lininding
Institute: Mindanao State University
Street: Ilian Street
City: Marantao, Lanao del Sur
Country: Philippines
Email: lininding.nm94@s.msumain.edu.ph

BOOK REVIEW

UNDERSTANDING CRISIS COMMUNICATION: THE INTERPLAY OF SOCIAL MEDIA, TRUST, SCIENTIFIC KNOWLEDGE AND PUBLIC POLICY

Authors: Jiankun Gong, Muhammad Zaiamri Zainal Abidin, Kwan-Hoong Ng

Review by

F. Hasford[1], C.K. Engmann[2]

[1]Ghana Atomic Energy Commission, Accra, Ghana.
[2]Nuclear Regulatory Authority, Accra, Ghana.

I. PUBLISHER

Publisher: Springer Nature, Cham, Switzerland, 2026.
Hardcover ISBN: 978-3-031-97493-5
eBook ISBN: 978-3-031-97494-2
DOI: 10.1007/978-3-031-97494-2
Number of pages: 203

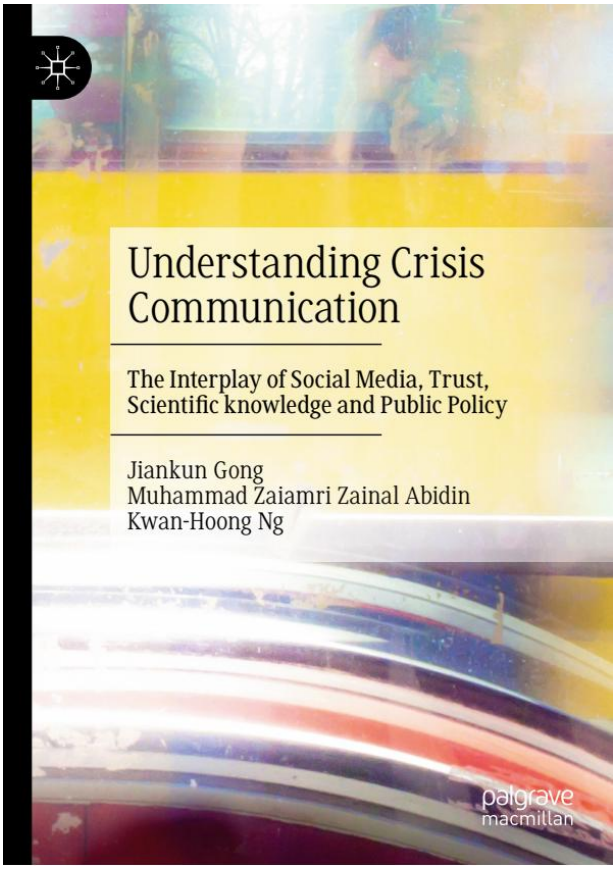

II. OVERVIEW

Understanding Crisis Communication provides a comprehensive examination of the principles, theories, and practical applications of crisis communication across high-risk sectors, with particular emphasis on nuclear incidents. The authors present an interdisciplinary analysis that combines communication science, organizational behaviour, public policy, and risk management to demonstrate how communication influences public trust, institutional credibility, and policy outcomes during crises. While the book addresses crisis communication broadly, its extensive treatment of nuclear accidents makes it especially relevant to professionals in medical physics, radiation protection, nuclear engineering, and emergency preparedness.

III. CONTENT AND ORGANIZATION

The book is logically organized into thematic chapters that progressively build the reader's understanding of crisis communication. It begins by introducing foundational theories, including Situational Crisis Communication Theory (SCCT), the Social-Mediated Crisis Communication (SMCC) model, Image Restoration Theory, and the science–policy interface. These theoretical concepts provide a framework for evaluating institutional responses to crises and are effectively applied throughout the book.

A major strength of the publication is its detailed examination of four landmark nuclear accidents: the SL-1 reactor accident (1961), Three Mile Island (1979), Chernobyl (1986), and Fukushima Daiichi (2011). Each case study follows a consistent structure, examining the historical background, communication strategies adopted by responsible institutions, public and media reactions, lessons learned, and implications for future crisis management. The authors demonstrate how differences in political environments, media ecosystems, and institutional transparency shaped public perception and trust during these events.

Particularly noteworthy is the analysis of the Three Mile Island accident, where delayed disclosure, inconsistent messaging, technical jargon, and fragmented institutional communication significantly undermined public confidence despite relatively limited radiological consequences. The discussion illustrates that communication failures can

become crises in their own right, independent of technical failures.

IV. RELEVANCE TO MEDICAL PHYSICS

Although primarily written from a crisis communication perspective, the book offers important lessons for medical physicists and radiation safety professionals. Modern healthcare increasingly depends on advanced radiation technologies, including diagnostic imaging, radiotherapy, radionuclide therapy, and artificial intelligence. While these technologies operate under different circumstances from nuclear power plants, they similarly require effective communication whenever incidents, accidental exposures, equipment failures, or public concerns arise.

The principles discussed throughout the book, including transparency, timely communication, stakeholder engagement, empathy, and acknowledgement of uncertainty, are directly applicable to radiation medicine and nuclear healthcare. Medical physicists, who increasingly serve as technical advisors and safety leaders, will find valuable guidance on communicating complex scientific information to patients, healthcare professionals, regulators, and the general public.

Furthermore, the discussion on maintaining institutional trust is highly relevant to radiation protection programmes, eergency preparedness planning, and hospital incident management.

V. STRENGTHS

Several features distinguish this publication. First, the integration of communication theory with real-world nuclear case studies provides readers with both conceptual understanding and practical application. Rather than merely describing historical events, the authors critically evaluate communication decisions using established theoretical frameworks.

Second, the writing is accessible despite addressing complex multidisciplinary topics. Technical concepts are explained clearly, allowing readers from communication, engineering, public health, and nuclear science backgrounds to benefit equally.

Third, the extensive referencing demonstrates thorough scholarship and encourages further exploration of crisis communication literature. The inclusion of contemporary communication theories alongside historical accident analyses enhances the academic value of the book.

Finally, the emphasis on trust, transparency, and stakeholder engagement reflects current international best practices in emergency preparedness and risk communication.

VI. OVERALL ASSESSMENT

Understanding Crisis Communication is a timely and well-researched contribution to the growing literature on crisis and risk communication. By demonstrating that effective communication is as critical as technical competence during emergencies, the authors make a compelling case for integrating communication planning into organizational risk management strategies.

The book serves as a valuable reminder that communication itself constitutes an essential component of radiation safety culture. As medical physicists increasingly assume leadership roles in quality assurance, radiation protection, emergency preparedness, and public engagement, the lessons presented throughout this volume are both relevant and practical.

VII. RECOMMENDATION

This publication successfully bridges communication science and nuclear technology, offering practical insights that extend well beyond the nuclear industry into healthcare and medical physics practice. Its emphasis on transparency, trust-building, and evidence-based communication makes it a valuable addition to the professional library of anyone involved in radiation-related disciplines.

The book is highly recommended for medical physicists, radiation protection professionals, nuclear scientists, healthcare administrators, emergency managers, policymakers, researchers, and postgraduate students seeking a deeper understanding of crisis communication within technologically complex environments.

VIII. REFERENCES

1. Gong J, et al. Understanding Crisis Communication. Cham: Springer Nature Switzerland; 2026. eBook ISBN: 978-3-031-97494-2. doi:10.1007/978-3-031-97494-2.

Contacts of the corresponding author:

Author:	Francis Hasford
Institute:	Ghana Atomic Energy Commission
City:	Accra
Country:	Ghana
Email:	haspee@yahoo.co.uk

INFORMATION FOR AUTHORS

INFORMATION FOR AUTHORS

INFORMATION FOR AUTHORS

INSTRUCTIONS FOR AUTHORS

The goal of the new IOMP Journal Medical Physics International (http://mpijournal.org) is to publish manuscripts that will enhance medical physics education and professional development on a global basis. There is a special emphasis on general review articles, reports on specific educational methods, programs, and resources. In general, this will be limited to resources that are available at no cost to medical physicists and related professionals in all countries of the world. Information on commercial educational products and services can be published as paid advertisements. Research reports are not published unless the subject is educational methodology or activities relating to professional development. High-quality review articles that are comprehensive and describe significant developments in medical physics and related technology are encouraged. These will become part of a series providing a record of the history and heritage of the medical physics profession.

A special feature of the IOMP MPI Journal will be the publication of thesis and dissertation abstracts for will be the publication of thesis and dissertation abstracts for recent doctoral graduates, specifically those receiving their doctoral degrees in medical physics (or closely related fields) in 2010 or later.

MANUSCRIPT STYLE

Manuscripts shall be in English and submitted in WORD. Either American or British spelling can be used but it must be the same throughout the manuscript. Authors for whom English is not their first language are encouraged to have their manuscripts edited and checked for appropriate grammar and spelling. Manuscripts can be up to 10 journal pages (approximately 8000 words reduced by the space occupied by tables and illustrations) and should include an unstructured abstract of no more than 100 words.

The style should follow the template that can be downloaded from the website at:

http://mpijournal.org/authors_submitapaper.aspx

ILLUSTRATIONS SPECIAL REQUIREMENTS

Illustrations can be inserted into the manuscript for the review process but must be submitted as individual files when a manuscript is accepted for publication.

The use of high-quality color visuals is encouraged. Any published visuals will be available to readers to use in their educational activities without additional approvals.

REFERENCE WEBSITES

Websites that relate to the manuscript topic and are sources for additional supporting information should be included and linked from within the article or as references.

EDITORIAL POLICIES, PERMISSIONS AND APPROVALS

AUTHORSHIP

Only persons who have made substantial contributions to the manuscript or the work described in the manuscript shall be listed as authors. All persons who have contributed to the preparation of the manuscript or the work through technical assistance, writing assistance, financial support shall be listed in an acknowledgements section.

CONFLICT OF INTEREST

When they submit a manuscript, whether an article or a letter, authors are responsible for recognizing and disclosing financial and other conflicts of interest that might bias their work. They should acknowledge in the manuscript all financial support for the work and other financial or personal connections to the work.

All submitted manuscripts must be supported by a document (form provided by MPI) that:

• Is signed by all co-authors verifying that they have participated in the project and approve the manuscript as submitted.

• Stating where the manuscript, or a substantially similar manuscript has been presented, published, or is being submitted for publication. Note: presentation of a paper at a conference or meeting does not prevent it from being published in MPI and where it was presented can be indicated in the published manuscript.

• Permission to publish any copyrighted material, or material created by other than the co-authors, has been obtained.

• Permission is granted to MPI to copyright, or use with permission copyrighted materials, the manuscripts to be published.

• Permission is granted for the free use of any published materials for non-commercial educational purposes.

SUBMISSION OF MANUSCRIPTS

Manuscripts to be considered for publication should be submitted as a WORD document to:

Francis Hasford, Co-editor: haspee@yahoo.co.uk

Sameer Tipnis, Co-editor: tipnis@musc.edu

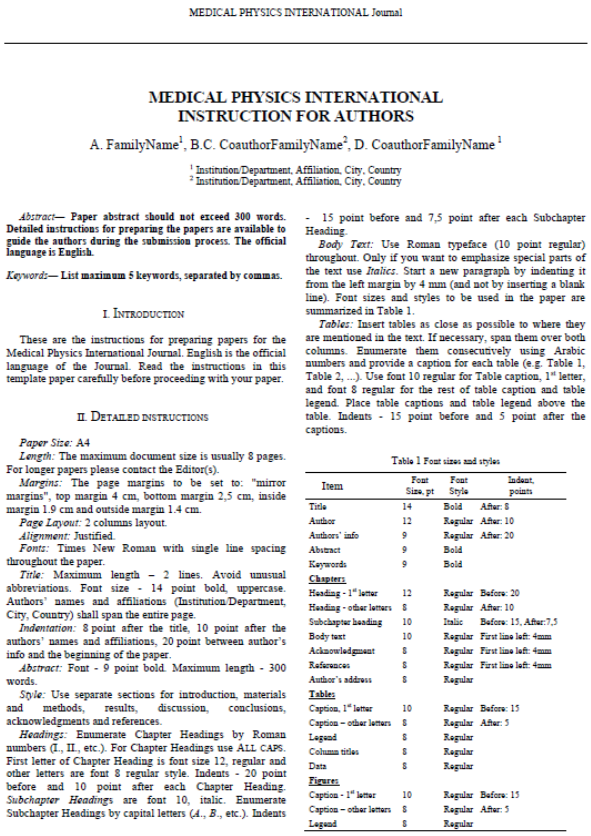

MEDICAL PHYSICS INTERNATIONAL Journal

MEDICAL PHYSICS INTERNATIONAL INSTRUCTION FOR AUTHORS

A. FamilyName[1], B.C. CoauthorFamilyName[2], D. CoauthorFamilyName [1]

[1] Institution/Department, Affiliation, City, Country
[2] Institution/Department, Affiliation, City, Country

Abstract— **Paper abstract should not exceed 300 words. Detailed instructions for preparing the papers are available to guide the authors during the submission process. The official language is English.**

Keywords— **List maximum 5 keywords, separated by commas.**

I. INTRODUCTION

These are the instructions for preparing papers for the Medical Physics International Journal. English is the official language of the Journal. Read the instructions in this template paper carefully before proceeding with your paper.

II. DETAILED INSTRUCTIONS

Paper Size: A4
Length: The maximum document size is usually 8 pages. For longer papers please contact the Editor(s).
Margins: The page margins to be set to: "mirror margins", top margin 4 cm, bottom margin 2,5 cm, inside margin 1.9 cm and outside margin 1.4 cm.
Page Layout: 2 columns layout.
Alignment: Justified.
Fonts: Times New Roman with single line spacing throughout the paper.
Title: Maximum length – 2 lines. Avoid unusual abbreviations. Font size - 14 point bold, uppercase. Authors' names and affiliations (Institution/Department, City, Country) shall span the entire page.
Indentation: 8 point after the title, 10 point after the authors' names and affiliations, 20 point between author's info and the beginning of the paper.
Abstract: Font - 9 point bold. Maximum length - 300 words.
Style: Use separate sections for introduction, materials and methods, results, discussion, conclusions, acknowledgments and references.
Headings: Enumerate Chapter Headings by Roman numbers (I., II., etc.). For Chapter Headings use ALL CAPS. First letter of Chapter Heading is font size 12, regular and other letters are font 8 regular style. Indents - 20 point before and 10 point after each Chapter Heading. *Subchapter Headings* are font 10, italic. Enumerate Subchapter Headings by capital letters (*A.*, *B.*, etc.). Indents - 15 point before and 7,5 point after each Subchapter Heading.
Body Text: Use Roman typeface (10 point regular) throughout. Only if you want to emphasize special parts of the text use *Italics*. Start a new paragraph by indenting it from the left margin by 4 mm (and not by inserting a blank line). Font sizes and styles to be used in the paper are summarized in Table 1.
Tables: Insert tables as close as possible to where they are mentioned in the text. If necessary, span them over both columns. Enumerate them consecutively using Arabic numbers and provide a caption for each table (e.g. Table 1, Table 2, ...). Use font 10 regular for Table caption, 1st letter, and font 8 regular for the rest of table caption and table legend. Place table captions and table legend above the table. Indents - 15 point before and 5 point after the captions.

Table 1 Font sizes and styles

Item	Font Size, pt	Font Style	Indent, points
Title	14	Bold	After: 8
Author	12	Regular	After: 10
Authors' info	9	Regular	After: 20
Abstract	9	Bold	
Keywords	9	Bold	
Chapters			
Heading - 1st letter	12	Regular	Before: 20
Heading - other letters	8	Regular	After: 10
Subchapter heading	10	Italic	Before: 15, After:7,5
Body text	10	Regular	First line left: 4mm
Acknowledgment	8	Regular	First line left: 4mm
References	8	Regular	First line left: 4mm
Author's address	8	Regular	
Tables:			
Caption, 1st letter	10	Regular	Before: 15
Caption – other letters	8	Regular	After: 5
Legend	8	Regular	
Column titles	8	Regular	
Data	8	Regular	
Figures:			
Caption - 1st letter	10	Regular	Before: 15
Caption – other letters	8	Regular	After: 5
Legend	8	Regular	

MANUSCRIPT PROPOSALS

Authors considering the development of a manuscript for a Review Article can first submit a brief proposal to the editors. This should include the title, list of authors, an abstract, and other supporting information that is appropriate. After review of the proposal the editors will consider issuing an invitation for a manuscript. When the manuscript is received it will go through the usual peer-review process.

PUBLICATION OF MULTIPLE ARTICLES FROM SAME INSTITUTION

To ensure balanced publication, not more than two articles from the same institution will be published in a single issue of MPI. If more than two are accepted, the Co-editors-in-chief may publish the first two and postpone the others to future issues.

Figures: Insert figures where appropriate as close as possible to where they are mentioned in the text. If necessary, span them over both columns. Enumerate them consecutively using Arabic numbers and provide a caption for each figure (e.g. Fig. 1, Fig. 2, …). Use font 10 regular for Figure caption, 1st letter, and font 8 regular for the rest of figure caption and figure legend. Place figure legend beneath figures. Indents - 15 point before and 5 point after the captions. Figures are going to be reproduced in color in the electronic versions of the Journal, but may be printed in grayscale or black & white.

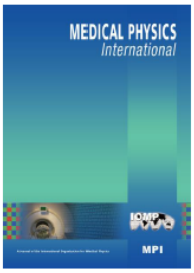

Fig. 1 Medical Physics International Journal

Equations: Write the equation in equation editor. Enumerate equations consecutively using Arabic numbers

$$A + B = C \quad (1)$$

$$X = A \times e^{st} + 2\mathrm{lkt} \quad (2)$$

Items/Bullets: In case you need to itemize parts of your text, use either bullets or numbers, as shown below:

- First item
- Second item

1. Numbered first item
2. Numbered second item

References: Use Arabic numbers in square brackets to number references in such order as they appear in the text. List them in numerical order as presented under the heading 'REFERENCES'. Examples of citations for Journal articles [1], books [2], the Digital Object Identifier (DOI) of the cited literature [3], Proceedings papers [4] and electronic publications [5].

III. CONCLUSIONS

Send your papers only in electronic form. Papers to be submitted prior the deadline. Check the on-line Editorial Process section for more information on Paper Submission and Review process.

ACKNOWLEDGMENT

Format the Acknowledgment headlines without numbering.

REFERENCES

The list of References should only include papers that are cited in the text and that have been published or accepted for publication. Citations in the text should be identified by numbers in square brackets and the list of references at the end of the paper should be numbered according to the order of appearance in the text.

Cited papers that have been accepted for publication should be included in the list of references with the name of the journal and marked as ''in press''. The author is responsible for the accuracy of the references. Journal titles should be abbreviated according to Engineering Index Inc. References with correct punctuation.

1. LeadingAuthor A, CoAuthor B, CoAuthor C et al. (2012) Paper Title. Journal 111:220–230
2. LeadingAuthor D, CoAuthor E (2000) Title. Publisher, London
3. LeadingAuthor A, CoAuthor B, CoAuthor C (2012) Paper Title. Journal 111:330–340 DOI 123456789
4. LeadingAuthor F, CoAuthor G (2012) Title, IOMP Proceedings. vol. 4, World Congress on Med. Phys. & Biomed. Eng., City, Country, 2012, pp 300–304
5. MPI at http://www.mpijournal.org

Contacts of the corresponding author:

Author:
Institute:
Street:
City:
Country:
Email: